UNIVERSITÀ DEGLI STUDI DI NAPOLI "FEDERICO II"

DIPARTIMENTO DI INGEGNERIA INDUSTRIALE

SCUOLA DI DOTTORATO IN INGEGNERIA INDUSTRIALE

High-accuracy Digital Elevation Model generation and Ship Monitoring from Synthetic Aperture Radar images: innovative techniques and experimental results

DOTTORATO DI RICERCA IN

"***INGEGNERIA AEROSPAZIALE, NAVALE E DELLA QUALITÀ***"

INDIRIZZO IN "*INGEGNERIA AEROSPAZIALE*"

XXV CICLO

Dott. Ing. Andrea Cecchini

Tutor

Ch.mo Prof. Ing. Antonio Moccia

Coordinatore

Ch.mo Prof. Ing. Luigi De Luca

Anno Accademico 2011/2012

Alla mia famiglia e a Danila,

per aver condiviso con me ogni emozione di questo percorso

ABSTRACT

In this Thesis several state-of-the-art and innovative techniques for Digital Elevation Model (DEM) generation from Synthetic Aperture Radar (SAR) images are deeply analyzed, with a special focus on the methods which allow the improvement of the accuracy of the DEM product, which is directly related to the geolocation accuracy of geocoded images and is considered as an enabling factor for a large series of civilian and Defence applications. Furthermore, some of the proposed techniques, which are based both on phase and amplitude information, are experimented on real data, i.e. COSMO-SkyMed (CSK) data, assessing the achievable performances compared with the state-of-the-art, and pointing out and quantitatively highlighting the acquisition and processing strategies which would allow to maximize the quality of the results. Moreover, a critical analysis is performed about the main errors affecting the applied techniques, as well as the limitations of the orbital configurations, identifying several complementary techniques which would allow to overcome or mitigate the observed drawbacks. An innovative procedure for on-demand DEM production from CSK SAR data is elaborated and proposed, as well as an auto-validation technique which would enable the validation of the produced DEM also where vertical ground truths are not available. Based on the obtained results and on the consequent critical analysis, several interferometric specifications for new generation SAR satellites are identified. Finally, a literature review is proposed about the main state-of-the-art ship monitoring techniques, considered as one of the main fields of application which takes benefit from SAR data, based on single/multi-platform multi-channel SAR data, with a focus on TanDEM-X (TDX).

In particular, in Chapter 1 the main concepts concerning SAR operating principles are introduced and the main characteristics and performances of CSK and TDX satellite systems are described; in Chapter 2 a review is proposed about the state-of-the-art SAR interferometric techniques for DEM generation, analyzing all the relevant processing steps and deepening the study of the main solutions recently proposed in the literature to increase the accuracy of the interferometric processing; in Chapter 3 complementary and innovative techniques respect to the interferometric processing are analyzed to mitigate disadvantages and to improve performances; in Chapter 4 experimental results are presented, obtained in the generation of high accuracy DEM by applying to a dataset of CSK images properly selected state-of-the-art interferometric techniques and innovative methods to improve DEM accuracy, exploring relevant limitations, and pointing out innovative acquisition and processing strategies. In Chapter 5, the basic principles of Ground Moving Target Indication (GMTI) are described, focusing on Displaced Phase Center Antenna (DPCA) and Along-Track Interferometry (ATI) techniques.

CONTENTS

CHAPTER 1
INTRODUCTION

In this Chapter the main concepts concerning Synthetic Aperture Radar operating principles are introduced and the main characteristics and performances of COSMO-SkyMed and TanDEM-X satellite systems are described. This introduction is useful for a full understanding of the following Chapters of this Thesis.

1.1. Synthetic Aperture Radars basics

Considering a basic radar system which transmits a sinusoidal signal $s_{sin}(u)$ of length T and carrier frequency $f_0 = \omega_0/2\pi$, equation 1.1.

$$s_{sin}(u) = \cos(\omega_0 u) \quad \text{for } -T/2 < u < T/2 \tag{1.1}$$

the bandwidth B_p of the sinusoidal pulse is defined in equation 1.2.

$$B_p = \frac{1}{T} \tag{1.2}$$

Therefore, long sinusoidal pulses have a narrow bandwidth and short pulses have a wide bandwidth. Since the pulse bandwidth is related to the resolution in the range direction of the radar system, it is of great importance in the following considerations.

Considering two point targets separated in range by a distance Δd, the two echoes at the radar receiver will be separated by a time $\Delta u = 2\Delta d/c$, therefore the pulse duration should be $T < 2\Delta d/c$ in order to not overlap the two echoes at the receiver.

The range resolution Δ_r can be defined as the shortest separation Δd which can be measured by the radar, equation 1.3.

$$\Delta_r = \Delta d = \frac{cT}{2} = \frac{c}{2B} \tag{1.3}$$

From equation 1.3 it is possible to understand how to have a high range resolution (i.e. a small Δ_r) it is necessary to have a wide bandwidth or a short pulse duration.

Since the pulse duration is directly related to the pulse energy, through the instantaneous peak power P_p, i.e. $E = P_p T$, and since the maximum power is limited by the radar hardware, a trade-off

should be done in radar systems between the energy which implies a large pulse duration and the resolution which implies a large bandwidth. This trade-off can be done by phase modulation.
In particular a chirp modulation is used, which is a linear frequency modulation. The frequency f_0 changes linearly from f_0 to $f_0 + \Delta f$ during the pulse duration. In this case the bandwidth B_c is independent on the pulse length T, equation 1.4.

$$B_c = (f_0 + \Delta f\ ) - f_0 = \Delta f \tag{1.4}$$

Therefore, through chirp modulation, it is possible to obtain a pulse with a large duration and a large bandwidth at the same time, which means high range resolution and high pulse energy.
The benefit of the chirp is the possibility to compress it at the receiver: it is possible to obtain with a chirp of long duration the same range resolution achievable with a short duration pulse, then at the reception through a matched filter it is possible to compress the total energy into a shorter pulse. The spectrum of a linear frequency modulated signal has a quadratic phase, in the frequency domain this spectrum is multiplied by a filter having the conjugate quadratic phase of the input signal, returning a flat phase. Finally, the inverse Fourier transform gives a time compressed signal, (Rizzato, 2012).
The length of the output pulse T' is limited by the bandwidth B_c through equation 1.5.

$$T' = \frac{1}{B_c} = \frac{1}{\Delta f} \tag{1.5}$$

Concerning the azimuth resolution, which is the shortest distance between two point targets which can be discriminated along the azimuth direction, for a real aperture radar it is related to the width in azimuth of the antenna footprint, since all the pulses from different azimuth positions and with the same range reach the receiver at the same time, equation 1.6.

$$\Delta'_a = \frac{R_0 \theta'_a}{\cos(\theta_l)} \tag{1.6}$$

where R_0 is the slant range, θ_l is the look angle and $\theta'_a = \lambda / L$ is the azimuth beamwidth of the antenna, where λ is the wavelength and L is the length of the antenna beamwidth. From equation 1.6 it is possible to understand that the azimuth resolution of a real aperture radar decreases (i.e. Δ'_a increases) with the slant range distance, which can be balanced only by increasing the antenna length L. Therefore, with a real aperture radar it would not be possible to obtain high azimuth resolution from satellites, because of the high slant range distance and the difficulty to have large antennas onboard the satellite.

The only solution to increase the azimuth resolution is the synthetic aperture radar. The idea at the basis of the synthetic aperture radar is to coherently add successive echoes received through the satellite flight, to synthesize a linear antenna array. The synthetic aperture L_s is defined as the azimuth length of the real antenna main beam footprint, Fig. 1.1, equation 1.7.

$$L_s = R_0 \theta'_a = R_0 \frac{\lambda}{L} \tag{1.7}$$

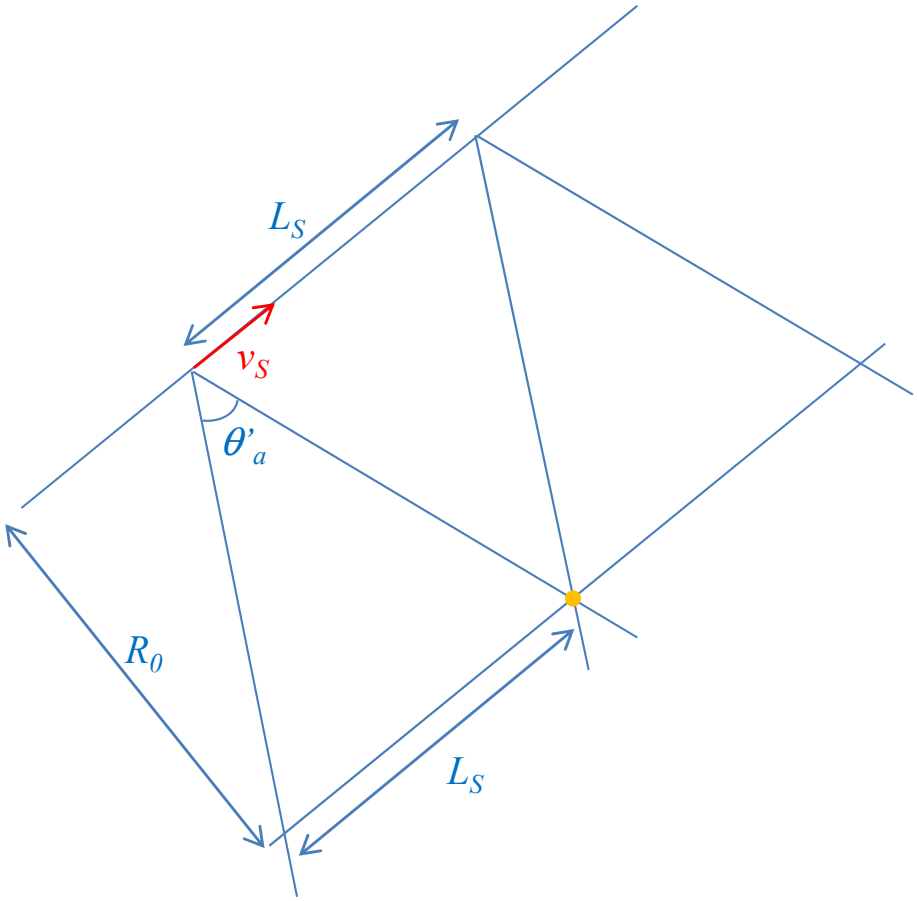

Fig. 1.1 – Synthetic Aperture Radar.

Therefore, also the beam width θ_s of the synthetic aperture can be written as in equation 1.8.

$$\theta_s = \frac{\lambda}{2L_s} = \frac{L}{2R_0} \tag{1.8}$$

where the factor of two takes into account the two-way path of the radar signal. Finally, the azimuth resolution of the synthetic aperture radar, Δ_a, is given by equation 1.9.

$$\Delta_a = R_0 \theta_s = \frac{L}{2} \tag{1.9}$$

From equation 1.9 it is possible to understand that the azimuth resolution of a synthetic aperture radar does not depend on the distance between the radar and the target, and there is not the need to have large real antennas because through the explained technique it is possible to synthesize a larger antenna. Obviously, the distance between the antenna and the target is limited by considerations related to the signal-to-noise ratio, which is constrained by the satellite power budget.

1.2. COSMO-SkyMed

COSMO-SkyMed system, funded by the Italian Space Agency and the Italian Ministry of Defence, is a constellation of four satellites, in low Earth orbit, each equipped with a multi-mode high-resolution SAR operating in X-band, Fig. 1.2.

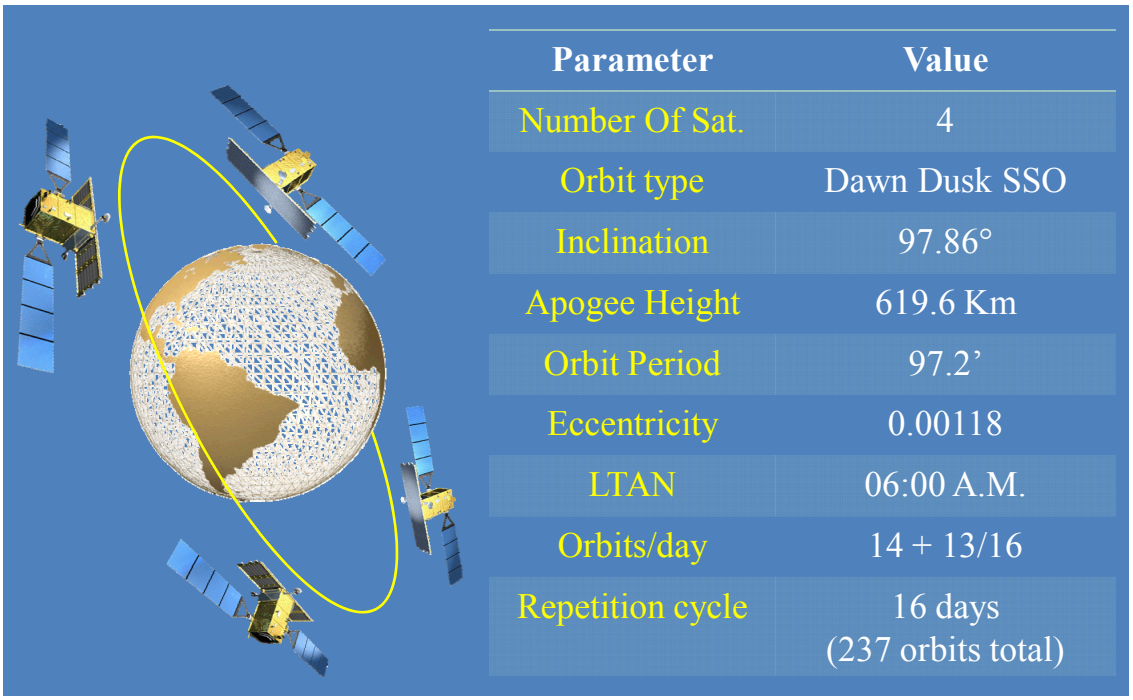

Parameter	Value
Number Of Sat.	4
Orbit type	Dawn Dusk SSO
Inclination	97.86°
Apogee Height	619.6 Km
Orbit Period	97.2’
Eccentricity	0.00118
LTAN	06:00 A.M.
Orbits/day	14 + 13/16
Repetition cycle	16 days (237 orbits total)

Fig. 1.2 – COSMO-SkyMed system characteristics.

In order to fulfil the requirements of different categories of users, the SAR is a multimode sensor which, in the civilian domain, can operate in, Fig. 1.3:

- Spotlight mode, for metric resolutions over small images (10km x 10km): in order to illuminate the scene for a time period longer than the one of the standard strip, during the acquisition time, the antenna is steered both in the azimuth and the elevation plane, increasing the length of the synthetic antenna and therefore the azimuth resolution. The acquisition is performed in frame mode and is limited in the azimuth direction, because of the antenna pointing.
- Stripmap mode, for metric resolutions (3m - 15m) over tenth of km images (40km x 40km): it represents the most common imaging mode, obtained by pointing the antenna along a fixed

direction with respect to the flight platform path. The antenna footprint covers a strip on the illuminated surfaces as the platform moves and the system operates. Two CSK Stripmap modes exist: the Himage and the PingPong. The latter implements a strip acquisition by alternating a pair of Tx/Rx polarization across bursts (cross-polarization).

- ScanSAR mode for medium to coarse (30m - 100m) resolution over large swath (100km^2 - 200km^2): two different implementations for CSK ScanSAR mode exist: WideRegion and HugeRegion.

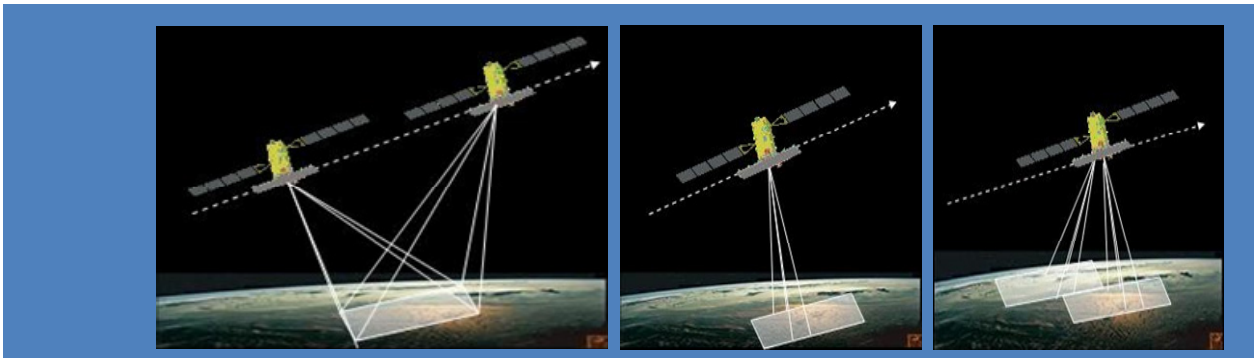

	Spotlight Smart	Spotlight Enhanced	Stripmap HImage	Ping-Pong	ScanSAR Wide	ScanSAR Huge
Resolution m x m	-	1 x 1	3 x 3	15 x 15	30 x 30	100 x 100
Swath km x km	-	10 x 10	40 X 40	30 X 30	100 X 100	200 X 200
Polarization	-	HH or VV	HH or VV or HV or VH	HH & VV HV & VV VV & VH	HH or VV or HV or VH	HH or VV or HV or VH

Fig. 1.3 – COSMO-SkyMed acquisition modes.

The CSK products can be divided in two classes: standard products and higher level products (for high level remote sensing applications). The standard products can have several processing levels, such as:

- Level 0 raw data: this data consist of time ordered echo data, obtained after decryption and decompression and after applying internal calibration and error compensation, it include all the auxiliary data required to produce the other basic and intermediate products;
- Level 1A, Single-look Complex Slant range (SCS) product: raw data focused in slant range-azimuth projection, that is the sensor natural acquisition projection;
- Level 1B, Detected Ground Multi-look (DGM) product: obtained by detecting, multi-looking and projecting the Single-look Complex Slant data onto a grid regular in ground. Spotlight products are not multi-looked;
- Level 1C/1D, Geocoded product, GEC (level 1C product) and GTC (level 1D product): obtained projecting the level 1A product onto a regular grid in a chosen cartographic reference

system. For level 1C product, the surface is the Earth ellipsoid, while for the level 1D product it is a Digital Elevation Model, which is used to approximate the real Earth surface. Level 1D products are constituted by the backscattering coefficient of the observed scene, multi-looked (except for Spotlight Mode), including the annexed the Incidence Angles Mask.

For standard use, the format adopted for products distribution is HDF5, which allows to store image layers as well as the ancillary information.

1.3. TanDEM-X

TanDEM-X (TDX) is an innovative formation flying radar mission whose primary aim is the acquisition of a global Digital Elevation Model with high accuracy (12 m horizontal and 2 m vertical), (Krieger, et al., 2012). This goal is obtained by extending the TerraSAR-X (TSX) mission by a second TSX-like satellite, i.e. TDX, flying in close formation with TSX. Both satellites form together a large single-pass SAR interferometer with a baseline which can be flexibly selected, allowing both the acquisition of single-pass cross-track interferograms and the exploitation for innovative applications of the along-track interferometry as well as bistatic techniques. TDX was developed in the frame of a public-private partnership between the German Aerospace Center (DLR) and EADS Astrium GmbH. The TanDEM-X mission was launched in June 2010 and started the operational activity in December 2010. The TSX satellite, as basis for TDX, was launched into a dusk-dawn sun-synchronous orbit (SSO) with 97.44° inclination in June 2007.

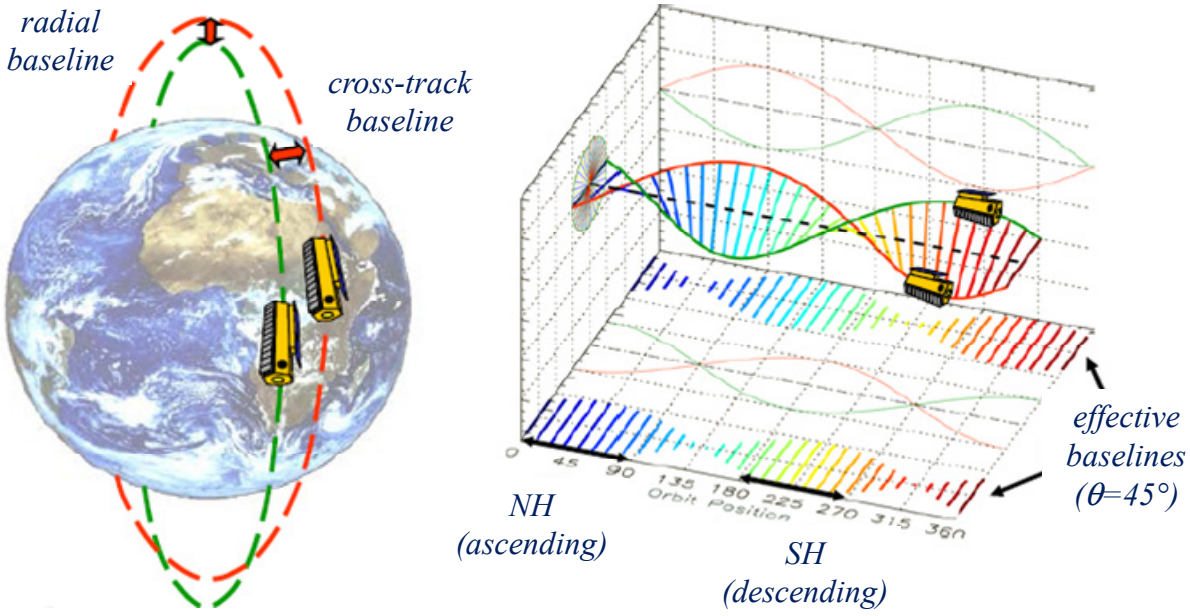

Fig. 1.4 – Helix formation for TSX-TDX satellites, (Krieger, et al., 2012).

The nominal orbit height is 514.8 km and the orbit repeat cycle is 11 days. TDX is very similar to TSX satellite, equipped with X-band SAR based on active phased array technology, which can be operated in Spotlight, Stripmap and ScanSAR mode with full polarization capability. TSX and TDX satellites fly in close Helix formation, Fig. 1.4, which combines an out-of-plane (horizontal) orbital displacement by different ascending nodes with a radial (vertical) separation by different eccentricity vectors resulting in a helix like relative movement of the satellites along the orbit, (Krieger, et al., 2012). Since there exists no crossing of the satellite orbits, arbitrary shifts of the satellites along their orbits are allowed, enabling safe operations without the need of autonomous control. Furthermore, at different latitudes it is possible to set the cross-track and along-track baseline components according to the application which has to be performed: cross-track interferometry aims at short along-track baselines to ensure an optimum overlap of the Doppler spectra and to avoid temporal decorrelation in vegetated areas; along-track interferometry or super resolution applications require along-track baselines in the range from hundred meters to several kilometers.

CHAPTER 2
SAR INTERFEROMETRY FOR DEM GENERATION

This Chapter focuses on a review of the state-of-the-art SAR interferometric techniques for DEM generation, analyzing all the relevant processing steps and deepening the study of the main options recently proposed in the literature to increase the accuracy of the interferometric processing. For a self-consistency of the overall work, all the elements required for a full understanding of the following part of the thesis, and in particular of the results of the experimental analysis conducted, will be presented in this Chapter.

2.1. SAR Interferometry

SAR interferometry (InSAR) usually refers to a SAR system or configuration which allows coherent correlation between multiple SAR acquisitions over the same target. The term InSAR is normally used for the across-track interferometric configuration, different from the along-track interferometric (ATI) configuration, which is commonly used for moving target detection (see Chapter 5). InSAR can be performed either through single-pass or repeat-pass acquisitions. A single-pass interferometer allows to overcome temporal decorrelation issues, while repeat-pass configuration, such as the one constituted by two CSK satellites, allows also to monitor changes occurring between the two acquisitions. Since in this case the temporal decorrelation is equal to one day, very good results can be achieved for DEM generation also through CSK repeat-pass interferometry, as proved in Chapter 4.

Considering two SAR acquisitions on the same target, u_1 and u_2, the complex correlation coefficient γ is defined as in equation 2.1.

$$\gamma = \frac{E[u_1 u_2^*]}{\sqrt{E[u_1 u_1^*]E[u_2 u_2^*]}} \tag{2.1}$$

where $E[...]$ is the mathematical expectation and * represents the complex conjugate.

The interferometric phase is defined as the phase of the complex correlation coefficient, as in equation 2.2.

$$\varphi = arg\{\gamma\} = arg\{E[u_1 u_2^*]\} \tag{2.2}$$

The two-dimensional map of the interferometric phase is called interferogram, which contains the interferometric phase fringes deriving either from SAR geometry, topography and surface displacement, each fringe corresponding to a 2π interferometric phase cycle.

The coherence is defined as the amplitude value of the complex correlation coefficient, as in equation 2.3, giving a measure of the quality of the interferogram.

$$\rho = |\gamma| \tag{2.2}$$

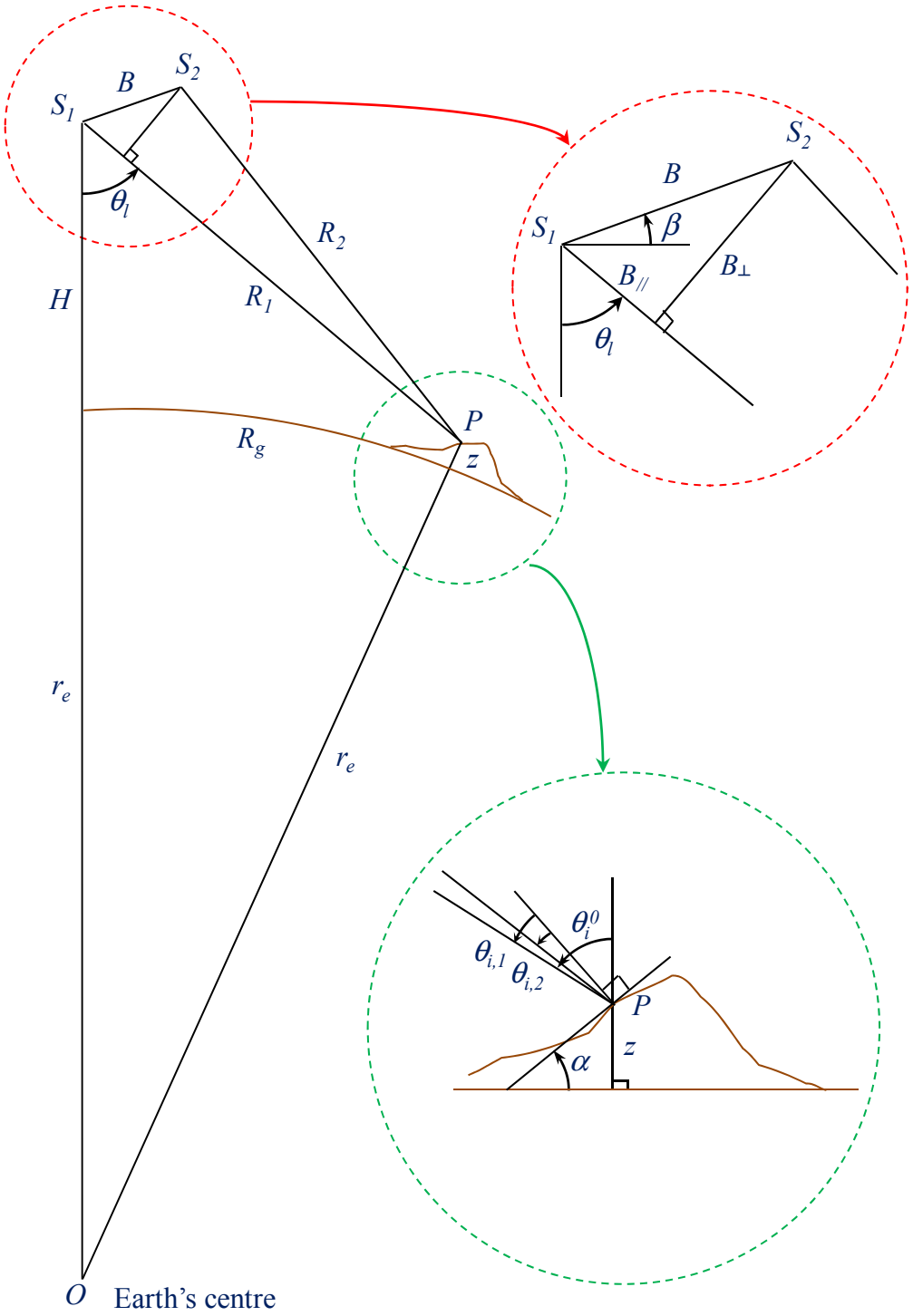

Fig. 2.1 – SAR interferometric configuration.

One of the possible interferometric formulations is proposed in the following part of this paragraph. Considering the interferometric configuration shown in Fig. 2.1, the target P is observed from two slightly different radar positions S_1 and S_2. The distance between S_1 and S_2 is called baseline, B. The look angle is θ_l. If the slant ranges difference is given by $\Delta R = R_2 - R_1$, then the measured interferometric phase is given by equation 2.3, which represents 2π times the round-trip distance difference in wavelengths.

$$\varphi = -\frac{4\pi}{\lambda}\Delta R \tag{2.3}$$

By applying the law of cosines to the triangle S_1PS_2, ΔR can be written as in equation 2.4.

$$\Delta R = \sqrt{R_1^2 + B^2 - 2R_1 B sin(\theta_l - \beta)} - R_1 \tag{2.4}$$

Then, from the measurement of the interferometric phase φ, knowing the baseline and the other geometric parameters in equation 2.4, equation 2.4 can be solved to obtain the look angle θ_l. Since different targets at the same distance from the SAR, i.e. the same slant range, but with different look angles are imaged at the same point because of the intrinsic SAR geometry, by knowing the slant range of the target with respect to S_1 and through equation 2.4 it is possible to solve the look angle ambiguity. With this information, it is possible to obtain the exact location of the target, in terms of topographic elevation z and ground range R_g, considering the triangle S_1OP, through equation 2.5.

$$\begin{gathered} \mathrm{z} = \sqrt{(r_e + H)^2 + R_1^2 - 2R_1(r_e + H)cos\theta_l} - r_e \\ R_g = r_e sin^{-1}\left(\frac{R_1}{r_e + z} sin\theta_l\right) \end{gathered} \tag{2.5}$$

From equation 2.3 and the first equation 2.5 it is possible to assess the height sensitivity of InSAR, meaning how much the interferometric phase changes for a certain variation of the surface elevation, equation 2.6.

$$\frac{\partial \varphi}{\partial \mathrm{z}} = \frac{4\pi}{\lambda}\frac{Bcos(\theta_l - \beta)}{R_1 sin\theta_l} \cdot \left(\frac{R_1}{r_e + H} \cdot \frac{\sqrt{(r_e + H)^2 + R_1^2 - 2R_1(r_e + H)cos\theta_l}}{\sqrt{R_1^2 + B^2 - 2R_1 B sin(\theta_l - \beta)}}\right) \tag{2.6}$$

According to (Zebker, et al., 1986), the minor term in brackets can be neglected and using the parallel ray approximation, the height sensitivity can be given as in equation 2.7.

$$\frac{\partial \varphi}{\partial z} \approx \frac{4\pi}{\lambda} \frac{B_{\perp}}{R_1 sin\theta_l} \tag{2.7}$$

Where $B_{\perp}$ is the normal baseline, which represents the baseline component perpendicular to the SAR looking direction.

According to (Bamler, et al., 1998), the height of ambiguity H_a, defined as the height resulting in a phase variation of one fringe (2π), is given by equation 2.8.

$$H_a = 2\pi \frac{\partial z}{\partial \varphi} \approx \frac{\lambda}{2} \frac{R_1 sin\theta_l}{B_{\perp}} \tag{2.8}$$

The height of ambiguity is inversely proportional to the perpendicular baseline, and in the interferogram it represents a fringe. Larger the perpendicular baseline, smaller the height of ambiguity, more difficult the phase unwrapping process.

From previous equations, it is possible to understand that a sufficiently large normal baseline $B_{\perp}$ is necessary to achieve a high sensitivity to topographic variations and for accurate topographic reconstruction. However, the upper value of $B_{\perp}$ is limited by the spatial decorrelation that reduces the coherence level and the quality of the interferogram, which becomes more difficult to unwrap because of the dense fringes, (Li, et al., 1990).

The interferometric phase fringes number in slant range is given by equation 2.9, (Bamler, et al., 1998).

$$k_{\varphi} = \frac{1}{2\pi} \frac{\partial \varphi}{\partial R_1} \approx \frac{2B_{\perp}}{\lambda R_1 tan\left(\theta_i^0 - \alpha\right)} \tag{2.9}$$

where α is the surface slope as in Fig. 2.1, positive towards the SAR looking direction, and θ_i^0 is the nominal incidence angle when $\alpha = 0°$. Equivalently, the interferometric phase fringes frequency in the fast time domain (range time) is given by equation 2.10, (Gatelli, et al., 1994).

$$f_{\varphi} = \frac{1}{2\pi} \frac{\partial \varphi}{\partial t} \approx \frac{cB_{\perp}}{\lambda R tan\left(\theta_i^0 - \alpha\right)} \tag{2.10}$$

obtained from equation 2.9 and from the two-way travel time relation $2R = ct$.

The main processing steps which allow to generate a DEM from a SAR interferometric pair are listed hereinafter and will be analyzed in the following paragraphs:

- Dataset selection;
- Coregistration;

- Coherence map and interferogram generation;
- Phase unwrapping;
- Phase-to-Height conversion;
- DEM geocoding.

2.2. Dataset Selection

To perform SAR interferometry for DEM generation, the dataset selection is an important step, and some significant principles, such as:

- The temporal baseline between the two interferometric acquisitions shall be as low as possible, to reduce decorrelation and loss of coherence.
- If the perpendicular baseline is too small, the generated interferogram will be easy to unwrap, but the topographic sensitivity can be too poor or the height of ambiguity can be even higher than the topographic variation over the scene, there will be a high sensitivity to phase noise and atmospheric effects.
- If the perpendicular baseline is too high, the topographic sensitivity will increase, but the generated interferogram will be difficult or almost impossible to unwrap for not smooth topographies and the coherence will be very small because of the high geometrical and volume scattering decorrelation. The coherence is totally lost for a critical baseline value, B_c, defined as in equation 2.11.

$$B_{cr} = \frac{\lambda R tan(\theta)}{2R_r} \tag{2.11}$$

  where λ is the acquisition wavelength, R is the slant range distance, R_r is the pixel spacing in slant range and θ is the acquisition incidence angle. For the critical baseline, the correlation between the received signals is zero.
- If possible, a combined use of small baseline and large baseline interferograms gives the best results, taking advantage of the small baseline interferogram to help unwrapping larger baseline interferograms, and combining them in order to reduce the atmospheric artifacts.
- Since coherence value is affected by local weather, it shall be avoided to acquire the interferometric pair during rain, snow or strong wind, which cause a loss of phase coherence. Images acquired during night are usually less affected by atmospheric effects, (Hanssen, 1998). Equally, acquisitions shall not be made during hot days or during a wet season, because of the higher quantity of water vapor, (Hanssen, 1998).

- The scenes selected to perform interferometry shall be preferably not vegetated areas, because of their very low decorrelation time.

2.3. SAR Coregistration

The SAR interferometric processing takes as input data two Single-look Complex Slant-range (SCS) images, referred to as a "master" and a "slave", and a low resolution DEM, which is used to estimate and compensate for topography in the final interferogram, together with the satellite orbits, and to provide an optimal removal of the "baseline decorrelation". If a low resolution input DEM is not available, the final interferogram will be compensated for an ellipsoidal Earth, or "flattened".
From the input DEM and from the knowledge of timing information and precise sensor orbits a synthetic interferogram can be generated. The interferogram phase is estimated by computing, for each target P in the (azimuth, slant range) plane, the difference in the sensor-target travel path distance for the two satellites, equation 2.12.

$$\varphi(P) = \frac{4\pi}{\lambda}[R_1(P) - R_2(P)] \approx \frac{4\pi B_\perp}{\lambda R_0}\Delta R(P) \tag{2.12}$$

The synthetic interferogram provides a field of unwrapped phase which can be used for images coregistration and for spectral shift filtering.
The coregistration aim is to guarantee that each ground target contributes to the same (range, azimuth) pixel in both master and slave image. If, ideally, the orbits were perfectly parallel and the acquisitions were aligned, coregistration step would only need to compensate for the different geometry by a proper cross-track stretching of one image. Actually, also several other contribution shall be taken into account, and the required transformation is mainly composed of a small rotation of the two images, a range and an azimuth stretch, with a change in sampling rate, and further second-order actions.
An appropriate alignment between the two images should be performed on a pixel by pixel basis, with an accuracy in the order of at least 1/10 of the resolution to avoid a significant loss of phase coherence. A map of pixel-to-pixel correspondence can be provided by the synthetic fringes, scaled by the wavelength. Since coregistration depend also on the local topography, in the next paragraph also a DEM will be taken into account for coregistration. In this paragraph, the assumption of ellipsoidal Earth surface is made, and the coregistration map can be provided as a smooth polynomial that approximate the pixel-to-pixel shift. If sensor velocity and attitude are sufficiently

stable, the master-slave deformation can be approximated, in general, by the second terms in equation 2.13.

$$\begin{cases} r_s = a \cdot r_m^2 + b \cdot r_m + c \cdot a_m + d \\ a_s = e \cdot r_m^2 + f \cdot r_m + g \cdot a_m + h \end{cases} \tag{2.13}$$

where (r_m, a_m) are the range and azimuth coordinates of the master image and (r_s, a_s) are the range and azimuth coordinates where the slave image should be evaluated. Conventionally, the slave image is the image which is re-sampled, then the interferogram is in the same (slant range, azimuth) reference of the master image.

According to (Ferretti, et al., 2007), the coefficients in equation 2.13 represent the following transformation:

- A fixed azimuth shift, coefficient d, due for instance to different timing along orbit, and a fixed range shift, coefficient h, due to the perpendicular baseline component;
- A stretch in range, coefficient b, due to the normal baseline variation with range, and an azimuth stretch, coefficient g, due to the possible variation in PRF (i.e. pulse repetition frequency) or in satellite velocity;
- A range and azimuth skew, coefficients c, f which approximate an image rotation for small rotation angles;
- Two second order terms, coefficients a, e, applicable for instance to large range swaths.

A way to obtain the values of these coefficients consists in exploiting the known acquisition geometry, $\Delta R(P)$ already computed in equation 2.12 for synthetic interferogram generation, to perform a Least Mean Square regression based on a regular grid of points distributed all over the image.

Another more accurate way to estimate the coregistration coefficients consists in dividing each image into small patches and finding the range and azimuth offset for each patch by maximizing some statistical measure, such as amplitude cross-correlation or fringe contrast, (Bamler, et al., 1998), (Moreira, et al., 2000). Finally, a smooth polynomial is fitted all over the measures, for instance through Least Mean Square regression, weighted according to the local SNR estimates, such as the amplitude normalized correlation coefficient or the absolute value of coherence. Referring to the statistical measure to maximize, fringe-based and amplitude-based techniques have different advantages and drawbacks, the first ones perform better for flat topography or small baselines because the fringes vary slowly, while the latter ones work better for larger baselines and are less computationally demanding at the cost of a coarser accuracy.

After coregistration coefficients have been estimated, the slave image can be re-sampled according to the polynomial mapping in equation 2.13, which can be split in two one-dimensional re-sampling steps, along range and then along azimuth, which can be efficiently performed in the space domain.

2.3.1. DEM-assisted SAR Coregistration

According to the previous paragraph, in conventional interferometric coregistration techniques for SAR data, a bi-dimensional low degree polynomial is chosen as warp function, and the coregistration parameters are estimated through least squares fit from the shifts measured on image windows. However, in case of steep topography or large baselines, the polynomial approximation may lead to errors which increase with the spatial resolution. In (Nitti, et al., 2011), a DEM-assisted SAR coregistration procedure is proposed to provide a better prediction of the offset vectors even in the previously mentioned cases. While in the classical approach the shifts are estimated on a limited number of patches and then a polynomial approximation is used for the transformation, according to this approach the correspondence between master and slave image is computed pixel by pixel by using the orbital data and a reference DEM. In particular, a geometric model is introduced to compute the range shifts between master and slave as a function of the 3D position of any point on the Earth surface, which is locally well approximated by spherical models to simplify the equations, in the assumption of zero-Doppler side-looking geometry.

Referring to Fig. 2.2 and according to the model proposed in (Nitti, et al., 2011), having in input precise orbits, assumed to be parallel, and a reference DEM radar coded in the master geometry, it is possible to retrieve analytically the pixel offset between master and slave along the slant-range direction at every master slow-time instant. In particular, for each master pixel p_1, the position of the corresponding slave pixel p_2 shall be estimated. The slave height H_2 is related to the master height H_1 through the equation 2.14.

$$r_e + H_2 = \sqrt{(r_e + H_1)^2 + B^2 - 2B(r_e + H_1)cos\alpha} \tag{2.14}$$

For a given pixel p_σ belonging to the master or to the slave, $\sigma \in \{1,2\}$, the master and slave slant-range distances R_σ are related to the corresponding two-way zero-Doppler range fast times τ_{p_σ} through equation 2.15.

$$\begin{aligned} \tau_{p_\sigma} &= \tau_{\sigma 0} + \frac{p_\sigma}{f_s} \\ R_\sigma &= \frac{c}{2}\tau_{p_\sigma} = \frac{c}{2}\left(\tau_{\sigma 0} + \frac{p_\sigma}{f_s}\right) \end{aligned} \tag{2.15}$$

where c is the speed of light, f_s the range sampling rate and $\tau_{\sigma 0}$ are the two-way zero-Doppler range times for the first range pixels in the master and slave images.

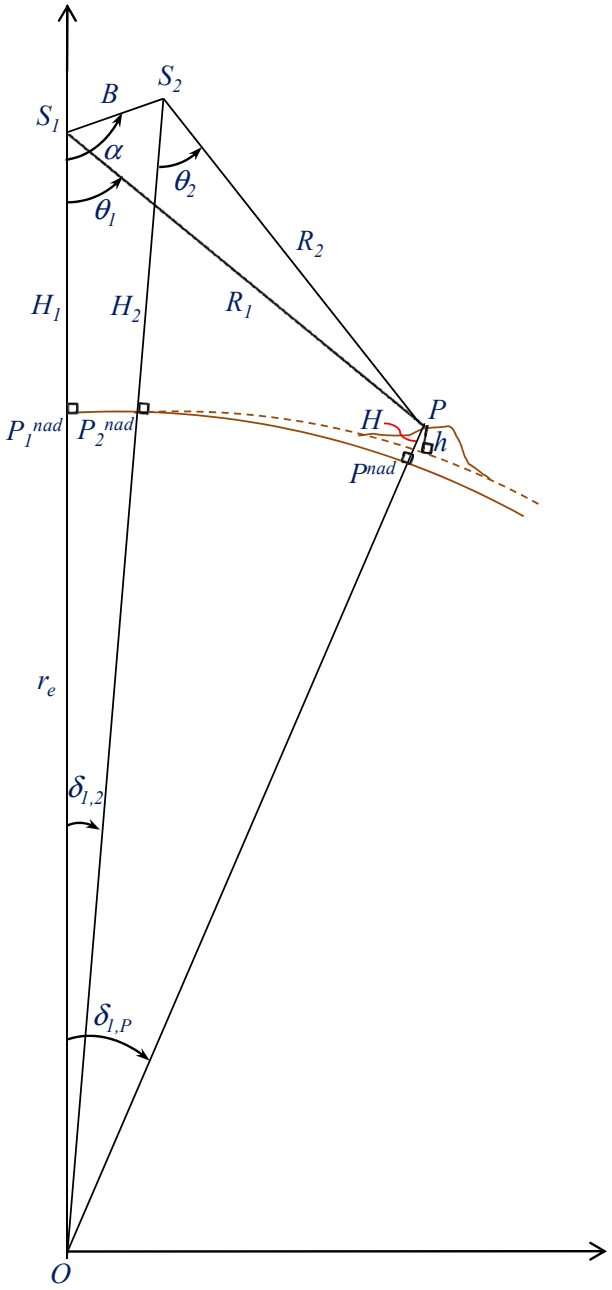

Fig. 2.2 – SAR interferometric geometry, according to the model proposed in (Nitti, et al., 2011). The dotted brown line is the reference ellipsoid (WGS84) while the solid brown line is its circular approximation.

Therefore, the pixel offsets between the master and slave along the range direction are given by equation 2.16.

$$\Delta p = p_2 - p_1 = f_s\left(2\frac{R_2}{c} - \tau_{20}\right) - p_1 = f_s\left[\frac{2}{c}(R_2 - R_1) + (\tau_{10} - \tau_{20})\right] \qquad (2.16)$$

According to Fig. 2.2, for each master pixel p_1, R_1 is expressed by equation 2.15, and the problem is reduced to the estimation of the slant range distance R_2, which can be estimated numerically by combining equations 2.17 into equation 2.18 and solving for R_2.

$$\begin{gathered}\frac{\sin\delta_{1,2}}{B}=\frac{\sin\alpha}{r_e+H_2}\\ \frac{\sin\delta_{1,P}}{R_1}=\frac{\sin\theta_1}{r_e+H}\\ \frac{\sin\left(\delta_{1,P}-\delta_{1,2}\right)}{R_2}=\frac{\sin\theta_2}{r_e+H}\\ \cos^2\theta_\sigma=\frac{(r_e+H_\sigma)^2+R_\sigma^2-(r_e+H)^2}{2R_\sigma(r_e+H_\sigma)}\end{gathered} \tag{2.17}$$

$$\begin{gathered}\arcsin\left[\frac{R_1}{r_e+H}\sqrt{1-\frac{(r_e+H_1)^2+R_1^2-(r_e+H)^2}{2R_1(r_e+H_1)}}\right]+\\ -\arcsin\left[\frac{R_2}{r_e+H}\sqrt{1-\frac{(r_e+H_2)^2+R_2^2-(r_e+H)^2}{2R_2(r_e+H_2)}}\right]=\arcsin\frac{B\sin\alpha}{r_e+H_2}\end{gathered} \tag{2.18}$$

By using equations 2.16, 2.17 and 2.18, the pixel offset between master and slave images can be expressed as the product of the range sampling rate f_s and a function of the normal and parallel baseline components and of the topographic height H above the adopted spherical model, which is close to the height h above the reference ellipsoid.

2.4. Coherence Map and Interferogram Generation

An interferogram can be generated through a pixel-to-pixel computation of the Hermitian product of two co-registered SCS SAR images u_1 and u_2, equation 2.19, previously filtered in order to remove the uncorrelated spectral contributions in range due the frequency shift in the reflectivity caused by a change in the look angle, (Gatelli, et al., 1994), and in azimuth due to the frequency shift caused by a change in the squint angle (variation of the antenna pointing, Doppler Centroids between the two acquisitions), (Fornaro, et al., 2001), as further analyzed in Chapter 4.

$$u_1u_2^*=|u_1u_2^*|e^{j(\varphi_1-\varphi_2)}=Ue^{j\varphi} \tag{2.19}$$

where φ_1 and φ_2 represent the phase of u_1 and u_2, * represents the complex conjugate, U is the Hermitian product amplitude and φ is the interferometric phase, or the phase difference.

The interferogram is registered in the same reference of the master image, and it is usually referred to as a "raw interferogram" because of the noisy phase, which contains phase fringes mainly from the system geometry and the topography. The phase fringes originated by the system geometry should be removed through an *Earth flattening* procedure. In particular, the interferometric phase fringes number due to system geometry, in slant range, from equation 2.9 when $\alpha = 0°$, is given by equation 2.20.

$$k_{\varphi_0} = \frac{2B_\perp}{\lambda R tan\theta_i^0} \tag{2.20}$$

where φ_0 is the phase difference originated by the system geometry. The fringe number from InSAR geometry is strongly dependent on the normal baseline, and should be removed before estimating the coherence. The interferometric phase due to system geometry can be compensated by considering the elliptical Earth surface, such as WGS84, where the surface elevation z is zero, through equation 2.21, referring to Fig. 2.1.

$$\begin{aligned} \theta_i^0 &= cos^{-1}\left(\frac{R_1^2 + (r_e + H)^2 - r_e^2}{R_1(r_e + H)}\right) \\ \varphi_0 &= \frac{4\pi}{\lambda}\Delta R|_{z=0} \\ \Delta R|_{z=0} &= \sqrt{R_1^2 + B^2 + 2R_1 B sin\left(\theta_i^0 - \beta\right)} - R_1 \end{aligned} \tag{2.21}$$

Finally, the interferometric phase due to system geometry, φ_0, can be removed by the interferogram through equation 2.22, to obtain the Earth flattened interferogram.

$$\varphi_{flat} = \varphi - \varphi_0 \tag{2.22}$$

Furthermore, a common practice to reduce the noise in the interferogram is represented by the averaging of adjacent pixels in the complex interferogram, process which is defined complex multi-looking. The trade-off to make during multi-looking is between the geometric resolution and the phase accuracy, which in turn affects the DEM vertical accuracy. The multi-looking is able to mitigate the uncorrelated noise due to temporal, spatial, volume decorrelation, but it is not able to remove space-correlated artifacts such as atmospheric noise, flattening errors, etc.

The coherence is the absolute value of the complex correlation coefficient in equation 2.1, which provides a measure of the interferogram quality, of the SNR. It is obtained from the complex Earth-flattened interferogram through equation 2.23.

$$|\gamma| = \frac{\left|\sum_{l=1}^{L}|u_1(l)||u_2^*(l)|e^{j\varphi_{flat}}\right|}{\sqrt{\sum_{l=1}^{L}u_1(l)u_1^*(l)}\sqrt{\sum_{l=1}^{L}u_2(l)u_2^*(l)}} \tag{2.22}$$

where L is the size of the averaging window, which is determined by a trade-off between spatial resolution and unbiased coherence estimation. For unbiased coherence estimation, the scene shall be locally stationary and ergodic within the averaging window. Therefore, a small averaging window guarantees high spatial resolution at the cost of a biased coherence estimation towards higher values in low coherence areas, (Touzi, et al., 1999), while a large averaging window can lead to a coherence underestimation for inhomogeneous scenes especially on steep slopes.

Two SAR acquisitions at a baseline equal or greater than the critical baseline B_{cr} by definition entail a complete loss of coherence. Therefore, unless the "non-cooperating" wave number components (i.e. the useless parts of the spectrum of the signal) are filtered out, on flat terrain the coherence of the two acquisitions will decrease linearly if the normal baseline increases, becoming zero when the critical baseline is reached, equation 2.23.

$$\gamma_b = 1 - \frac{B_n}{B_{cr}} \tag{2.23}$$

When the terrain slope significantly changes in range or azimuth, the situation is more complex because the filter necessary to remove the useless components of the spectrum become space varying. If the terrain slope changes so quickly to become significant within a resolution cell, it is not possible to avoid a coherence loss due to the volume effect, (Fornaro, et al., 2001). Other causes affecting coherence value will be analyzed in the following Chapters of the Thesis.

2.5. Phase Unwrapping

The interferometric phase is known only modulo-2π, it is ambiguous, because the height variation in the area of interest can entail hundreds of cycles. Therefore, in order to estimate the topography from the interferometric phase, it is necessary to unwrap the phase. The aim of phase unwrapping is to recover the integer number of cycles n to be added to the wrapped phase φ in order to obtain the unambiguous phase value ψ for each pixel, equation 2.24.

$$\psi = \varphi + 2\pi \cdot n \tag{2.24}$$

If no a priori information concerning φ is available, there is not any given constraint to the solution and the phase unwrapping problem is an ill-posed inverse problem with an infinite number of different possible solutions.

The simpler phase unwrapping technique would be an integration of the phase differences starting from a reference point, however the existing phase discontinuities actually would make the results inaccurate.

Phase unwrapping algorithms usually assume that the true unwrapped phase field is smooth and slowly changing, therefore adjacent phase values are assumed to be within a one-half cycle (i.e. π). If some phase discontinuities arise, they cause inconsistencies because the integration yields different results depending on the followed path, which can be verified if the sum of the wrapped phase differences around a closed path differs from zero.

To be consistent, a gradient field must be irrotational, meaning that the curl of the phase gradient should be zero everywhere, (Goldstein, et al., 1988), equation 2.25.

$$\boldsymbol{\nabla} \wedge \boldsymbol{\nabla}\varphi = \mathbf{0} \tag{2.25}$$

It is quite rare that this condition is verified over the whole interferogram. If the sum of the wrapped phase differences around the closed paths formed by each mutually neighboring set of four pixels is not zero, the rotational component of the gradient field is not zero, and a residue exists, (Goldstein, et al., 1988), whose value is usually normalized to one cycle and can be positive or negative. The sum of the wrapped phase variations along an arbitrary closed path is equal to the algebraic sum of the residues enclosed in that path, (Ferretti, et al., 2007). The main issue is the complete identification of the phase residues, which are related to the discontinuities, and can be mainly caused by phase noise, particularly in repeat-pass interferometry, or steep terrain slopes. In general, the number of discontinuities is a function of the local topography, the off-nadir angle, the normal baseline and the decorrelation noise, (Ferretti, et al., 2007).

Several algorithms exist to cope with phase discontinuities, and almost all are aimed at minimizing the cost function in equation 2.26, (Ghiglia, et al., 1996), (Chen, et al., 2000).

$$\mathrm{C} = \left\{ \sum_{i,j} w_{i,j}^{(r)} \left| \Delta^{(r)} \psi_{i,j} - \Delta_w^{(r)} \varphi_{i,j} \right|^p + \sum_{i,j} w_{i,j}^{(a)} \left| \Delta^{(a)} \psi_{i,j} - \Delta_w^{(a)} \varphi_{i,j} \right|^p \right\} \tag{2.26}$$

where $0 \leq p \leq 2$, Δ indicates a discrete differentiation respectively along range (r) and azimuth (a), w represent the weights defined by the user, the summations are over appropriate rows i and columns j, and Δ_w means that the phase differences are wrapped in the interval $[-\pi; +\pi]$. Equation

2.26 is a mathematical representation of the basic assumption that $\Delta\psi = \Delta_w\varphi$ almost everywhere. The minimum L^p-norm gives efficient algorithms for $p = 2$ and $p = 1$.

2.5.1. Un-weighted Least Mean Squares Method

Assuming $p = 2$ and no weights, $w_{ij} = 1\ \forall_{ij}$, equation 2.26 leads to the linear system of equations 2.27, which can be solved with some boundary conditions.

$$\begin{aligned} \psi_{i+1,j} - \psi_{i,j} &= \Delta_w^{(a)}\varphi_{i,j} \\ \psi_{i,j+1} - \psi_{i,j} &= \Delta_w^{(r)}\varphi_{i,j} \end{aligned} \tag{2.27}$$

The system of equation 2.27 is over-constrained, there are two gradient estimates for each phase, and it can be formulated in a normal equation form $\boldsymbol{G^T G\psi = G^T d}$, where the data vector $\boldsymbol{d}$ is the vector form of the wrapped phase differences estimated from the interferogram, while the model matrix $\boldsymbol{G}$ is an incidence matrix whose non-zero elements assume the value +1 or -1, (Ferretti, et al., 2007). Many efficient numerical solutions exist for this matrix, (Strang, et al., 1997), considering at least one pixel of known elevation.

The main drawback of this method is that the number and the position of phase discontinuities are not taken into account and can cause severe errors which are propagated by the equations, (Ferretti, et al., 2007). The solution is congruent with the data only if no discontinuities exist, $\psi = \varphi + 2\pi n$.

2.5.2. Weighted Least Mean Squares Method

If weights are used in the equations, the results improve. The coherence map can be used to identify areas where phase discontinuities can occur with a higher probability, (Ghiglia, et al., 1996), losing on the other hand the regular structure of the matrix to be inverted. Therefore, it is necessary to apply iterative numerical techniques, increasing the computational effort. For a correct phase reconstruction, zero weights should be applied where phase discontinuities arise, and unitary weights where the phase gradient is correct, but this would imply the identification of the cycle skips, which is the issue that this method should avoid, (Ferretti, et al., 2007). According with (Spagnolini, 1995), the phase artifacts in the estimated unwrapped phase field due to noise can be reduced if local phase gradient are estimated on large windows using FFT analysis. The problem is a variational surface reconstruction problem from indirect measurements, well known in the field of computer vision, (Ferretti, et al., 2007). Also this method, like the previous one, gives solutions which are not congruent with the original interferogram, except if no discontinuities exist. The

solution can be forced to be congruent with the data, by rounding the difference between the wrapped and unwrapped phase to the nearest integer number of cycles, but it is not equivalent to minimizing the cost function in equation 2.26 with the integer constraint, (Ferretti, et al., 2007).

2.5.3. Minimum Cost Flow Method

According to (Costantini, 1998), the Minimum Cost Flow phase unwrapping approach, based on network programming, efficiently allows to globally minimize the cost function in equation 2.26 under the weighted L^1-norm (minimum absolute deviation). The phase unwrapping is formulated as a constrained optimization problem, where the integer number of cycles to be added to the phase variations is minimized to make them consistent, meaning that the gradient field must be irrotational. Therefore, the constraint to be satisfied is the equation 2.25, and the Minimum Cost Flow method adds an integer number of cycles to every wrapped phase value. As for the Weighted Least Mean Squares method, it is possible to define proper weights to distinguish the areas where the probability of phase discontinuities is higher. The unwrapped phase field is congruent with the original interferogram.

2.5.4. Branch-Cut Method

Assuming $p = 0$, the gradients of the estimated unwrapped phase field exactly equal the data in as many places as possible, (Ferretti, et al., 2007). The branch-cut method, (Goldstein, et al., 1988), aims at unwrapping the interferogram selecting only the integration paths which lead to self-consistent solutions. The rotational part of the estimated phase gradient, which is the residue field, is used to lead the integration along a consistent path, limiting the error propagation, (Ferretti, et al., 2007). Since the sum of the wrapped phase variations along a closed path is equal to the algebraic sum of the residues enclosed in that path, and since integration paths associated to a net "charge" should be avoided, oppositely-charged residues are connected with branch cuts, like straight lines, which cannot be crossed by the integration paths. The main issue of this method is that in low coherence areas, the cuts can close on themselves, entailing holes in the unwrapped phase field in correspondence to low SNR areas.

2.5.5. Other Methods

Other phase unwrapping algorithms exist and can be efficiently used for InSAR processing, such as Region Growing techniques, (Xu, et al., 1999), which was designed to handle noisy interferograms,

according to whom the unwrapping is performed on the perimeter of "growth regions", which can grow with consistency checking, and phase information from adjacent pixels is used to predict the correct phase of each new pixel to be unwrapped. Furthermore, a reliability check is applied to each unwrapping attempt. Another phase unwrapping approach is based on Kalman Filters, (Kramer, et al., 1996), or if more interferograms are available on the same scene, a Multi-Baseline Phase Unwrapping algorithm can be applied, (Ferretti, et al., 1997). In fact, phase unwrapping from a single interferogram is an ill-posed inverse problem, and even in high coherence areas the phase aliasing can generate significant artifacts on the estimated topography. On the contrary, of several interferograms on the same area are available, with different baseline values, it is possible to combine the data to suppress phase ambiguities, limiting the impact of the noise.

Finally, different techniques which allow to by-pass the phase unwrapping step will be analyzed in Chapter 3.

2.6. Phase-to-Height Conversion and DEM Geocoding

After having performed phase unwrapping, every pixel can be localized with respect to a Cartesian reference system. Therefore, the aim of the phase-to-height conversion step is to pass from radar coordinates in range and azimuth and from unwrapped phase variation on the scene, to a description of the local topography, knowing the acquisition geometry and the satellite orbit positions of master and slave images. Phase-to-height conversion techniques can be divided in two groups, (Small, et al., 1996), depending if they work on the flattened phase or on the un-flattened interferogram. The most accurate methods operate on the un-flattened interferogram, the flattening phase terms are deterministic and known, and they can be added back to the data after unwrapping, even if commonly the unwrapping algorithms work on flattened data. Through one of the different possible methods reviewed in (Small, et al., 1996), this processing step allows to determine the relationship between the heights and the unwrapped phase differences.

Finally, DEM geocoding is important to generate a product in a standard format. It is assumed that for CSK the accuracy of the satellites state vectors allows precise data geocoding without any GCPs. Initially the data geocoding problem is described when the target height in known a priori, and then the procedure is extended to interferometric data, (Ferretti, et al., 2007).

An Earth-Centered Earth-Fixed (ECEF) reference frame is assumed, and the target is considered motionless. If the local topography is known, the target coordinates are determined by the solution of three equations, (Curlander, 1982), such as:

- Range equation;
- Doppler equation;

- Earth model equation.

Each pixel $P = P\{r, t\}$ of the image is identified by its azimuth time t and its slant range coordinate r. Considering a zero-Doppler focusing, (Curlander, et al., 1991), the Cartesian coordinates $P = P\{X, Y, Z\}$ of the target have to satisfy the equations 2.28, the first one is the range equation representing a sphere of radius r centered in $S(t)$, the second one is the Doppler equation, describing a plane orthogonal to V_{PS}.

$$\begin{aligned} |\boldsymbol{P} - \boldsymbol{S}(t)| &= r = r_{ca} + r_s \cdot n_r \\ \big(\boldsymbol{P} - \boldsymbol{S}(t)\big) \cdot \boldsymbol{V_{PS}}(t) &= 0 \end{aligned} \tag{2.28}$$

where:

- r_{ca} is the distance between the sensor and the first sample of the range line;
- r_s is the range step;
- n_r is the sample of the range line under consideration;
- V_{PS} is the sensor-target relative velocity;
- $S(t)$ is the satellite Cartesian coordinates at the azimuth time t.

In order to localize P, a third equation is needed, and can be represented by the Earth model equation 2.29 if the height of the target with respect to a reference ellipsoid, z, is known.

$$\frac{X^2 + Y^2}{(r_e + z)^2} + \frac{Z^2}{r_p^2} = 1 \tag{2.29}$$

where:

- r_e is the Earth equatorial radius;
- $r_p = (1 - f)(r_e + z)$, with f which is the flattening factor of the reference ellipsoid.

The non-linear system of these three equations can be solved for $P = \{X, Y, Z\}$ through an iterative numerical technique, (Schreier, 1993).

According to (Curlander, et al., 1991), as opposed to optical sensor, for SAR sensors the attitude information is not required, if sensor position and velocity vectors are sufficiently accurate, in order to achieve accurate location information through this procedure.

If the geocoding concerns interferometric data and z is unknown, the equation 2.29 cannot be used. However, the target coordinates can be estimated using the unwrapped interferometric phase ψ and the state vectors relative to the second radar acquisition. In particular, for the slave sensor it is possible to write the equations 2.30.

$$\begin{aligned} |\boldsymbol{P} - \boldsymbol{S_{slave}}(t_{slave})| &= r + \frac{\lambda}{4\pi}\psi \\ \left(\boldsymbol{P} - \boldsymbol{S_{slave}}(t_{slave})\right) \cdot \boldsymbol{V_{PS_{slave}}}(t_{slave}) &= 0 \end{aligned} \tag{2.30}$$

where, in general, $t = t_{master} \neq t_{slave}$. Therefore, the system of four equations 2.28 and 2.30 in four unknowns (X, Y, Z, t_{slave}) can be solved.

Finally, in order to obtain a standard product which can be compared with other similar products, it is necessary to perform a data re-sampling, since the uniform image grid in slant range and azimuth coordinates generate a non-uniform sampling in the geographical coordinates in terms of latitude and longitude, depending on the local topography. Therefore, it is necessary to perform an interpolation to obtain a constant sampling step in the final product. Several interpolator exist, such as the *nearest neighbor*, the *Delaunay triangulation and linear interpolation*, the *inverse distance weighting*, the *Kriging interpolation*, (Wackernagel, 1998).

2.7. Digital Elevation Models: Application Domains and Standards

The availability of high accuracy DEM products is an enabling factor for several applications which need a deep knowledge of the Earth surface. A list of different potential fields of applications is proposed, they are very diversified and continuously increasing in number:

- Topography;
- Air and surface based weapon system navigation;
- 3D visualization;
- Airport landing approach mapping;
- Helicopter landing zones;
- Go/No-Go route planning based on slope assessment;
- Mobility analysis/slope;
- Cross-country movement / trafficability analysis;
- Ingress/Egress route planning;
- Intelligence preparation of the battle-space;
- Force protection;
- Ambush assessment models;
- Auto-Ground collision avoidance system for military aircrafts;
- Surface analysis;
- Improved crisis intervention planning;
- Situational awareness;

- Base mapping;
- Target analysis;
- Modeling and simulation;
- 3D Flight mission planning (aircrafts, missiles, etc);
- 3D Flight simulation;
- Aerial and satellite images orthorectification and geometric correction;
- Line-of-sight analysis;
- Electromagnetic propagation analysis for telecommunication applications;
- Communication tower placement;
- Road and hydro-infrastructure design;
- Land cover/soils analysis;
- Prediction of impact of emergency situations;
- Hydro basins study and modeling of floods and landslips.

Furthermore, a higher DEM absolute vertical accuracy is fundamental to achieve a higher geolocation accuracy of the images geo-coded using that DEM, as further analyzed in Chapter 4. In particular, the contribution of the DEM absolute vertical accuracy to the geolocation accuracy is given by equation 2.31.

$$loc_{err} = \frac{h_{err}}{tan(\alpha_{inc})} \tag{2.31}$$

where h_{err} is the DEM absolute vertical accuracy, loc_{err} represents the range geolocation accuracy and α_{inc} is the incidence angle. It is important to observe that the contribution given by the DEM absolute vertical accuracy to the geolocation accuracy can be reduced or amplified depending on the incidence angle.

Several quality parameters exist to characterize the DEM quality, which are listed hereinafter, ((NIMA), 2000), (National Geospatial-Intelligence Agency, 2009):

- Absolute Horizontal Accuracy: accuracy of the horizontal location of the DEM points caused by random and uncorrected systematic errors, expressed as the maximum absolute difference between the true and measured values with a 90% confidence level;
- Relative Horizontal Accuracy: accuracy of the horizontal location of the DEM points caused by random errors, expressed as the maximum absolute value of the unbiased difference between the true and measured values with a 90% confidence level. The unbiased difference can be evaluated by subtracting to the difference a local average of the differences;

- Absolute Vertical Accuracy: accuracy of the height of the DEM points caused by random and uncorrected systematic errors, expressed as the maximum absolute difference between the true and measured values with a 90% confidence level.
- Relative Vertical Accuracy: accuracy of the height of the DEM points caused by random errors, expressed as the maximum absolute value of the unbiased difference between the true and measured values with a 90% confidence level. The unbiased difference can be evaluated by subtracting to the difference a local average of the differences.
- Posting: grid spacing.

Several DEM products classification standards exist, among them, the National Geospatial-Intelligence Agency (NGA) standards are commonly used, ((NIMA), 2000), (National Geospatial-Intelligence Agency, 2009):

- Digital Terrain Elevation Data (DTED) standards, level 0, 1, 2;
- High Resolution Terrain Information (HRTI) standards;
- High Resolution Elevation (HRE) standards, composed of the standard HRE Geographic Projection (HRE-GP), with data in geographical projection, and of the standards HRE80-HRE01, with data in UTM projection.

In Tab. 2.1 and in Tab. 2.2 DTED/HRTI standards and HRE standards are summarized.

Specification	**Spatial Resolution**	**Vertical Accuracy (LE90)**		**Absolute Horizontal Accuracy (CE90)**
		Absolute	Relative	
DTED-1	90 m x 90 m	< 30 m	≤ 20 m	≤ 50 m
DTED-2	30 m x 30 m (1 arcsec at the equator)	< 18 m	≤ 12 m ≤ 15 m (terrain slopes >20%)	≤ 23 m
HRTI-3 (or DTED-3)	12 m x 12 m (0.4 arcsec at the equator)	≤ 10 m	≤ 2 m ≤ 4 m (terrain slopes >20%)	≤ 10 m
HRTI-4 (or DTED-4)	6 m x 6 m (0.2 arcsec at the equator)	< 5 m	≤ 0.8 m ≤ 1 m (terrain slopes >20%)	≤ 10 m

Tab. 2.1 – NGA (NIMA) standards for Digital Elevation Models, ((NIMA), 2000).

Product Name	Grid spatial resolution	Random Vertical Error per point (meters)	Relative Vertical Accuracy between points (meters)	Absolute Vertical Accuracy LE90 (meters)
HRE-GP	0.4 arcsec	2.2	6.2	12.4
HRE-80	8 m	1.41	4.00	8.00
HRE-40	4 m	0.71	2.00	4.00
HRE-20	2 m	0.35	1.00	2.00
HRE-10	1 m	0.18	0.50	1.00
HRE-05	0.50 m	0.09	0.25	0.50
HRE-02	0.25 m	0.04	0.12	0.25
HRE-01	0.125 m	0.02	0.06	0.12

Tab. 2.2 – NGA standards for HRE DEM products, (National Geospatial-Intelligence Agency, 2009).

CHAPTER 3
INNOVATIVE TECHNIQUES FOR IMPROVING DEM ACCURACY

This Chapter focuses on complementary and innovative techniques respect to the interferometric processing to generate Digital Elevation Models (DEM) from COSMO-SkyMed (CSK) data. The state-of-the-art interferometric processing was deeply analyzed in Chapter 2. The mentioned innovative techniques can be applied in place of specific InSAR processing steps in order to increase the DEM accuracy or can concern the combination of complementary techniques to mitigate mutual disadvantages and improve the overall performances.

3.1. Multi-Chromatic Approach to SAR Interferometry

The Multi-Chromatic Approach (MCA) to SAR interferometry, (Veneziani, et al., 2006), is a differential analysis in the frequency domain which allows the computation of the absolute phase of the targets without the need to unwrap the phase.

Through MCA it is possible to generate a DEM from interferometric pairs relying on an alternative technique to phase unwrapping algorithms in the spatial domain, and avoiding all the error contributions and the limitations related with this core processing step (e.g. in order to assign to each pixel of a fringe in the wrapped interferogram the right value of integer 2π-multiples, it is necessary a correct segmentation of the fringe pattern).

In particular, in (Veneziani, et al., 2000) and in (Veneziani, et al., 2006) it is shown how, by exploiting a focusing into several range sub-bands, a set of equal resolution interferograms of the same area at adjacent carrier frequencies f_i can be combined in order to improve the edge detection among fringes and to enlarge the extension of segmented areas, also where different kind of phase ambiguities exist. From the set of interferograms, through a differential analysis of sampled interferometric phase history along the frequency axis, it is possible to obtain a point-wise estimator of the terrain height.

In order to reduce the error of the point-wise estimates, by improving the constraints in the linear regression, a combination strategy was introduced between the differential analysis in the frequency domain and a statistical investigation in the spatial domain, which refers to the distribution of the integer 2π-multiples of targets absolute phases, derived by the ratio between the zero order coefficient of the linear fit and 2π, rounded to the nearest integer. These numbers are referred to as k-values. A preliminary segmentation of a fringe pattern is required in order to perform a correct classification of the same pattern in terms of k-values.

The difference between the common phase unwrapping algorithms and the MCA technique is that while the first approach is monochromatic and needs a spatial integration of phase gradients through phase unwrapping techniques which introduce significant contributions to the error budget, the second one is multi-chromatic and allows to perform absolute and spatially independent measurements of targets heights, without the need of phase unwrapping. The MCA technique is reliable when a set of coherent targets is selected, whose interferometric phase history is known in the frequency domain.

A preliminary quality parameter of the measurements achieved through MCA technique, (Veneziani, et al., 2003), is given by equation 3.1.

$$\sigma'_{\phi} = \sqrt{\frac{1}{N_f}\sum_{i=1}^{N_f}[\Phi_i(x,r) - C_0(x,r) - C_1(x,r)\cdot f_i]^2} \tag{3.1}$$

which represents an a-posteriori estimation of the inherent phase standard deviation. In fact, the second term of the equation 3.1 is the mean squared deviation between the interferometric phase samples Φ_i measured at different carrier frequencies f_i and the corresponding values computed through their linear regression. The smaller σ'_{ϕ}, the better is the achievable accuracy for terrain heights.

The first step of the MCA technique consists in the selection from the scene of a set of pixels (i.e. targets) with an inter-band phase standard deviation σ'_{ϕ} below a certain reliability threshold. In (Veneziani, et al., 2003) a threshold of 0.02 *rad* was computed as the value granting height measurements within a height of ambiguity.

Therefore, the scene is divided into patches, and the distribution of the *k*-values can be extracted independently for each fringe segment in the patch. The value of maximum occurrence in this distribution allows to identify the right *k*-value of the fringe analyzed.

These distributions normally have a low percentage of targets matching the right integer term of the absolute phase related to the local morphology. It can also happen that targets have very low phase standard deviation but at the same time an wrong topographic *k*-value. These considerations mean that there is not a strict correlation between the accuracy of the measurements and the target capability to point at the right morphological *k*-value of its local fringe.

However, considering that all the targets which lie on the same fringe should aim at the same *k*-value, also those whose standard deviation is higher than the threshold, the topographic retrieval can be extended to all the fringe targets.

Therefore, after a coarse linear fitting over the basic phase samples of each interferogram, a second order linear regression can be computed for all the pixels of the same fringe, including the absolute phase term at zero frequency, which is related to the fringe *k*-value through the zero order coefficient of the linear fit.

The MCA process and its interaction with the standard InSAR processing steps is reported in Fig. 3.1, (Bovenga, et al., 2011).

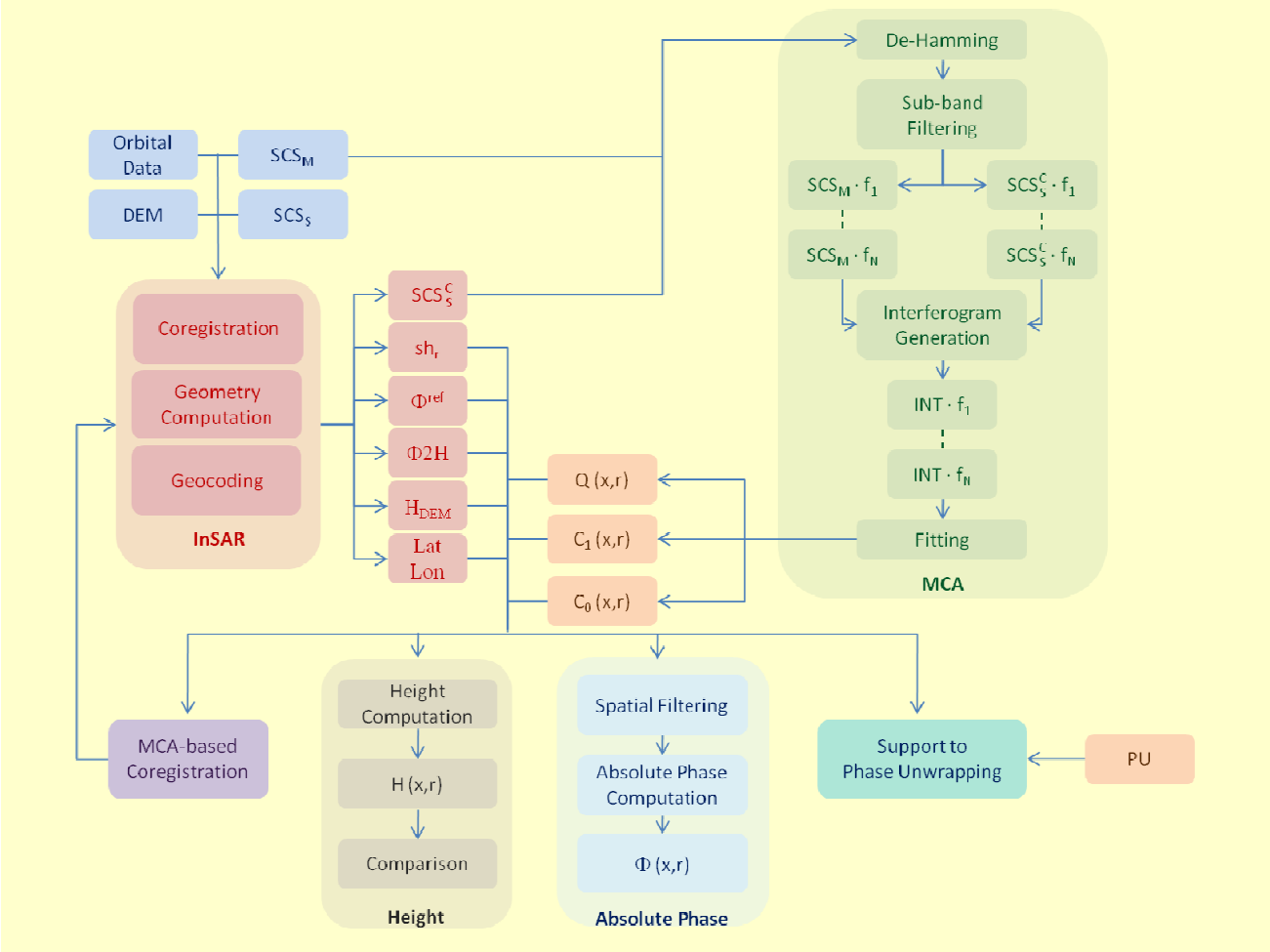

Fig. 3.1 – Multi-Chromatic Approach (MCA) to InSAR diagram.

As summarized in Fig. 3.1, MCA technique takes in input SAR interferometric pairs processed at range sub-bands. The phase of spectrally-coherent pixels has a linear trend respect to the central wavelength of the sub-band, since the slope is proportional to the absolute optical path difference.

The range sub-look images, which are called "chromatic views", have to be generated both from master and slave interferometric image with the same parameters setting $\{I_{M,i}, I_{S,i}\}$ with $i = 1, \ldots, N_f$. After that, it is possible to generate N_f interferograms by cross-multiplying master and slave chromatic views relative to the same central frequency f_i. Considering that only wrapped phase values are measured, it is possible to write equation 3.2.

$$\Phi_i^W(x,r) = -2\pi \cdot k(x,r) - \frac{4\pi}{c} \cdot \Delta R(x,r) \cdot f_i = C_0(x,r) + C_1(x,r) \cdot f_i \quad (3.2)$$

Where:

- $\Delta R = R_M(x,r) - R_S(x,r)$, with R which is the optical path between the sensor and the target on the ground;
- (x,r) are the pixel coordinates in azimuth and range respectively;
- $k(x,r)$ is the integer number of wavelength between the sensor and the target.

As previously stated, and according with equation 3.2, the wrapped interferometric phase has a linear trend with the central carrier frequency, since the linear term $C_1(x,r)$ is proportional to the absolute optical phase difference ΔR, equation 3.3.

$$\Delta R(x,r) = -\frac{c}{4\pi} C_1(x,r) \quad (3.3)$$

The coefficient $C_0(x,r)$ is proportional to the integer number of 2π, i.e. $k(x,r)$, to be added to the wrapped interferometric phase of each pixel to obtain the absolute unwrapped phase in the pixel (x,r).

The consideration at the origin of MCA technique is that phase unwrapping can be performed on a pixel basis, without the need to estimate spatial phase gradients, which may introduce significant errors in conventional phase unwrapping algorithms, at the cost of a worse range resolution related to the sub-bands B_P.

According with this approach, taking in input the generated set of wrapped interferograms, the coefficients $C_0(x,r)$ and $C_1(x,r)$ are point-wise estimated through a linear regression. The phase of a pixel can be wrapped along the frequencies, analogously to what happens in the spatial domain, therefore before the linear regression it is necessary to perform a one-dimensional phase unwrapping. In addition, among MCA parameters, the frequency spacing df has to be set narrow enough to avoid aliasing condition for any elevation in the observed scene.

According with equation 3.3, the absolute path can be derived from the coefficient $C_1(x,r)$ by multiplying it with a large scale factor $c/4\pi$. Therefore, the method is highly sensitive to noise and interferometric coherence, such as in classical interferometry.

This consideration suggests to use MCA on highly coherent pixels in order to achieve very high accuracy local absolute measurements which can be integrated and improve the performances of classical phase unwrapping algorithms and also of coregistration techniques. In general, MCA technique looks at frequency-stable targets and it is able to provide absolute phase unwrapping on

highly coherent points to support standard phase unwrapping as well as coregistration algorithms and to perform topographic measurement.

If in input to the MCA technique are provided SAR raw data, the chromatic views are generated immediately after the focusing process, performing range sub-looks in the range frequency space before the last Fourier transform bringing the signal back to the image domain. If SAR raw data are not available for data policy constraints, the input to MCA technique has to be represented by SAR images processed up to SCS (i.e. Single-look Complex Slant-range) level. The SCS processors are linear and phase preserving, with the exception of the Hamming filter at the end of the focusing process, necessary to reduce side-lobe ratio of the point scatterers response, to the detriment of a small loss in resolution. Therefore, in order to avoid asymmetry in the spectrum, the application of a de-Hamming filter in range, consisting in an inverse apodization filter, is required before splitting into sub-bands, Fig. 3.1.

Moreover, referring to Fig. 3.1, in order to save processing time, the coregistration between master and slave SAR images is performed only on the full-band images, before the sub-looks generation. However, performing the sub-band filtering after the re-sampling step, which is part of the coregistration, causes the loss of a phase term related to the range shift applied to the slave image. This term has to be considered in order to obtain the correct path difference between the two images, and it can be inferred from the range shift matrix, which is usually available as a side-product of the coregistration step. The needed phase compensation is computationally inexpensive respect to the coregistration process applied to every sub-look. Furthermore, by following this approach also processing constraints are relaxed: since ΔR is decreased by a factor proportional to the coregistration shift, the minimum value of df needed to avoid aliasing along the frequency domain is increased of the same amount.

With the aim of giving an quantitative idea of the benefit of the MCA technique, an error analysis of phase unwrapping algorithms is presented, which would be avoided with the proposed technique. It is worth noting that phase unwrapping errors influence directly the accuracy on DEM generated through InSAR processing. Three main error sources are related to phase unwrapping, such as:

- phase confusion caused by sharp change of terrain: in terrain regions with sharp changes, the fringes assume acute irregularities in the interferogram, making true phase restoring difficult for phase unwrapping under fixed Nyquist sampling frequency;
- phase distortion caused by poor SNR, yielding distortions also in the unwrapped phase;
- improper selection of phase unwrapping algorithms (in terms of norm and weight) respect to the interferogram, which can cause residual errors affecting the overall accuracy.

3.2. Delta-k Technique

Delta-k technique allows the estimation of the absolute unwrapped phase also for scenes where the topography changes rapidly or with phase noise or difficult geometries to be unwrapped. Where classical phase unwrapping algorithms do not perform correctly leaving gaps and errors in the generated DEM, the delta-k technique allows to artificially increase the height of ambiguity up to a value such that phase unwrapping is not necessary anymore, by exploiting the frequency diversity in range to simulate an interferogram with a longer carrier wavelength than that of the SAR system. Through this approach, phase unwrapping is not necessary anymore because absolute phase is directly given over small patches of the image. Delta-k technique was initially thought as a technique able to determine the remaining phase ambiguity in an interferogram after phase unwrapping, (Brcic, et al., 2008).

In repeat-pass interferometry, the interferometric phase φ and the differential range Δr are related as in equation 3.4.

$$\varphi = 4\pi \frac{f_c}{c} \Delta r \tag{3.4}$$

where f_c is the radar carrier frequency and c is the speed of light.

Therefore, the differential phase $\Delta\varphi$ between two sub-band interferograms with range bandwidths b and range center frequencies $f_c + f_0$ and $f_c - f_0$ respectively, Fig. 3.2, is given by equation 3.5 and is defined as delta-k phase.

$$\Delta\varphi = \varphi_2 - \varphi_1 = 4\pi \frac{2f_0}{c} \Delta r \tag{3.5}$$

Basing on equations 3.4 and 3.5, the delta-k phase can be considered as the interferometric phase at a carrier frequency of $2f_0 \ll f_c$, or equivalently at a much longer wavelength than the carrier. Therefore, the height of ambiguity of the delta-k phase is increased by the delta-k factor $f_c/2f_0$ relative to the full-band interferometric phase. The delta-k factor can be at least equal to f_c/B, resulting in very high heights of ambiguity, making phase unwrapping unnecessary. The integer phase cycle number at the carrier frequency can then be obtained by scaling the delta-k phase by the same factor.

According to the above explained principle, the delta-k absolute phase can be estimated following the flow-chart in Fig. 3.3.

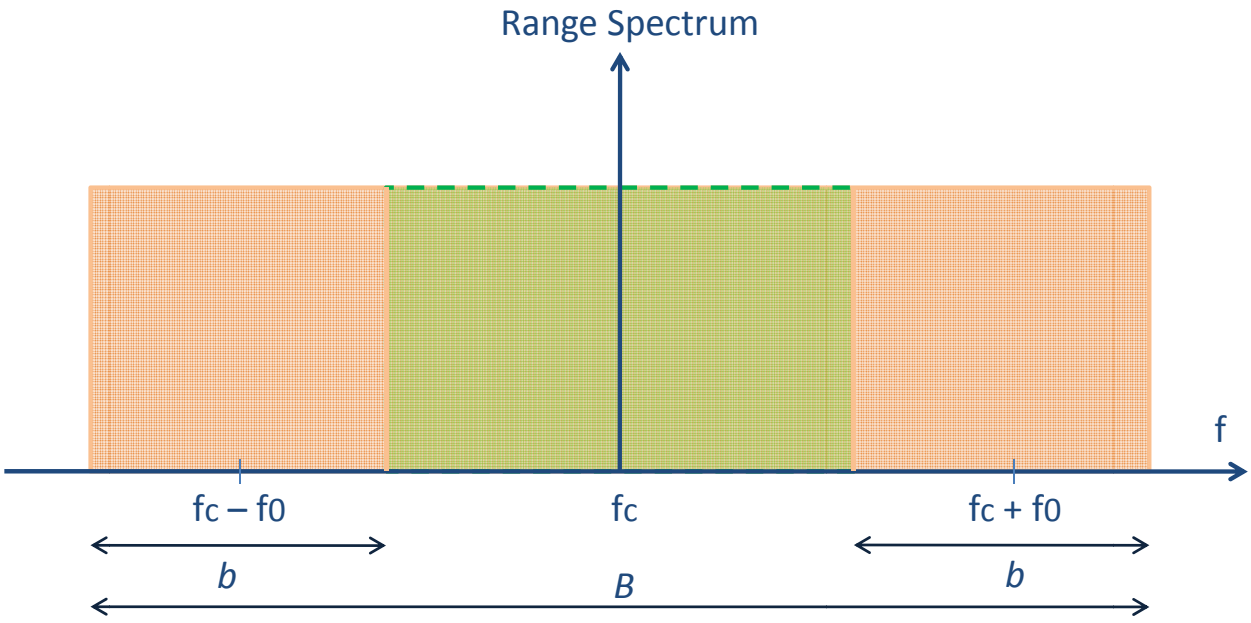

Fig. 3.2 – Filtering of the full-band to sub-bands.

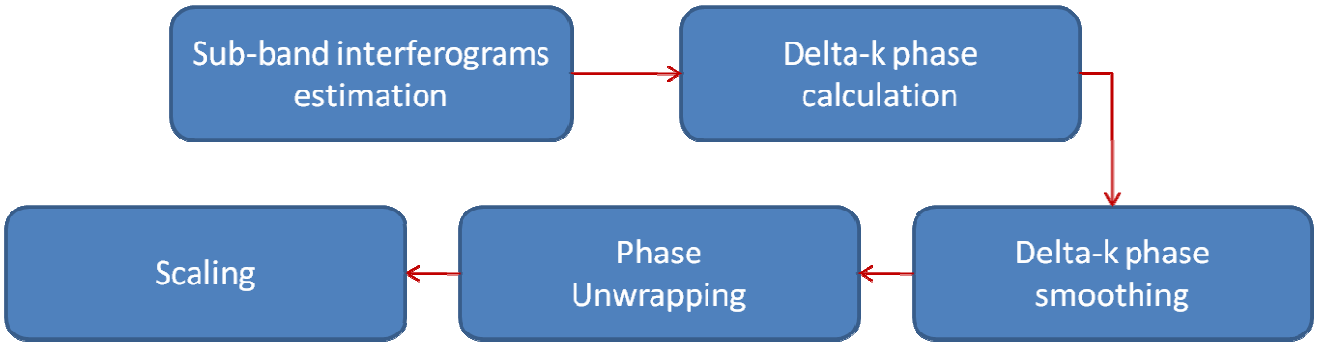

Fig. 3.3 – Delta-k absolute phase estimation algorithm.

Referring to Fig. 3.3, the first step of the delta-k absolute phase estimation algorithm consists in the estimation of the sub-band interferograms. A band-pass filter is applied to the full-band of both master and slave SAR images, in order to generate a master and a slave image for each sub-band, which in turn are processed to generate independent lower and upper sub-band interferograms. A demodulation is performed immediately after band-pass filtering so that the lower and upper sub-band SAR images are centered at the frequencies $f_c - f_0$ and $f_c + f_0$, in order to avoid an incorrect flat earth phase and coregistration errors due to the re-sampling of band-pass signals, issues which would arise if images with range spectra not centered at the carrier frequency were processed.

The second step of the algorithm is the calculation of the delta-k phase, applying equation 3.5 to estimate the difference between the interferometric phases of the upper and lower sub-band.

The third step of the algorithm consists in smoothing the delta-k phase. In particular, assuming the statistical independence between the upper and lower interferometric phases, the variance of the delta-k phase is increased of a factor approximately equal to $2B/b$ respect to the full-band

interferometric phase, increasing the probability of phase wraps. Therefore, it is necessary to apply a low-pass filter to smooth the complex delta-k phase, in order to reduce its variance.

The fourth step of the algorithm is phase unwrapping, since even delta-k phase can cross a 2π interval, depending on the topography, on the delta-k height of ambiguity and on the overall phase offset in the interferogram. However, delta-k phase unwrapping is usually unambiguous and without residuals.

The fifth and last step of the algorithm consists in scaling-up the delta-k phase by the delta-k factor to the height of ambiguity at the carrier frequency.

In (Bamler, et al., 2005), it is shown that for a number N of non-overlapping sub-bands with the same range bandwidth, the optimal sub-band range bandwidth b is given by equation 3.6.

$$b = \frac{B}{N+1} \tag{3.6}$$

with range center frequencies given by equation 3.7.

$$f_c \pm B\frac{N-2(n-1)}{2(N+1)}, n = 1, \dots, \frac{N}{2} \tag{3.7}$$

which allows to achieve a Fisher efficiency η_F, defined as the ratio between the Cramer-Rao lower bound and the variance of the estimator, given by equation 3.8.

$$\eta_F = \frac{N(N+2)}{(N+1)^2} \tag{3.8}$$

Since the use of multiple sub-bands does not improve significantly the performances, increasing at the same time the implementation complexity, only two sub-bands are usually considered.

3.3. Geolocation Improvements through Atmospheric Modeling

A geolocation improvement of CSK images obtained through a fine atmospheric delay model would allow to achieve a strong improvement of DEM accuracies achievable through interferometric processing.

The delay introduced by the atmosphere on the two-way X-band signal is significant, and strongly affects the SAR image geolocation performance if not taken into account. Some improvements are possible thanks to nowadays' high resolution SAR systems and to Galileo studies aimed at achieving 1 mm delay path accuracy, (Solheim, et al., 1999).

Atmosphere can be viewed as a stack of layers, each one locally homogeneous in terms of density and optical/microwave refractivity.

According to an exponential density assumption, given a target point on the Earth surface, the up-standing layer boundaries can be recursively defined as in equation 3.9, (Jehle, et al., 2008).

$$h_{i+1} = -h_s \ln\left(e^{\frac{h_i}{h_s}} - \frac{dt_{tot}}{N}\right)$$
$$dt_{tot} = \int_{h_0}^{h_n} e^{-\frac{h_i}{h_s}} dh \tag{3.9}$$

Basing on equation 3.9, in (Jehle, et al., 2008) and in (Schubert, et al., 2010) an upgraded model of the atmospheric path delay Ψ was computed, whose components are respectively the troposphere and the ionosphere terms, equation 3.10.

$$\Psi = \Psi_{iono} + \Psi_{tropo}$$
$$\Psi_{iono} = k_4 \frac{TEC}{f_c^2} \qquad \Psi_{tropo} = \Psi_{wet} + \Psi_{hyd} + \Psi_{liq}$$
$$\Psi_{wet} = 10^{-6}\left[\frac{(k_2' T_m + k_3) R_d e_0}{T_0[g_m(\lambda+1) - \beta R_d]}\right]\kappa_{wet} \qquad \kappa_{wet} = \left(1 - \frac{\beta h}{T_0}\right)^{\frac{g_m(\lambda+1)}{\beta R_d}-1} \tag{3.10}$$
$$\Psi_{hyd} = 10^{-6} k_1 \frac{R_d}{g_m} P_0 \qquad \Psi_{liq}\ negligible$$

where T_0 is the local atmosphere temperature in °K, T_m is the mean water vapor temperature in °K, h is the target height in meters, λ is the average water vapor decrease, e_0 is the water vapor pressure over the sea level in *hPa*, g_m is the local gravity acceleration. Further symbols as well as the refractive constants, the ideal gas constant and the atmosphere temperature gradient are discussed in (Jehle, et al., 2008).

According to equation 3.10, the path delay depends on four variables, such as latitude and altitude, which affects respectively g_m and (h, g_m), together with local air-column temperature and pressure. According to a static atmosphere model, atmosphere temperature and pressure are assumed to be constant and equal to their respective average values on a year basis, therefore the relations in equations 3.10 can be computed directly in 2-ways time delays and applied to radiation incidence boundaries. In such a way, the only remaining variable is the target (or column) height. If equation 3.10 are adapted to CSK case, equation 3.11 can be obtained, which show a parabolic behavior of the atmospheric path delay Φ, expressed in *ns*, with the target height h, where *a*, *b* and *c* are proper positive constants which depend on the nominal incidence angle, calculated using the local height above the ellipsoid, (Jehle, et al., 2008).

$$\Phi = a - b \cdot h + c \cdot h^2 \tag{3.11}$$

CSK standard processors for the generation of Geocoded Terrain Corrected (GTC) products can be further improved by implementing a dependence of the atmospheric path delay from the target height. The processing level suitable for such an implementation is figured in GTC products because a DEM is already used for the geocoding process and can be also used to take into account the target height in large areas where strong topographic changes occur.

3.4. Wavelet Fusion

The DEM accuracy mainly depend, as further analyzed in Chapter 4, on:

- phase unwrapping errors;
- baseline errors (or orbit indetermination), if applicable;
- phase noise, including thermal noise, coregistration errors, processing artifacts, temporal decorrelation, etc;
- atmospheric effects, due to the refractive index variations in the propagation medium, both in space and in time.

Even if two interferometric images show high coherence values, the generated DEM can be affected by strong distortions due to the atmospheric effect, since the correlation length of atmospheric phenomena (usually more than 1 km) is much larger than the estimation window used the coherence computation.

Both phase noise and atmospheric artifacts can be mitigated in the final DEM if large baseline interferograms are used, since the height dispersion is related to the phase dispersion by the inverse of the normal baseline.

A properly weighted combination of several uncorrelated DEMs strongly decreases the effect of phase artifacts on the final DEM. According to (Ferretti, et al., 1999), through a wavelet domain approach it is possible to take advantage of the specific frequency trend of the atmospheric distortions, and to estimate from the data the noise and the atmospheric distortion power associated to each interferogram. Therefore, by combining DEMs through a weighted average performed in the wavelet domain, it is possible to improve the accuracy of the final DEM since the phase error is estimated for each interferogram.

In Chapter 4, an experimental analysis is performed on a test site to quantitatively understand the achievable improvement in DEM quality after a wavelet-based fusion between a high accuracy DEM generated from CSK interferometric pairs, and a low accuracy DEM deriving from SRTM mission, where the atmospheric disturbances at low frequencies are mitigated.

In this paragraph, the theory applied for a wavelet-based DEM combination is explained, referring to (Ferretti, et al., 1999) for the atmospheric term characterization and further details.

Taking in input for the combination several DEMs, derived from several unwrapped interferograms, each one, if there were not atmospheric artifacts in any of the input data, would be considered as affected by a Gaussian noise. Then, the combined DEM would be derived through a maximum-likelihood Gaussian estimator, equation 3.12.

$$\hat{z} = \frac{\sum_{i=1}^{N} \frac{z_i}{\sigma_{zi}^2}}{\sum_{i=1}^{N} \frac{1}{\sigma_{zi}^2}} \tag{3.12}$$

where z_i is the elevation estimated from the i^{th} interferogram and σ_{zi}^2 is the relative noise variance.

However, the previous approach has several approximations, mainly because actually each DEM sample is correlated with neighbor samples, there are atmospheric in-homogeneities which are neglected in noise variances, and the noise spectrum is not white.

Since the atmosphere is not a homogenous medium, the interferometric phase value include both a white noise term, w, and an additive term due to the time and space variations of atmospheric water vapor, a, which exhibits a $1/f$-type spectral behavior, (Wornell, 1993). These terms are statistically independent since associated to different physical phenomena.

The previous two terms have very different spectra, since the noise term w dominates at high frequencies while the atmospheric contribution a dominates at low frequencies.

From these consideration, the problem statement is to find a way to isolate the error power due to the atmosphere from the noise power due to decorrelation, taking in input several interferograms on the same area. A useful technique to this aim is the wavelet transform.

Turbulence phenomena and in general $1/f$ processes, such as the atmospheric term a, are scale-invariant and have statistical self-similarity, (Wornell, 1993), meaning that their statistics are invariant to the scaling of time or space axis, equation 3.13.

$$S_a(f) \propto S_a(kf) \tag{3.13}$$

The wavelet transform plays a central role in the analysis of scale-invariant signals. The Discrete Wavelet Transform (DWT) can be implemented as a filter bank and allows to estimate the noise and atmospheric distortion mean powers.

According to (Ferretti, et al., 1999), if N independent DEMs are available, it is possible to generate $N_E = \binom{N}{2}$ error maps computing the difference between each pair. The error mean power is given by four independent contributions, equation 3.14.

$$P_{ij} = \sigma_{ai}^2 + \sigma_{aj}^2 + \sigma_{wi}^2 + \sigma_{wj}^2 \tag{3.14}$$

where w and a represent respectively the noise and atmospheric contributions and i and j the DEMs used for the error map generation.

If the noise power σ_{wi}^2 was exactly known for each DEM, and $N > 2$, it would be easy to obtain the unknown atmospheric distortion powers. However, usually the interferograms are filtered before being unwrapped, so the noise power estimated from the coherence cannot be taken as the truth. Furthermore, possible phase unwrapping errors can corrupt the error power. For these reasons it is necessary to estimate both atmospheric distortion power and noise power from the error maps, while the coherence maps are used to understand the spatial distribution of the noise power.

Supposing, only for a first approach to the problem, a constant coherence value in each interferogram, and considering the one-dimensional case for simplicity, it is assumed that $a(t)$ is a zero-mean Gaussian $1/f$ process, with the spectrum in equation 3.15.

$$S_a(f) \propto f^{-\frac{8}{3}} \tag{3.15}$$

Given the equation 3.16,

$$r(t) = a(t) + w(t) \tag{3.16}$$

where $w(t)$ is a zero-mean Gaussian white noise, it is possible to extract a collection of wavelet coefficients, equation 3.17.

$$\boldsymbol{r} = \{r_n^m, m \in \mathcal{M}, n \in \mathcal{N}(m)\} \tag{3.17}$$

where m and n are the scaling and translation indexes, $\mathcal{M}\{1, \dots, M\}$ is the set of available scales (sub-bands), limited by the total number of available data samples and the filter length, and $\mathcal{N}(m)$ is the set of available samples in each sub-band.

These variables are uncorrelated and can be modeled as mutually independent zero-mean Gaussian random variables, equation 3.18.

$$var\ r_n^m = \sigma_m^2 = \sigma_a^2 \cdot 2^{-\frac{8}{3}m} + \sigma_w^2 \tag{3.18}$$

Therefore, the maximum-likelihood solution has to be found through an iterative algorithm from equation 3.19.

$$\widehat{P_{ij}^m} = \left(\sigma_{ai}^2 + \sigma_{aj}^2\right) \cdot 2^{-\frac{8}{3}m} + \left(\sigma_{wi}^2 + \sigma_{wj}^2\right) \tag{3.19}$$

where:

$$\widehat{P_{ij}^{m}} = \frac{1}{\mathcal{N}(m)} \sum_{n \in \mathcal{N}(m)} (r_n^m)^2 \tag{3.20}$$

where $m \in \mathcal{M}$ and $\mathcal{N}(m)$ is the number of samples at scale m. If the number of interferograms $N > 2, N_E > N$, there are a sufficient number of equations to solve for $\{\widehat{\sigma_{ai}^2}, \widehat{\sigma_{wi}^2}\}, i = 1, \dots, N$.
Since the previous considerations were based on the first approximation assumption of a coherence value constant over the image, and since through the explained process it was possible to obtain an estimation of just the mean power $\widehat{\sigma_{wi}^2}$, it is possible to simply scale the estimated noise powers σ_{win}^2, which are function of the point n in the image, by a factor K_i which is function of the effective number of looks in the data, equation 3.21.

$$\frac{1}{p} \sum_{n=1}^{p} K_i \, \sigma_{win}^2 = \widehat{\sigma_{wi}^2} \tag{3.21}$$

where p is the number of points in the region of interest.

The previously explained process allows to estimate the noise power and the atmospheric distortion power for each DEM, $\{\widehat{\sigma_{ai}^2}, \widehat{\sigma_{wi}^2}\}, i = 1, \dots, N$.
After that, the combined DEM can be obtained through a proper weighted average, again in the wavelet domain. The wavelet coefficients $(d_n^m)_i$ relative to the i^{th} DEM include three contributions such as topography t_n^m, atmospheric distortion (a_n^m) and noise (w_n^m), as in equation 3.22.

$$(d_n^m)_i = t_n^m + (a_n^m)_i + (w_n^m)_i \tag{3.22}$$

From equation 3.18 it is possible to compute the variances of the Gaussian variables a_n^m and w_n^m, while the topographic contribution can be obtained through a maximum likelihood Gaussian estimator, equation 3.23.

$$\widehat{t_n^m} = \frac{\sum_{i=1}^{N} \frac{(d_n^m)_i}{\sigma_{min}^2}}{\sum_{i=1}^{N} \frac{1}{\sigma_{min}^2}} \tag{3.23}$$

$$\sigma_{min}^2 = \widehat{\sigma_{ai}^2} \cdot 2^{-\alpha m} + \widehat{\sigma_{win}^2}$$

Also the topography can be modeled as a $1/f$ process, the coefficients t_n^m are uncorrelated and it is possible to work independently on each sample.

Through the explained technique, it is possible to understand how by combining in the wavelet domain many uncorrelated phase artifacts, mainly due to atmospheric variations, their effect on DEM accuracy is in general very reduced.

3.5. Permanent Scatterers Interferometry and SqueeSAR

Since classical SAR interferometric processing is affected and limited by constraints such as atmospheric effects, thermal and other sources noise, a recent technique which was developed and explained in literature to overcame these limitations, namely Permanent Scatterers Interferometry (PS-InSAR), (Ferretti, et al., 2001).

PS-InSAR is a very effective technique to measure ground displacements or subsidence, or to determine with very high accuracy the height of those pixels which remain coherent over a large sequence of interferograms, i.e. permanent scatterers. If used to generate a DEM, the major drawback of this technique would be the voids filling, especially where the density of the points which exhibit a phase stability over time is poor, such as in non-urban areas. However, the great advantage of this technique is the very high accuracy achievable in measuring the permanent scatterers' height, since by using a large amount of interferograms it is possible to remove errors such as system and thermal noise, atmospheric phase contribution errors, temporal decorrelation effects, input DEM errors, which usually affect the final DEM accuracy.

Examples of permanent scatterers correspond to metallic structures, buildings, antennae, bridges, man-made structures, dams, water-pipelines, prominent natural features such as exposed rocks, and any other elements showing phase stability over a long period of time.

Many integration strategies of this technique with standard interferometric techniques can be thought, according to the specific aim. In particular, the very high accuracy measured 3D coordinates through PS-InSAR can be very useful to refine and to increase the accuracy of an already generated interferometric DEM in correspondence to the permanent scatterers, or to create a 3D model to be superimposed to a DEM in order to increase the specific scene awareness. This kind of integration strategies is the reason to deepen this technique in this Chapter.

Other general applications of PS-InSAR technique are for instance surface deformation measurements, slope instability, flood protection, oil field monitoring, CO_2 sequestration, seismic faults, surface deformation measurement, urban subsidence, buildings stability and health monitoring.

PS-InSAR has as the major constraint the need of a huge amount of data to give significant results. Higher the number of input images is, better the precision of the measurement. For instance, the theoretical precision of the estimate of the target height is related to the number of input images, to

the dispersion of their normal baselines and to the phase noise according to equation 4.30 of Chapter 4.

PS-InSAR is an effective technique mainly in urban areas, where the density of permanent scatterers is much higher, but faces some limitation in rural areas. This issue has a very serious impact for instance if the technique is used to generate a DEM, since voids are a binding limitation for industrial DEM production, and voids filling methods are not reliable for wide voids.

With the aim of facing and solving this major issue, a new technique called SqueeSAR was recently introduced, (Ferretti, et al., 2011), according to whom in addition to permanent scatterers also distributed scatterers can be taken in input for this new algorithm, expanding the application of the technique also to rural areas with a low density of scatterers. Distributed scatterers consist of a wide area where the backscattered energy in statistically homogeneous within the area. Distributed scatterers typically correspond to debris areas, non-cultivated lands and desert areas. The processing chain required is the same of PS-InSAR, and distributed scatterers, properly handled, are finally managed as permanent scatterers, having as the resulting effect an increasing number and density of useful scatterers.

In the following part of the paragraph, the main processing steps of the two techniques will be analyzed in detail.

3.5.1. PS-InSAR Technique

The accuracies achievable through PS-InSAR in DEM generation and terrain displacement measurement on the permanent scatterers are respectively in the order of sub-meter accuracy and millimetric accuracy, and mainly depend on the number of input images used for the process, (Ferretti, et al., 2001).

The first task of PS-InSAR technique is to identify single pixels which are coherent over long time intervals and for a wide range of look-angles, namely permanent scatterers. When the dimension of the permanent scatterer is smaller than the resolution cell, the coherence is good even if the normal baseline of the interferometric pair is higher than the critical baseline, therefore it is possible to exploit this assumption selecting a spatial dimension of the scatterers such that all the available pairs of the dataset can be used with their baselines. Even if the coherence on neighbor pixel is low, on these targets it is possible to obtain the previously estimated accuracies.

The process is explained consecutively, (Ferretti, et al., 2007): supposing that $(N + 1)$ SAR images are available on the area of interest, these images have to be co-registered to a unique master image, and a DEM of that area has to be generated through classical interferometric processing from low temporal baseline interferometric pairs. Then, N differential interferograms between all available

SAR images have to be computed. After DEM compensation, the residual phase of the interferogram i is given by equation 3.24.

$$\phi_i = \frac{4\pi}{\lambda} r_{Ti} + \alpha_i + \eta_i + \varepsilon_{topo\_i} \tag{3.24}$$

where:

- λ is the system wavelength;
- α_i is the atmospheric phase contribution;
- η_i is the decorrelation noise;
- ε_{topo_i} represents the phase contribution due to possible errors in the input DEM, which is proportional to the normal baseline of each image, B_{n_i};
- r_{Ti} is the possible target motion in the direction of the satellite line-of-sight.

The first term at the second member of equation 3.24 can be written as in equation 3.25.

$$\frac{4\pi}{\lambda} r_{Ti} = \frac{4\pi}{\lambda} v_r T_i + \mu_{NLi} = C_{vi} v + \mu_{NLi} \tag{3.25}$$

where:

- v is the unknown component of the mean target velocity in the direction of the line of sight;
- μ_{NLi} is the phase term due to a possible non-linear target motion;
- T_i is the temporal baseline between master acquisition and the generic i^{th} slave acquisition.

Therefore, since there are N independent differential interferograms, it is possible to write for each pixel a linear system of N equations and two unknowns, equation 3.26.

$$\phi_i = C_{zi} \varepsilon_z + C_{vi} v, \quad \text{for } i = 1, \dots, N \tag{3.26}$$

where:

- ε_z is the DEM error;
- C_{zi} is proportional to B_{n_i}.

Actually, since the phase values are not unwrapped, the problem is not linear. However, using a simple periodogram, if the SNR is high enough it is possible to estimate both the residual elevation and the mean line-of-sight velocity.

The Linear Phase Residues (LPR) w_i, representing the phase data after linear detrending in temporal and spatial baseline, are the sum of three contributions, such as Atmospheric Phase Screen (APS) of the master and slave images, noise, and non-linear motion, equation 3.27.

$$w_i = \phi_i - C_{zi} \varepsilon_z - C_{vi} v_r = \mu_{NLi} + \alpha_i + n_i \tag{3.27}$$

Since μ_{NLi}, α and n are independent random variables, also the residual phase variance σ_w^2 is the sum of the three variances: $\sigma_{\mu_{NL}}^2, \sigma_\alpha^2$ and σ_n^2.

An accurate estimation of the target elevation and motion can be performed only if σ_w^2 is low.

For this reason, as a first step a subset of image pixels is selected, retaining only highly coherent targets, with low σ_w^2.

Among them, considering a pair of targets within a short distance, it is possible to estimate the relative mean velocity Δv and the relative elevation error $\Delta\varepsilon_z$ with a good accuracy, since a short distance yields a low variance of the atmospheric component σ_α^2.

Moreover, if the hypothesis of correlated adjacent pixels is verified, also $\sigma_{\mu_{NL}}^2$ is low.

Therefore, it is possible to obtain an estimation of v and ε_z by integrating the values of Δv and $\Delta\varepsilon_z$ previously estimated from pairs of adjacent pixels.

Following this process, if $|w_i| < \pi$, it is possible to unwrap the differential interferograms, obtaining the unwrapped phase differences $\Delta\varphi_i$ between pairs of adjacent pixels and then integrating them over the sparse grid of permanent scatterers candidates.

To summarize, even if PS-InSAR works easier if a constant velocity model can be applied, even if non-uniform target motion is present the technique is able to model it and to provide results, at the condition that the permanent scatterers density and coherence is high enough, i.e. low σ_w^2. Phase differences are unwrapped using the estimated values of relative velocity Δv and relative elevation $\Delta\varepsilon_z$ of each pair of scatterers, and phase values are then integrated over the grid of permanent scatterers using a technique used for unwrapping regularly sampled data.

Once phase data are unwrapped, it is possible to obtain estimates at unmeasured points and instants (e.g. subsidence), through interpolation or prediction for instance.

3.5.2. SqueeSAR Technique

While PS-InSAR works only with permanent scatterers, which usually correspond to point-wise, man-made objects that are very densely distributed in urban areas and very sparsely present in non-urban areas, SqueeSAR technique aims at extracting geophysical parameters not only from permanent scatterers, but also from distributed scatterers, in order to overcome previously analyzed limitations of PS-InSAR. Through SqueeSAR technique, permanent and distributed scatterers can be jointly processed, taking into account their different statistical behavior and without the need to unwrap hundreds of interferograms. To this aim, the coherence matrix associated with each distributed scatterer is properly squeezed to provide a vector of optimum wrapped phase values, which allow to manage it as a permanent scatterer. Compared to permanent scatterers case, the

signals retrieved for distributed scatterers, i.e. for natural targets where no dominant scatterer can be identified within a specific resolution cell, are noisier and with a lower spatial density, which in any case depends on the selected coherence threshold.

A distributed scatterer is different from a point-wise permanent scatterer, since it often corresponds to neighboring pixels belonging to areas of moderate coherence in some interferometric pairs of the available dataset, which have similar reflectivity values.

Although the average coherence in time of these targets is typically low because of temporal and geometrical decorrelation, the number of pixels which exhibit a similar statistical behavior can be high enough to make possible for some pixels to exceed the coherence threshold and become a permanent scatterer.

While combining permanent scatterers with distributed scatterers in order to increase the density of measurement points, it is important to preserve the higher quality information obtained through PS-InSAR over deterministic targets, by using space-adaptive spatial filters able to average only statistically-homogeneous-pixels, without averaging permanent scatterers with low-SNR neighboring pixels.

The process is explained consecutively, (Ferretti, et al., 2011).

First of all a space-adaptive filtering is performed, with an algorithm able to discriminate if two image pixels belonging to an interferometric data-stack can be considered statistically-homogeneous or not. Once the proper estimation window is defined for each image pixel and the families of statistical-homogeneous-pixels are created, amplitude data can be de-speckled, interferometric phase values can be filtered and coherence values can be estimated.

In particular, given N SAR images re-sampled on the same master grid, $\boldsymbol{d}$ is a complex data vector, deterministic for point scatterers and random for distributed scatterers, defined in equation 3.28.

$$\boldsymbol{d}(P) = [d_1(P), d_2(P), \dots, d_N(P)]^T \tag{3.28}$$

where $d_i(P)$ is the complex reflectivity value of the image i^{th} in the pixel P, and ^{T} indicates transposition.

Two pixels P_1 and P_2 are defined statistically homogeneous if the null hypothesis that the two vectors $\boldsymbol{d}(P_1)$ and $\boldsymbol{d}(P_2)$ have the same probability distribution function cannot be disproved, given a certain level of significance. It means that the probability distribution function of the complex reflectivity values of the two pixel is the same for all the images of the dataset. These statistical tests are applied to all pixels within a certain estimation window. An easy to implement option to this aim is the two-sample Kolmogorov-Smirnov test, (Stephens, 1970), which can be applied to

vectors of amplitude values of reflectivity rather than to complex values, according to the approach followed for permanent scatterers.

The space-adaptive algorithm developed by TRE, (Ferretti, et al., 2011), able to identify statistically homogeneous areas is composed of the following steps:

- For each image pixel P, an estimation window is defined centered on P;
- A two-sample Kolmogorov-Smirnov test is applied to amplitude vectors to select all the pixels within the estimation window which can be considered statistically-homogeneous with P;
- The selected pixels which are not connected to P directly or through other statistically-homogeneous pixels are discarded;
- Pixel P and all statistical-homogeneous pixels within the estimation window connected to P, namely set Ω, are considered for further processing.

In order to estimate the statistical parameters of each distributed scatterer, under the Gaussian scattering assumption based on the central limit theorem, SAR data vector can be described by a zero-mean, multi-dimensional, complex Gaussian probability distribution function. Therefore, for a complete statistical description of a distributed scatterer it is sufficient to know the covariance matrix. The sample covariance matrix can be estimated through equation 3.29.

$$\boldsymbol{C}(P) = E[\boldsymbol{d}\boldsymbol{d}^H] \approx \frac{1}{|\Omega|}\sum_{P\in\Omega} \boldsymbol{d}(P)\,\boldsymbol{d}(P)^H = \widehat{\boldsymbol{C}} \tag{3.29}$$

where ^{H} stands for Hermitian conjugation and Ω is the set of statistically-homogeneous pixels used in the sample estimate of the covariance matrix.

The principal diagonal of the covariance matrix of any distributed scatterer represents a data vector of N despeckled intensity values of the N available scenes, while the phase values of the off-diagonal complex elements of $\widehat{\boldsymbol{C}}$ are spatially filtered interferograms.

The coherence matrix $\boldsymbol{\Gamma}$ is obtained by normalizing amplitude data such that $E[|d_i|^2] = 1$ for all i, and respect to the covariance matrix it allows to compensate for possible backscattered power unbalances among all the images.

The absolute values of the off-diagonal elements of $\hat{\boldsymbol{\Gamma}}$ represent an estimate of the coherence values for all possible interferograms of the data-stack, γ_{kj}, while the phase values correspond to spatially filtered interferometric phases, ϕ_{kj}, equation 3.30.

$$\hat{\boldsymbol{\Gamma}} = \left\{\gamma_{kj} \cdot e^{i\phi_{kj}}\right\} \tag{3.30}$$

While for a deterministic target such as a permanent scatterer the phase values of all off-diagonal elements of the coherence matrix are redundant, since the $N(N-1)/2$ phase values are simply the

difference in phase values of the N available scenes, equation 3.31, this property of phase triangularity or phase consistency is no longer true for a distributed scatterer.

$$\phi_{nj} = \phi_{nm} - \phi_{mj} \tag{3.31}$$

For distributed scatterers, the coherence matrix is not redundant, it is not rank 1, and equation 3.31 is not valid anymore.

Therefore, for distributed scatterers it is not possible to consider only N interferometric phase values as for permanent scatterers, but it is necessary to deal with $N(N-1)/2$ values.

In order to make joint processing of permanent and distributed scatterers possible, it is necessary for distributed scatterers, through a phase triangulation algorithm (PTA) described consequently, to estimate a vector of N phase values, $\boldsymbol{\vartheta} = [\vartheta_1, \vartheta_2, \dots, \vartheta_N]$, matching those of the off-diagonal elements of $\hat{\boldsymbol{\Gamma}}$, properly taking into account the associated coherence values.

To this optimization aim, the coherence matrix of a generic pixel P is supposed to be expressed as in equation 3.32.

$$\boldsymbol{\Gamma}(P) = \boldsymbol{\Theta}\boldsymbol{\Upsilon}\boldsymbol{\Theta}^{\mathrm{H}} \tag{3.32}$$

where:

- $\boldsymbol{\Upsilon}$ is a Nx N symmetric real matrix whose elements are the coherence values of all the interferograms;
- $\boldsymbol{\Theta}$ is a Nx N diagonal matrix whose elements are the true phase values of pixel P, related to the optical path of the radar beam in each acquisition, $\boldsymbol{\Theta} = \mathrm{diag}\{e^{j\theta}\}$, where assuming that all pixels belonging to Ω are described by the same set of phase values θ, the maximum likelihood estimate of θ is obtained by maximizing the probability distribution function of the statistically-homogeneous pixels.

Setting the interferometric phase of the first image to zero (possible since phase values can be estimated up to an arbitrary additive constant because only phase differences appear in $\hat{\boldsymbol{\Gamma}}$), the optimal estimate of the remaining $N-1$ phase values, $\boldsymbol{\lambda} = [0, \vartheta_2, \dots, \vartheta_N]^{\mathrm{T}}$, is given by equation 3.33.

$$\begin{aligned} \hat{\boldsymbol{\lambda}} &= \arg\max_{\lambda}\{\exp[-\mathrm{trace}(\boldsymbol{\Phi}\boldsymbol{\Upsilon}^{-1}\boldsymbol{\Phi}^{\mathrm{H}}\hat{\boldsymbol{\Gamma}})]\} = \\ &= \arg\max_{\lambda}\{\exp[-\boldsymbol{\Lambda}^{\mathrm{H}}(\boldsymbol{\Upsilon}^{-1} \circ \hat{\boldsymbol{\Gamma}})\boldsymbol{\Lambda}]\} = \\ &= \arg\max_{\lambda}\{\boldsymbol{\Lambda}^{\mathrm{H}}(\boldsymbol{\Upsilon}^{-1} \circ \hat{\boldsymbol{\Gamma}})\boldsymbol{\Lambda}\} \end{aligned} \tag{3.33}$$

where:

- $\boldsymbol{\Phi}$ is a Nx N diagonal matrix, $\boldsymbol{\Phi} = \text{diag}\{e^{i\boldsymbol{\lambda}}\}$;
- $\boldsymbol{\Lambda}$ is a N-dimensional vector, $\boldsymbol{\Lambda} = e^{i\boldsymbol{\lambda}}$;
- $\circ$ represents the Hadamard product.

Since the true coherence matrix $\boldsymbol{\Upsilon}$ is unknown, the absolute value of $\hat{\boldsymbol{\Gamma}}$ can be used as an estimate of $\boldsymbol{\Upsilon}$. Therefore, from equation 3.33, the equation 3.34 is obtained.

$$\hat{\boldsymbol{\lambda}} = \arg\max_{\lambda} \left\{ \boldsymbol{\Lambda}^{\mathrm{H}} \left(\left| \hat{\boldsymbol{\Gamma}} \right|^{-1} \circ \hat{\boldsymbol{\Gamma}} \right) \boldsymbol{\Lambda} \right\} \tag{3.34}$$

By using iterative methods for the minimization of a non-linear function, it is possible to obtain the optimal solution consisting in N optimum phase values, which can be used as an input for SqueeSAR technique.

After having identified statistically-homogeneous pixels preserving the information of point-wise permanent scatterers and after having characterized by means of PTA the distributed scatterers through N phase values, like for permanent scatterers, rather than $N(N-1)/2$, both permanent and distributed scatterers can be exploited in SqueeSAR technique, as follows:

- N_S statistically-homogeneous pixels families are identified;
- Distributed scatterers are defined all those pixels for which N_S is larger than a certain threshold;
- The sample coherence matrix is estimated for every distributed scatterer;
- The PTA algorithm is applied to each coherence matrix, the optimum N phase values are retrieved and properly combined before phase unwrapping algorithm;
- For the distributed scatterers with a phase estimates quality higher than a certain threshold, the phase values of the original SAR images are substituted with their optimized values;
- Distributed scatterers are processed jointly with permanent scatterers through the classical PS-InSAR algorithm for the estimation of scatterers displacement or height, see paragraph 3.5.1.

3.6. Radargrammetric Processing

Radargrammetry can be considered as a complementary technique with respect to interferometric processing, useful to improve DEM accuracy since it works on amplitude data and it allows to do not suffer atmospheric artifacts and all the drawbacks introduced by the phase. The integration of the radargrammetric technique in the processing, aimed at increasing the final DEM accuracy, can be a fusion at product level, exploiting the complementary advantages of the radargrammetric and interferometric techniques, or the integration can be at a techniques level, by exploiting radargrammetry to solve the phase ambiguity during phase unwrapping, improving the accuracy of

this crucial step, useful especially in the regions at latitudes over 60°, where SRTM DEM are not available as a reference.

The main drawbacks of radargrammetry lie in:

- difficult matching of corresponding points, especially in high density urban areas where multipath and complex scattering effects can degrade the results;
- feature-less areas are not suitable for height information extraction;
- geometric distortions such as layover and shadowing make matching difficult because of the strong difference in the look angle between the acquisitions.

For further discussion on this subject, refer to paragraph 4.6.

The definition of radargrammetry was stated by (Leberl, 1990): "radargrammetry is the technology of extracting geometric information from radar images". The first works on radargrammetry began after the Second World War, but they were fully developed, improved and tested only at the end of last century, with radar imaging missions experiences. The operational benefit of this technique was really appreciated only with new generation satellite SAR systems, since the very high spatial resolution and the various incidence angles significantly improved the radargrammetric performances.

In this paragraph the main radargrammetric processing steps are analyzed.

3.6.1. Acquisition of SAR Stereo Images

Two main acquisition configurations can be considered for radargrammetric processing: same-side, in which the scene is positioned at the same side respect to the position of the two radars, Fig. 3.4; or opposite-side, in which the scene is viewed from opposite sides from the two radars, Fig. 3.5. While the higher baseline of the opposite-side configuration enables a higher accuracy in the target height reconstruction because of the higher parallax value, the drawback of this acquisition configuration lies in the matching difficulties due to the stronger radiometric differences, which can prejudice the overall results without a proper images pre-processing such as radiometric inversion. Moreover, in Figg. 3.4 and 3.5 it is possible to notice the consequence of a range estimation error: the real point M migrates to the point M_e during the processing. This effect, considering an equal range estimation error in the two configurations, is less significant in the opposite-side case than in the same-side configuration. In literature, an optimum ratio between the baseline and the height of the platform to obtain a good height reconstruction accuracy can vary from 0.25 to 2, which in CSK for a same-side acquisition configuration can be achieved by choosing different beams giving a look angle difference of about 15°-20°.

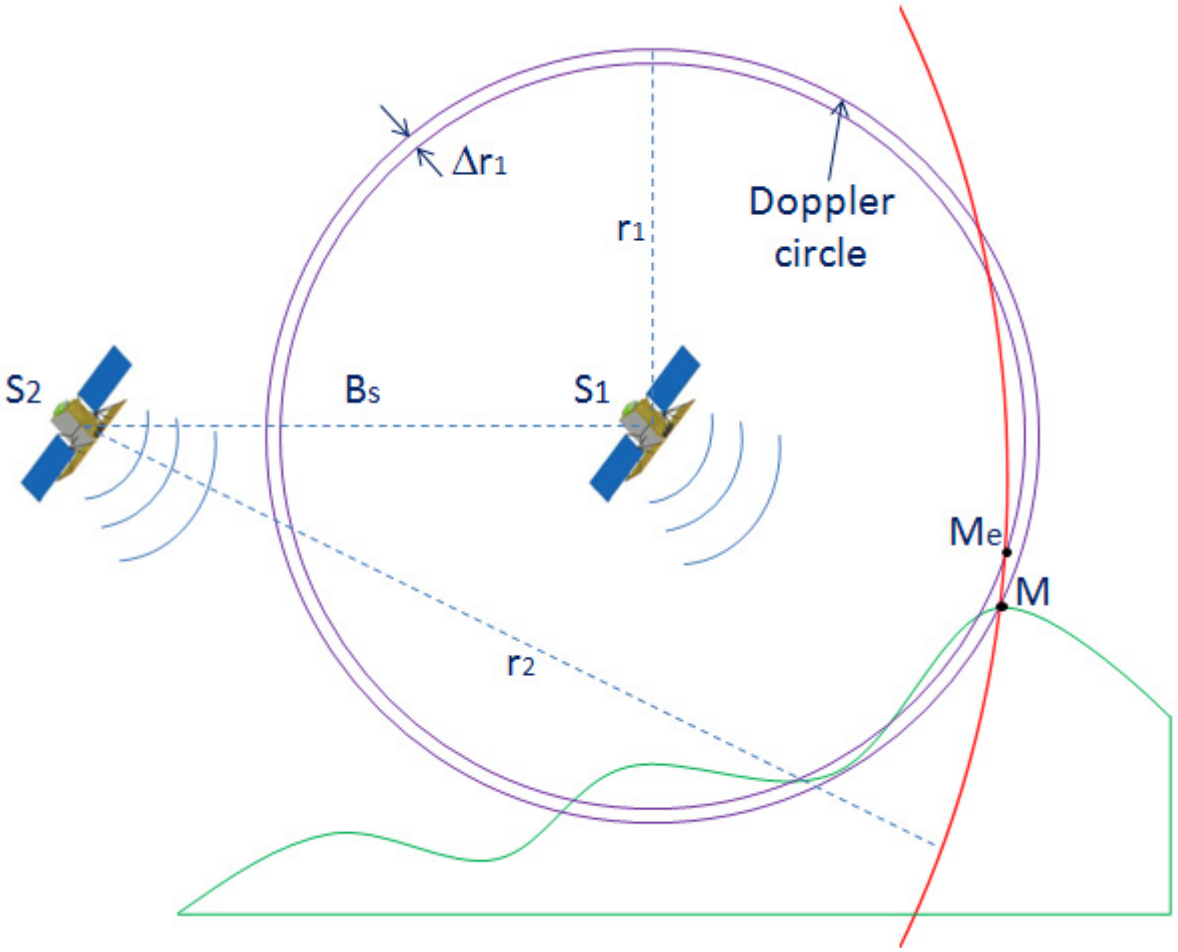

Fig. 3.4 – Same-side radargrammetric acquisition configuration.

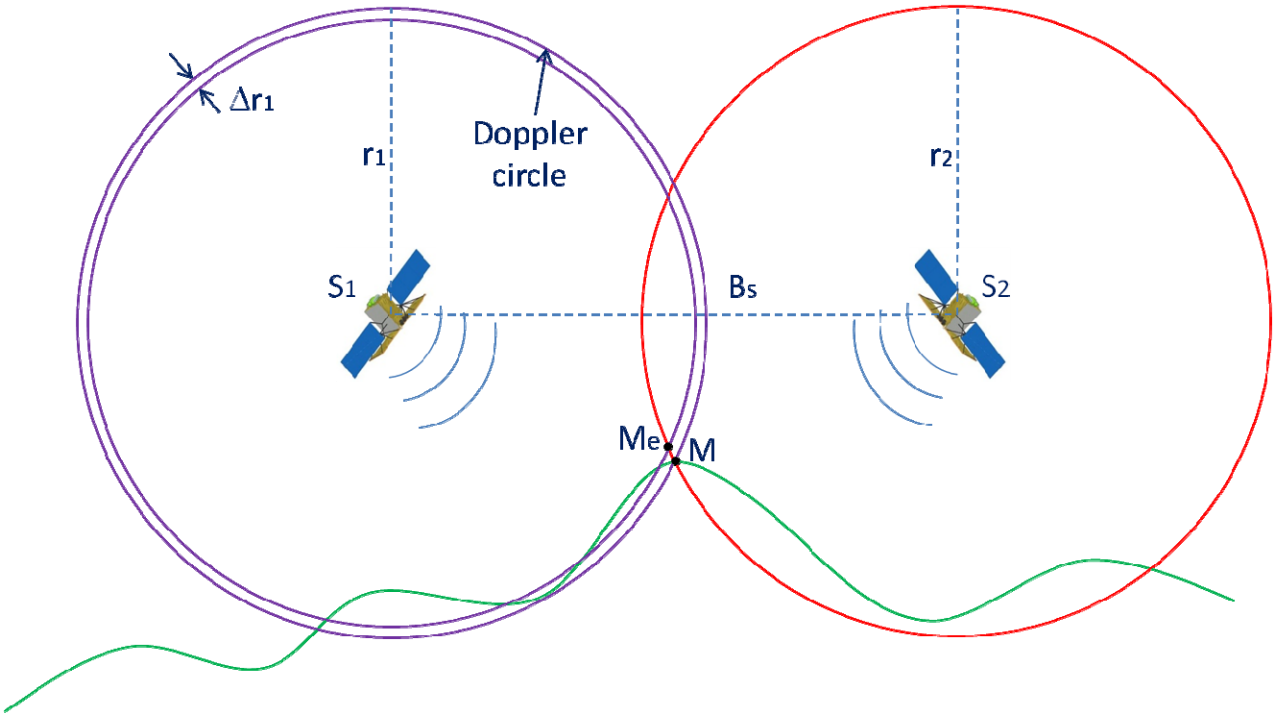

Fig. 3.5 – Opposite-side radargrammetric acquisition configuration.

3.6.2. Matching Methods

The most common image matching method is the area correlation. For a given area in the master image, the matching operation has to detect the closest one in the slave image. To find matching areas an analytical metric comparison can be used and the zero-mean normalized cross-correlation (ZNCC) can be applied, whose advantage lies in the robustness respect to the radiometric variations of the radar image. The cross-correlation coefficient ρ is defined as in equation 3.35.

$$\rho = \frac{E[I_1 I_2] - E[I_1]E[I_2]}{\sqrt{V(I_1)V(I_2)}} \tag{3.35}$$

Where I_1 and I_2 represent the amplitude images in the searching windows, $E[\dots]$ represents the mean calculated on the N pixels inside the window and $V(\dots)$ is the variance.
The value of ρ is bounded in the interval $[-1; 1]$, and the windows are considered matched for the maximum value of ρ. The coefficient ρ is calculated for each position (az_s, rg_s) of the searching window in the searching area, obtaining a correlation surface composed of the values of the coefficient ρ. The maximum of this correlation surface fives the disparity along the azimuth axis and the range axis, respectively $disp_{az}$ and $disp_{rg}$, equation 3.36.

$$\begin{aligned} disp_{az} &= |az_s(\max) - az_r| \\ disp_{rg} &= |rg_s(\max) - rg_r| \end{aligned} \tag{3.36}$$

Carrying out this process for each point of the master image, the disparity map is achieved.
It is important to observe that for difficult geometries, or strong radiometric distortions in the SAR images, the cross-correlation computation does not work very well, and a well-trained imagery analyst eye can be necessary to manually improve the matching accuracy for particularly difficult scenes. Several techniques can be applied to improve the matching operation accuracy. For instance, the use of smaller correlation windows is useful to limit false matching results of the cross-correlation method. Assuming parallel orbital paths at a constant altitude and using the epipolar geometry, (Zhang, et al., 1995), it is possible to reduce the searching area assuming that for a given point in an image, the corresponding point is located on the same azimuth line. Through the epipolar geometry it is possible to reduce the search area to a thin strip on the epipolar line, and consequently the computing time. Moreover, knowing the minimum and maximum elevation of the area it is possible to compute the minimum and maximum disparities along the range axis, limiting the research also along the range axis.

Another way to reduce the processing time is based on the application of a pyramidal procedure, (Denos, 1992), according to whom from the original image a pyramid of images is built. At each level, the image size is reduced by a factor of 2^k, with k representing the iteration step. For each iteration, the matching process allows to establish an approximate disparity map. Therefore, it is possible to predict the disparity offsets at the following level of the hierarchical process, reducing computation time. By increasing the iteration, a better accuracy is obtained for each level. The last disparity map is used to generate the DEM, (Leberl, 1990).

In (Meric, et al., 2010) a way to improve the matching operation results, and thus the DEM accuracy, is presented, based on a multi-window approach that allows to get correlation windows adapted to the compression areas.

Further details on the cross-correlation coefficient matching criterion, and a comparison with other two criteria derived from the Mean Square Error analysis, such as a ratio-based criterion and a new normalization-based criterion, is proposed in (Tupin, et al., 2002).

3.6.3. Height Reconstruction

After having performed the matching of homologous pixels between radargrammetric acquisitions, the three-dimensional geometric data have to be extracted from the stereo pair. In the radar image each pixel is referenced by its slant range and azimuth indexes.

The slant range distance r locates the pixel M on a range sphere centered on the radar position S with radius r, equation 3.37.

$$\left|\overrightarrow{SM}\right| = r \tag{3.37}$$

The azimuth position of a fixed pixel gives the Doppler cone, which is the cone of equal Doppler frequency having its apex located at the center of the range sphere, equation 3.38.

$$f_D = \frac{2}{\lambda} \cdot \frac{\vec{\dot{S}} \cdot \overrightarrow{SM}}{\left|\overrightarrow{SM}\right|} \tag{3.38}$$

In case of side-looking radar, the Doppler centroid frequency f_D is equal to zero, and the cone becomes a plane perpendicular to the velocity vector.

Equations 3.37 and 3.38 form a system of 2 equations and 3 unknowns (x, y, z), whose solutions describe a circle called Doppler circle (Fig. 3.6, also in Figg. 3.4-3.5). The Earth's model allows to get two rough solutions of the given system, and one of these can be removed according to the direction of the radar beam, with some possible approximations.

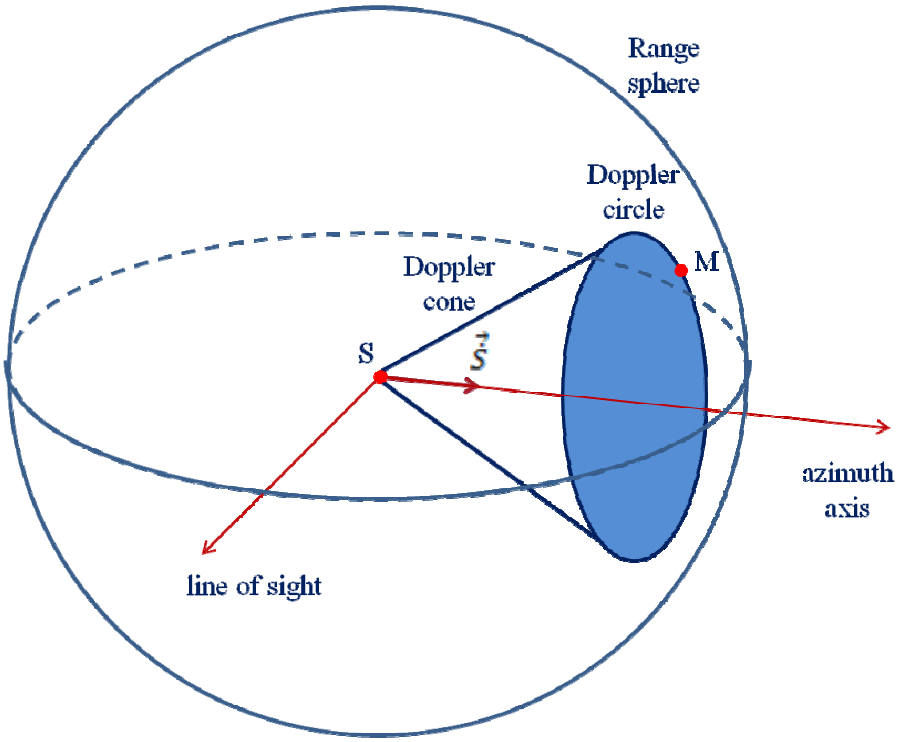

Fig. 3.6 – Range sphere, Doppler cone and Doppler circle.

Considering a stereo pair, for each radargrammetric image there is a range equation, 3.37, and a Doppler equation, 3.38, which compose the system 3.39, to be solved for the unknowns (x, y, z).

$$\begin{cases} (x - X_1)^2 + (y - Y_1)^2 + (z - Z_1)^2 = {r_1}^2 \\ (x - X_1)\dot{X}_1 + (y - Y_1)\dot{Y}_1 + (z - Z_1)\dot{Z}_1 = 0 \\ (x - X_2)^2 + (y - Y_2)^2 + (z - Z_2)^2 = {r_2}^2 \\ (x - X_2)\dot{X}_2 + (y - Y_2)\dot{Y}_2 + (z - Z_2)\dot{Z}_2 = 0 \end{cases} \tag{3.39}$$

where the position $(X_{1,2}, Y_{1,2}, Z_{1,2})$ and the velocity $(\dot{X}_{1,2}, \dot{Y}_{1,2}, \dot{Z}_{1,2})$ of the radar are required to solve the system, and can be assessed from the knowledge of the azimuth time, which in turn is a function of the pixel raw index, the zero Doppler azimuth first time and the Pulse Repetition Frequency of the SAR sensor. On the other hand, the slant range is a function of the pixel column index, the zero Doppler range first time and the column interval.

The system 3.39 is oversized because there are 3 unknowns and 4 equations. By solving 3 of the 4 equation it is possible to obtain the coordinates (x, y, z), which can be described in the geocentric reference as latitude, longitude and height, and the 4th equation can be used to check the results.

According to the general rigorous approach, system 3.40, the residuals v_i of the 4 equations can be used to derive a function to minimize, i.e. the sum of the squares of the residuals, equation 3.41, (Chen, et al., 2001).

$$\begin{cases} r_1 - \left|\overrightarrow{S_1M}\right| = v_1 \\ \dfrac{2}{\lambda r_1} \cdot \overrightarrow{S_1M} \cdot \overrightarrow{\dot{S}_1} = v_2 \\ r_2 - \left|\overrightarrow{S_2M}\right| = v_3 \\ \dfrac{2}{\lambda r_2} \cdot \overrightarrow{S_2M} \cdot \overrightarrow{\dot{S}_2} = v_4 \end{cases} \tag{3.40}$$

$$\sum_{i=1}^{4} v_i^2 \rightarrow min \tag{3.41}$$

The previous approach can be extended to n stereo-images in order to reduce the uncertainty of the final result. It would be necessary to solve a $2n$ equations system, with the sum of the squares of the residuals to be minimized, through a Gauss-Newton approach for instance.

3.7. Post-processing Techniques for Voids Filling

After having generated a DEM through an interferometric processing, even if the applied techniques guarantee very high accuracies, further post-processing is necessary to improve the quality of the DEM product, which needs to be handled in particular for voids filling in order to be considered a finished and usable DEM product.

Voids occur for different reasons, (Reuter, et al., 2007) and (Luedeling, et al., 2007):

- Water surfaces produce radar signal scattering, which prevent the interferometer from detecting meaningful reflections;
- For surface inclinations above 20°, the frequency of data voids increases because of radar shadowing;
- In desert areas, a void is more probable due to the complex dielectric constant.

Small voids can be successfully filled through interpolation of values around the edges, while large voids need to be filled with topographic information from other sources.

Many approaches have been developed for voids filling, such as:

- Fill and feather (FF);
- Inverse distance weighted interpolation-based delta surface fill (DSF);
- Triangulated irregular network-based delta surface (TDS);
- Kriging interpolation method;
- Spline interpolation method;
- Advanced spline interpolation method.

The FF method replaces a void with the most accurate elevation source available and then smoothes the transition. FF does not take into account varying vertical biases within the void, (Luedeling, et al., 2007).

The DSF process replaces the void with fill source posts that are adjusted to the DEM values found at the void interface, in which inverse distance weighted interpolation is used, (Grohman, et al., 2006).

The TDS method is similar to DSF, but voids are filled by triangulated irregular networks that connect the points bordering the voids, (Luedeling, et al., 2007).

A new method for voids filling was introduced in (Yue, et al., 2012) by improving the approach to high-accuracy surface modeling, which is based on the first and the second fundamental coefficients of surfaces, reflecting respectively lengths/angles/areas and the local warping of the surface.

CHAPTER 4
EXPERIMENTAL RESULTS ON COSMO-SKYMED DATA

This Chapter focuses on the experimental results obtained in the generation of high accuracy Digital Elevation Models (DEMs) by applying state-of-the-art interferometric techniques to a dataset of COSMO-SkyMed (CSK) images properly selected[1]. Furthermore, innovative techniques were applied in order to increase and maximize DEM accuracy, considering that DEM absolute vertical accuracy is directly related to the geolocation accuracy of DEM-geocoded products, and it strongly affects the main applications based on SAR images such as 3D modeling accuracies, intelligence preparation of battle-space, flight planning and all Line Of Sight (LOS) applications. The aim of the experimental activity was to assess the quality of the DEM which can be obtained from CSK data in the current Tandem-like orbital configuration (at the time of this Thesis), exploring relevant limitations, and to detect innovative processing strategies to increase DEM vertical accuracy.

4.1. Dataset

For the purposes of this study, nine civilian Enhanced Spotlight (ES) COSMO-SkyMed images were used, properly selected, on Pomezia (Rome), with processing level Single-look Complex Slant-range (SCS_B), containing focused data in complex format, in slant range and zero Doppler projection, as summarized in Tab. 4.1.

Tasking parameters such as off-nadir angle, interferometric baseline and orbit direction were selected in order to perform a sensitivity analysis and evaluate how DEM vertical accuracy is affected by each parameter or by proper processing techniques based on the specific dataset.

Furthermore, also Detected Ground Multilook (DGM_B) processing level, containing focused data, detected, radiometrically equalized and in ground range/azimuth projection, was exploited in order to properly apply also a radargrammetric processing to improve the interferometric DEM accuracy.

Satellite	Acquisition Time	Acquisition Mode	Orbit Direction	Beam	Polarization	Processing Level	Off-nadir Angle	Code
CSK2	2011-12-20	Spotlitgh-2 (ES)	Right Descending	31	HH	SCS_B	49.64°	1
CSK3	2011-12-21	Spotlitgh-2 (ES)	Right Descending	31	HH	SCS_B	49.64°	2

[1] Courtesy of Italian Space Agency

CSK2	2011-12-21	Spotlitgh-2 (ES)	Right Descending	11	HH	SCS_B	33.93°	3
CSK3	2011-12-22	Spotlitgh-2 (ES)	Right Descending	11	HH	SCS_B	33.93°	4
CSK2	2011-12-25	Spotlitgh-2 (ES)	Right Ascending	15	HH	SCS_B	37.52°	5
CSK3	2011-12-26	Spotlitgh-2 (ES)	Right Ascending	15	HH	SCS_B	37.52°	6
CSK2	2011-12-30	Spotlitgh-2 (ES)	Right Ascending	08	HH	SCS_B	30.85°	7
CSK3	2011-12-31	Spotlitgh-2 (ES)	Right Ascending	08	HH	SCS_B	30.85°	8
CSK3	2012-01-01	Spotlitgh-2 (ES)	Right Ascending	28	HH	SCS_B	48.04°	9

Tab. 4.1 – Dataset: civilian Enhanced Spotlight COSMO-SkyMed, courtesy of Italian Space Agency.

Moreover, sixty-six Ground Control Points (GCPs) equally distributed through the overall acquisition scene, were considered:

- a proper subset for calibration purposes during the interferometric processing;
- the remaining subset to validate the generated DEM.

It is important to stress that the GCPs used to validate the generated DEM are different from the GCPs used during the interferometric processing, which would have wrongly biased the quality measures.

Methodologically, a certification of CSK capability to generate DEM through tandem-like interferometry would need a huge dataset over several scenarios characterized by different topographic and coherence-affecting features such as vegetation, in different seasonal and atmospheric conditions, and with the availability of a DEM for validation purposes with accuracies at least one order of magnitude better than the expected accuracies of CSK DEM. However, the aim of this study is not to perform a capability certification, which cannot be conducted because of the unavailability for the purposes of this study of a large dataset and a high accuracy DEM for validation. On the contrary, this study wants to explore CSK potentialities in DEM generation and to analyze innovative techniques to maximize DEM accuracy in specific conditions.

In Tab. 4.2, a synthesis of the matching between dataset and relevant application is offered, where B_n, B_{cr} and H_a are respectively the *Normal Baseline*, *Critical Baseline* and *Height of Ambiguity*.

Application	Orbit Direction	Off-nadir Angle	Dataset	B_n	B_{cr}	H_a
~~1-day interferometry~~	~~Descending~~	~~High~~	~~1-2~~	~~23 m~~	~~-~~	~~601 m~~
1-day interferometry	Descending	Low	3-4	220 m	14859 m	33 m
1-day interferometry	Ascending	High	5-6	872 m	16646 m	9.8 m
1-day interferometry	Ascending	Low	7-8	1412 m	13755 m	4.6 m
1-day interferometry	Combination D + A	High or Low	3-4 with 7-8	-		
Radargrammetry	Same-side D	-	2-3	- Adequate B/H (about 0.3).		
Radargrammetry	Same-side A	-	8-9	- Difficult *matching* for "opposite-side" pairs.		

Tab. 4.2 – Matching between available dataset and relevant application.

In particular, the dataset allows to perform interferometry with a decorrelation time of 1 day, both in ascending and descending orbit directions, both with a low and high off-nadir angle, and in several *Normal Baseline* conditions. These conditions are very useful to perform a sensitivity analysis.

Theoretically, DEM generated from CSK interferometric data at low incidence angles will be more accurate because the wider chirp bandwidth, used to guarantee a constant ground-range resolution, gives higher coherence values.

Among all the possible interferometric dataset, the pair 1-2 was discarded because its *Height of Ambiguity*, which is the height corresponding to a 2π phase variation (one interferometric cycle), is higher than the topographic variation of the scene. By increasing the *Normal Baseline* value, the sensitivity to topographic variations will increase, but the very dense interferogram fringes will make the phase unwrapping processing very difficult. At the *Critical Baseline* B_{cr}, the interferometric coherence is zero and there is not correlation any more between the two acquisitions.

$$B_{cr} = \frac{\lambda R tan(\theta)}{2R_r} \tag{4.1}$$

where λ is the acquisition wavelength, R is the slant range distance, R_r is the pixel spacing in slant range, θ is the acquisition incidence angle. However, it is better to avoid normal baseline values higher than half the critical value, which is an optimal baseline value because it minimizes phase errors. The selected dataset allows also a combination between a DEM generated from an ascending pair and from a descending pair, in order to smooth layover and shadow effects. Furthermore, the dataset allows to perform same-side radargrammetry both in ascending and descending orbit

directions, with a B/H ratio approximately equal to 0.3 with a difference of about 15-20° in the off-nadir angles. On the contrary, opposite-side radargrammetry was not considered because several experimental tests highlighted that even if the geometric acquisition parameters would allow very good results, the difficulties in the matching phase bring the overall accuracy down.

4.2. Interferometric Processing

Several DEM were generated from the dataset through interferometric techniques and then validated, exploiting the specific different acquisition parameters of each interferometric pair in terms of normal baseline, incidence angle and orbit direction.

The interferometric processing applied was explained in the previous Chapters, while in the following part of this paragraph the main processing choices are pointed out.

During processing for DEM generation, both reference SRTM[2] coarse DTED-1 DEM, (National Geospatial-Intelligence Agency, 2009), and calibration GCP were referred to the ellipsoid WGS84, because *geocoding* and *flattening* operations are mathematically corrected if an ellipsoidal height is considered. Finally, EGM96 geoid was added to obtain orthometric heights.

A DEM-assisted coregistration, if applied, would allow to compensate for local distortions, (D.O. Nitti, 2008): an input DEM is useful to refine the offset vectors estimation when polynomial corrections are not able to locally interpolate the topography. A simulated topographic phase, if removed after the coherent cross-correlation in order to compensate the phase cycles due to the topography, would allow to obtain the position of the maximum with sub-pixel accuracy.

In order to increase the phase Signal-to-Noise-Ratio (SNR) and to have a better coherence estimation, to the detriment of spatial resolution, both in range and in azimuth a multi-look factor was chosen equal to 2.

During the interferogram generation step, optionally Common Band Filtering was applied, in order to compensate for the effects on the coherence of the non-common portions of the Doppler band between the two interferometric acquisitions, to the detriment of azimuth spatial resolution, Fig. 4.1.

The contribution to the interferometric phase proportional to the slant range displacement *s* of the point targets was estimated and removed (*interferogram flattening*), which is related to the slight difference in the antenna positions (second term in equation 4.2).

$$\Delta\phi = -\frac{4\pi}{\lambda}\frac{B_n q}{R sin\theta} - \frac{4\pi}{\lambda}\frac{B_n s}{R tan\theta} \tag{4.2}$$

[2] SRTM: Shuttle Radar Topography Mission

where θ is the radiation incidence angle with respect to the reference, q is the altitude difference between the point targets, $\Delta\phi$ is the interferometric phase variation and R is the radar-target distance. As a result, a phase map only proportional to the relative terrain altitude was generated. By generating synthetic fringes from a coarser resolution DEM or from an ellipsoidal height, using a backward geocoding approach, and then cross-multiplying them by the SAR interferogram, it was possible to remove most of the low frequency components of the wrapped phase, and to make phase unwrapping easier.

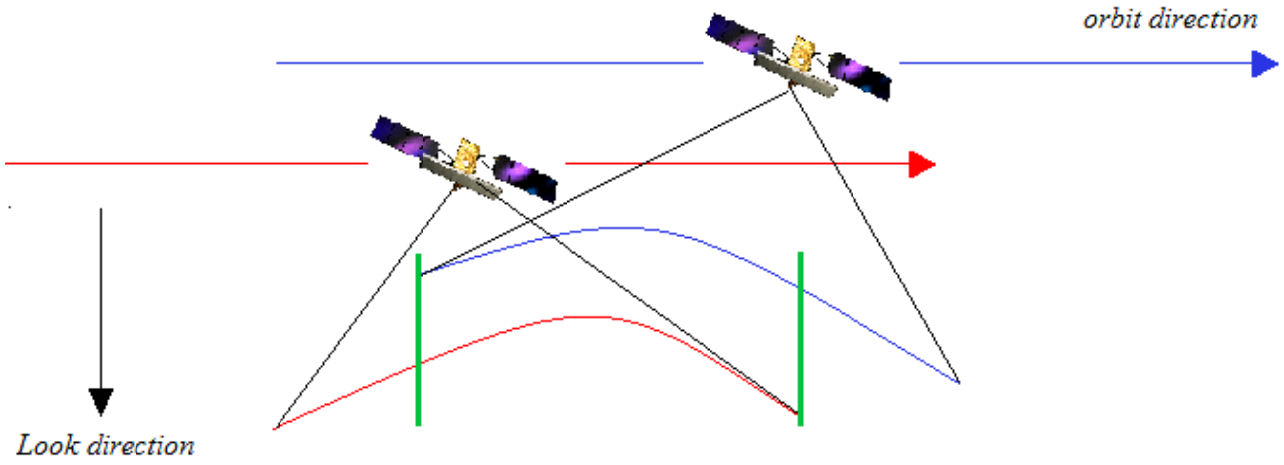

Fig. 4.1 – Common Band Filtering pictorial view.

The interferogram was filtered to reduce phase noise through an extension of the Goldstein method, (I. Baran, 2003), where the adaptive filter band was optimized on the base of the local coherence.

To perform *phase unwrapping*, the Minimum Cost Flow (MCF) algorithm was used, (Eineder, et al., 1998), which minimizes the integer number of cycles to add to the phase variation in order to make the phase gradient irrotational, $\nabla \wedge \nabla\phi = \mathbf{0}$, so that the unwrapped phase field is independent on the followed integration path.

In order to minimize unwrapping errors, the interferogram was decomposed and unwrapped at a lower resolution, and then reconstructed at the original resolution. Higher the number of decomposition levels is, better and faster the interferogram is unwrapped. However, if the number of decomposition levels is too high, aliasing effects could arise and affect the unwrapped phase quality. Therefore, a first decomposition level equal to 1 was chosen, corresponding to an under-sampling factor equal to 3. If *unwrapping islands* were observed in the unwrapped phase, the number of decomposition levels was increased to 2, while if aliasing was observed in the areas of steep topographic residual, the number of decomposition levels was decreased to 0.

During conversion from unwrapped phase to height and geocoding, a range-Doppler rigorous approach was used and a grid size slightly lower than twice the interferogram ground-range resolution was chosen, representing the lowest value which does not require an interpolation.

4.3. Sensitivity Analysis

From a theoretical point of view, (Caltagirone, et al., 2011), through equations 4.3 it is possible to perform a sensitivity analysis of the absolute and relative height measurement accuracy, the ambiguity separation height and the maximum resolvable slope respect to

$$\delta z_B = -r\,tan(\theta-\xi)\left(sin\theta + cos\theta tan\tau_y\right)\frac{\delta B}{B}$$

$$\delta z_\xi = r\left(sin\theta + cos\theta tan\tau_y\right)\delta\xi$$

$$\delta z_\phi = \frac{r\lambda\left(sin\theta + cos\theta tan\tau_y\right)}{4\pi B cos(\theta-\xi)}\sigma\phi \qquad (4.3)$$

$$z_{unamb} = \frac{r sin\theta\lambda}{4B cos(\theta-\xi)}$$

$$\tau_{y,max} = \theta - tan^{-1}\left(\frac{cB}{rBW\lambda}\right)$$

describing respectively:

- δz_B: the sensitivity of the absolute height evaluation to the uncertainty in the knowledge of the baseline length δB, which depends on the slant range r of the target and so the observation angle θ, on the baseline tilt ξ and on the terrain range slope τ_y;
- δz_ξ: the sensitivity of the absolute height evaluation to the uncertainty in the knowledge baseline tilt $\delta\xi$, which depends on the slant range r of the target and so the observation angle θ and on the range slope τ_y;
- δz_ϕ: the precision in determining the height related mainly with the standard deviation of the phase measurement, which depends on the slant range r of the target and so the observation angle θ, on the wavelength λ, on the terrain range slope τ_y, on the baseline tilt angle ξ, on the baseline length B and on the phase standard deviation $\sigma\phi$;
- z_{unamb}: the ambiguity separation height, which depends on the slant range r of the target and so the observation angle θ, on the baseline tilt ξ and length B and on the wavelength λ;
- $\tau_{y,max}$: the maximum resolvable terrain slope, which depends on the observation angle θ and slant range r, on the baseline length B, on the wavelength λ, on the transmission bandwidth BW and on the light speed c.

In the following paragraphs, the results of an experimental analysis are discussed, which was performed to assess the sensitivity of the DEM accuracy and the interferometric coherence both

respect to the acquisition parameters of the interferometric pairs (i.e. normal baseline, incidence angle and orbit direction), and respect to processing options such as:

- the application of a classical or a "coarse DEM-assisted" co-registration of the interferometric images;
- the application or not during the interferogram generation step of a Common Band Filtering in order to filter out the non-common parts of the shifted azimuth spectra of the interferometric images and to fully capture the scene potential coherence even if at a lower azimuth spatial resolution;
- the usage or not of calibration GCP during the interferometric processing.

4.3.1. Processing Options

In this paragraph, the obtained experimental results are proposed. In Fig. 4.2, it is shown the interferometric pair of CSK images with a temporal decorrelation of one-day used as a first input to the interferometric processing for DEM generation and the subsequent sensitivity analysis. In this first case, a DEM-assisted coregistration and Common Band Filtering were applied, and a SRTM DTED-1 with a grid spacing equal to 90 m together with 10 GCP for calibration purposes were used during processing.

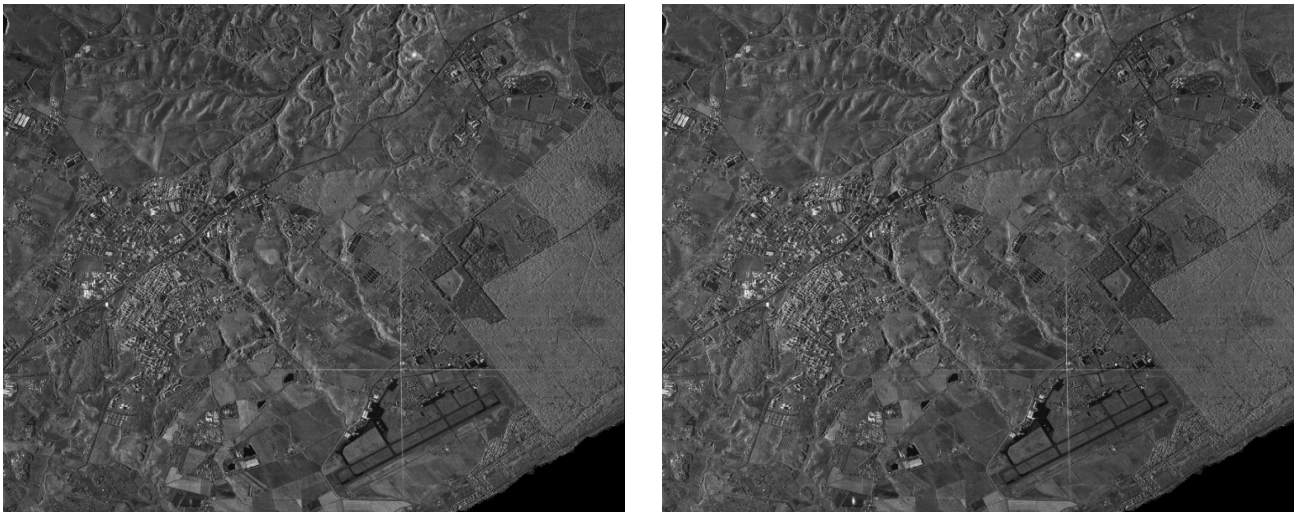

CSK 2 – ES (courtesy of ASI)
Single Look Complex
December 21st 2011
Right Descending
Off-nadir angle = 33.93°

CSK 3 – ES (courtesy of ASI)
Single Look Complex
December 22nd 2011
Right Descending
Off-nadir angle = 33.93°

Fig. 4.2 – CSK one-day interferometric pair, B_n = 220 m, H_a = 33 m, Tab. 4.1 – code: 3-4.

According to (N. Yague-Martinez, 2010), the coregistration accuracy can be computed through the equation 4.4, which is given by the Cramer-Rao bound in case coherent cross-correlation is used for coregistration (i.e. using *complex* image samples):

$$\sigma_{CR} = \sqrt{\frac{3}{2N}} \frac{\sqrt{1-\gamma^2}}{\pi\gamma} osf^{\frac{3}{2}} \tag{4.4}$$

where N is the number of pixels of the correlation window, *osf* is the oversampling factor and γ is the coherence value. Coherent cross-correlation is the optimum (maximum likelihood) estimator for differential shift of partially correlated signals, but it is very sensitive to phase differences between corresponding windows because of topographic fringes, for instance.

The coregistration accuracy, computed as the mean of the shift values over all the coregistration windows, is equal to:

Range: 0.24 pixel	**Azimuth: 0.04 pixel**

In Fig. 4.3 the coherence map is shown.

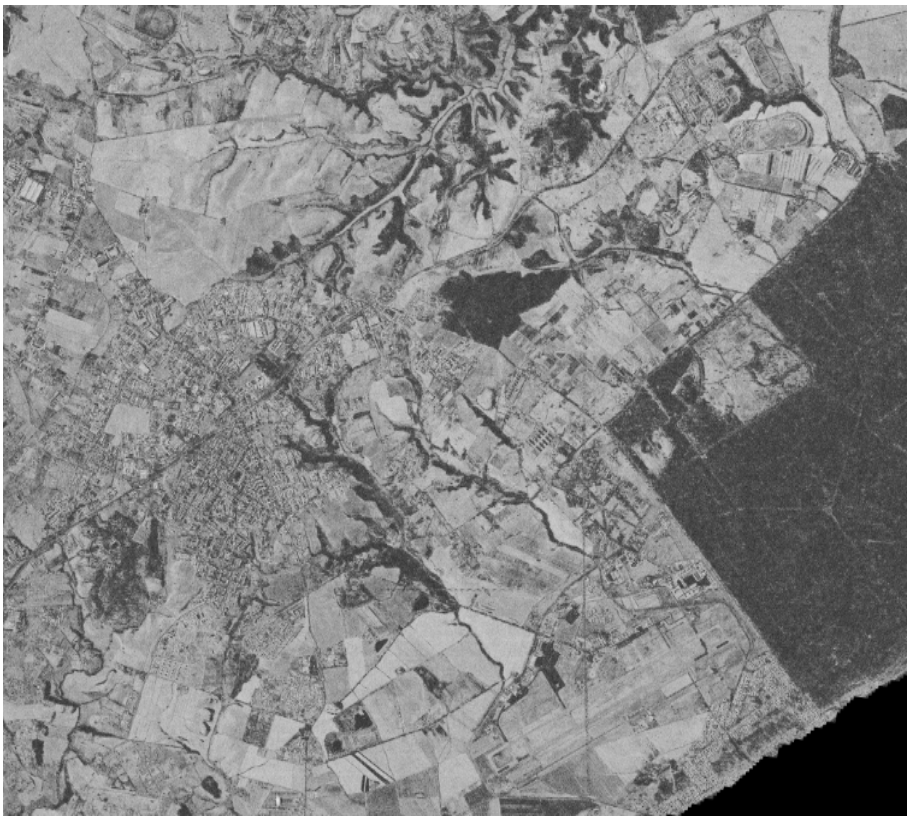

Fig. 4.3 – Coherence Map (DEM-assisted coregistration).

The coherence values were computed to be equal to:

Mean coherence: 0.54	**Standard deviation: 0.19**	**Modal value: 0.65**

The coherence map has local peaks up to 0.99, but its mean value is pull-down by vegetated areas, which have a very low decorrelation time and thus a very low coherence value being the decorrelation time between the two CSK acquisitions equal to one day.

In Fig. 4.4 the interferogram is shown, from left to right, respectively after flattening and after filtering.

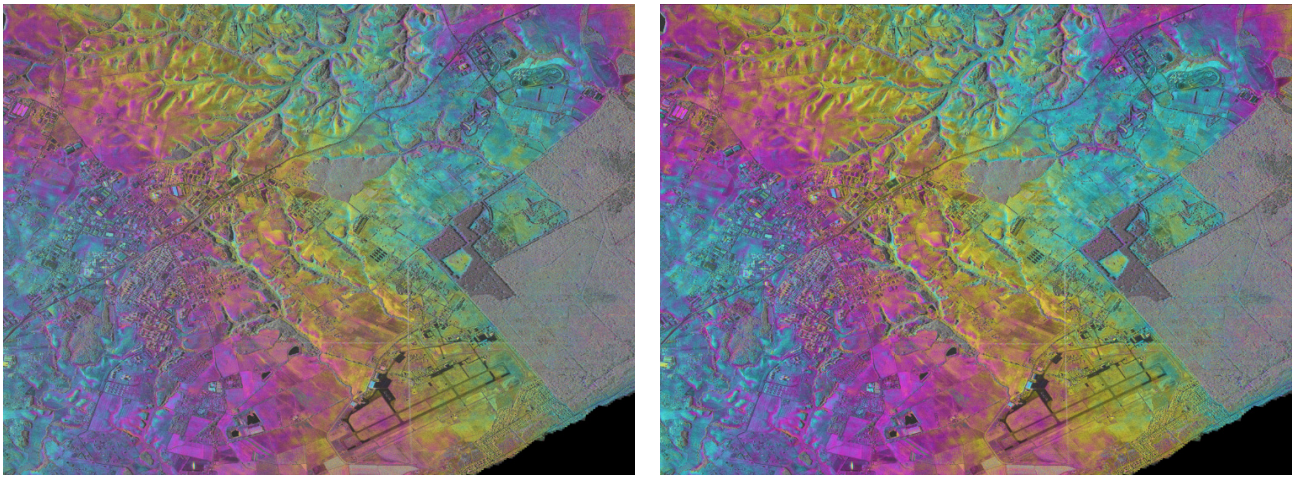

Fig. 4.4 – Interferogram (left: after flattening; right: after filtering).

Finally, a DEM was generated and geocoded, Fig. 4.5, after phase unwrapping and phase-to-height conversion, with a posting (i.e. grid size) of 2 m according to the considerations of paragraph 4.2.

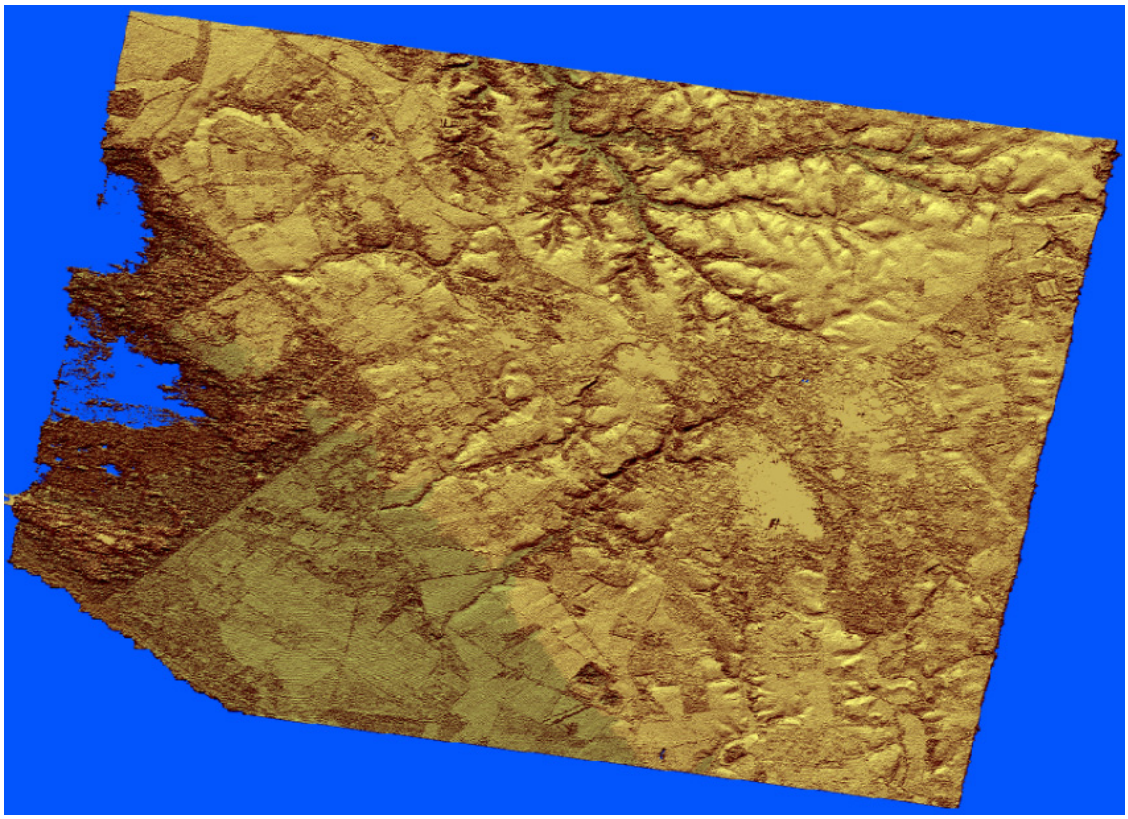

Fig. 4.5 – DEM generated from CSK interferometric data (DEM-assisted coregistration and CBF).

Through a comparison of the DEM generated from CSK interferometric data with all the GCP available for validation purposes and homogeneously distributed on the scene, it was possible to obtain the DEM quality parameters synthesized in Tab. 4.3, which allow to place CSK-generated DEM between NGA quality standards *High Resolution Elevation-Geographic Projection* (*HRE-GP*) and *High Resolution Elevation-80* (*HRE-80*), (National Geospatial-Intelligence Agency, 2009).

Comparison between DEM and validation GCP height values	
Mean of differences	2.95 m
RMS	5.07 m
Min differences	-7.33 m
Max differences	14.84 m
Absolute Vertical Accuracy LE90 [3]	**8.57 m**
Relative Vertical Accuracy LE90	**5.72 m**

Tab. 4.3 – CSK-generated DEM quality parameters (with DEM-assisted coregistration and CBF).

The relative accuracy derives from the comparison between the differences in GCP height values and the corresponding differences in DEM points heights.

Even if this is only a test case, and even if to achieve certifiable results it is necessary to perform an extensive experimental campaign in several scenarios and different conditions, it is significant to explore the capabilities of COSMO-SkyMed satellites in tandem-like orbital configuration, and to perform a sensitivity analysis to know how to set acquisition and processing parameters in order to maximize the DEM accuracy which can be obtained in the current orbital configuration, also by applying innovative post-processing techniques.

A first sensitivity analysis is performed respect to the application during the interferometric processing of a Common Band Filtering, specifically after the coregistration step of the same Single-look Complex Slant-range interferometric pair, in Fig. 4.2. A different azimuth pointing of antennas during acquisitions, which can be addressed through Doppler inter-calibration, causes a shift of Doppler Centroids and azimuth spectra between interferometric images, which results in a phase noise contribution and coherence reduction. In particular, the azimuth spectral correlation is given by equation 4.5.

$$\gamma = 1 - \frac{\Delta f_{Dc}}{B_{az}} \tag{4.5}$$

[3] LE90: Linear Error at 90% means that the error of the 90% of the points does not exceed the accuracy threshold.

where Δf_{Dc} represents the Doppler Centroids shift and B_{az} the azimuth band. It is easy to understand how non-common spectral contributions introduce decorrelation. To improve coherence, Common Band Filtering can be applied, to the detriment of azimuth spatial resolution which gets worse of a quantity directly related to the percentage of B_{az} which is not used, Fig. 4.6.

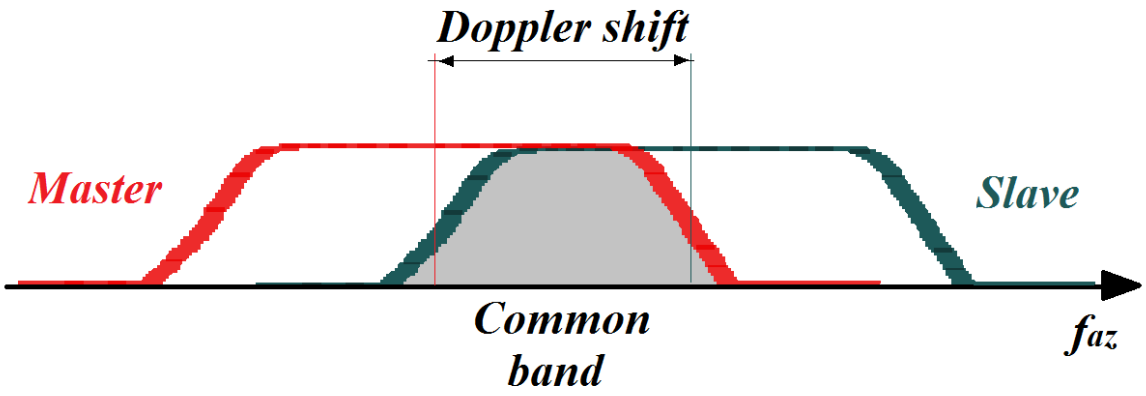

Fig. 4.6 – Common Band Filtering.

If Common Band Filtering is not applied, the generated DEM, Fig. 4.7, returns the accuracies summarized in Tab. 4.4, which can be compared with the previous results. In this specific case, the Doppler Centroids shift is equal to 674.8 Hz.

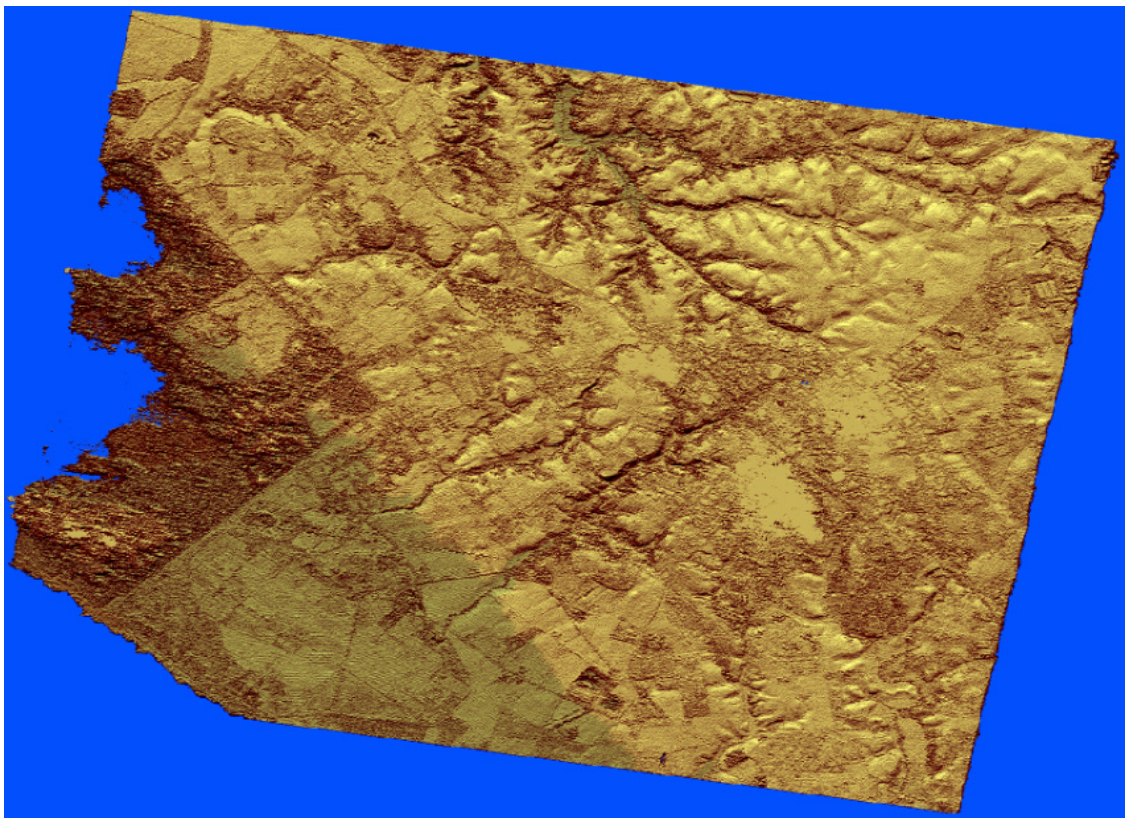

Fig. 4.7 – DEM generated from CSK interferometric data (DEM-assisted coregistration, no CBF).

The coherence values were computed to be equal to:

Mean coherence: 0.50	Standard deviation: 0.19	Modal value: 0.60

with a deterioration percentage of the mean coherence equal to **7.4%** respect to the CBF case.
The DEM vertical accuracies reported in Tab 4.4 represent a deterioration percentage respect to the CBF case of **1.9%** and **19.6%** respectively in the absolute and relative vertical accuracy.

Comparison between DEM and validation GCP height values	
Absolute Vertical Accuracy LE90	8.73 m
Relative Vertical Accuracy LE90	6.84 m

Tab. 4.4 – CSK-generated DEM quality parameters (DEM-assisted coregistration, no CBF).

The slight deterioration of the absolute vertical accuracy compared to the deterioration of the relative vertical accuracy is mainly due to the GCP-assisted calibration.

A sensitivity analysis was performed also respect to the DEM-assisted coregistration. If the coregistration of the same interferometric pair in Fig. 4.2 is not DEM-assisted, a worsening of the coregistration accuracy and coherence is experimented.

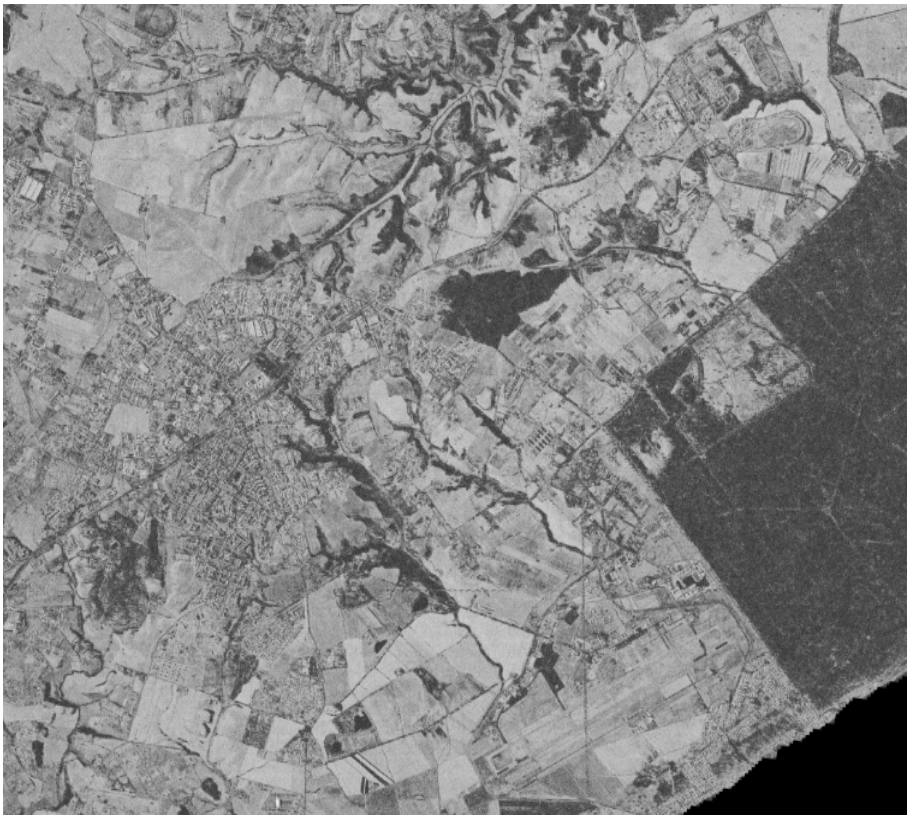

Fig. 4.8 – Coherence Map (no DEM-assisted coregistration).

The worsening percentages in coregistration accuracy and mean coherence were equal respectively to **0.2%** and **0.02%**. The low effect is due mainly to the slight topographic variation of the scene.

A further sensitivity analysis was performed respect to the usage of calibration GCPs during processing. If no calibration GCP are used during processing of the same interferometric pair in Fig. 4.2, a worsening of the absolute vertical accuracy is experimented.
In particular, if a SRTM DTED-1 was used for *flattening* and *geocoding* purposes instead of precise calibration GCP, an absolute vertical accuracy of the generated DEM equal to **9.08 m** (LE90) is obtained, corresponding to a worsening percentage of **5.9%**.

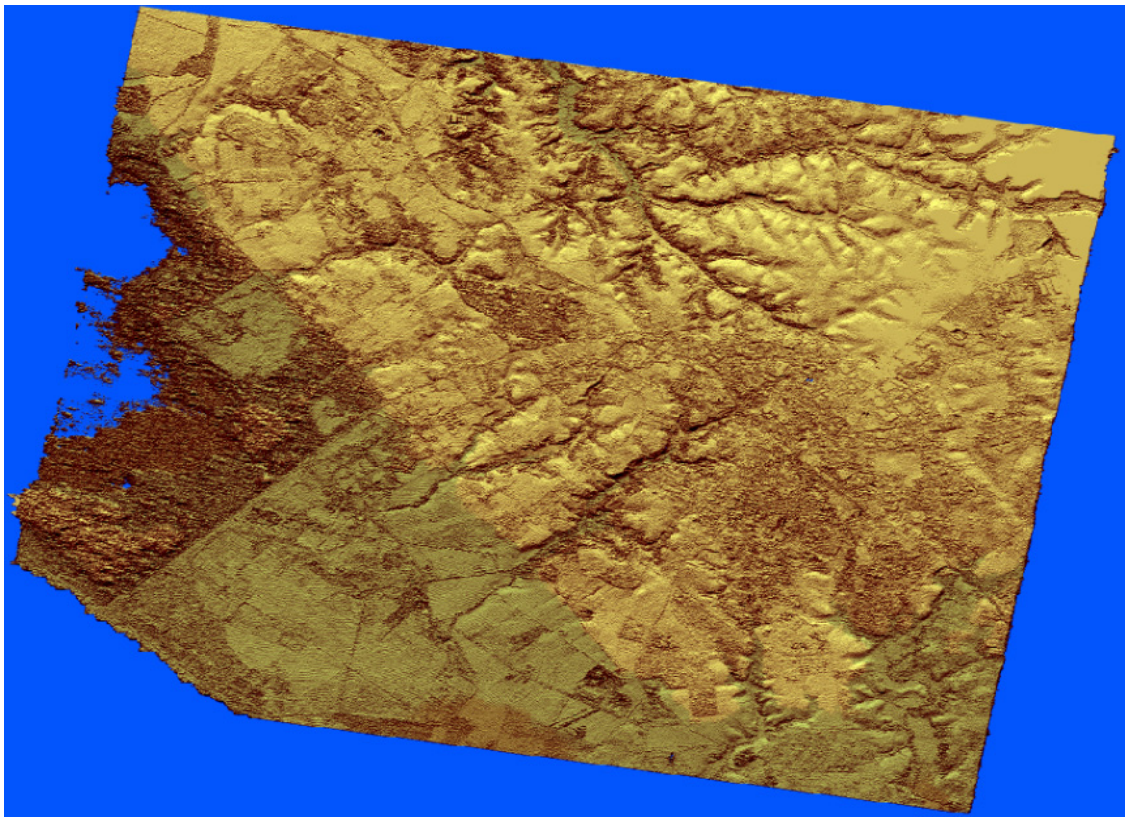

Fig. 4.9 – DEM generated from CSK interferometric data (no DEM-assisted coregistration, CBF).

4.3.2. Acquisition Parameters

A second interferometric pair, Fig. 4.10, was used for DEM generation, in order to perform a sensitivity analysis respect to different acquisition parameters.

Both DEM-assisted coregistration and Common Band Filtering were applied during processing, and calibration GCPs were used.

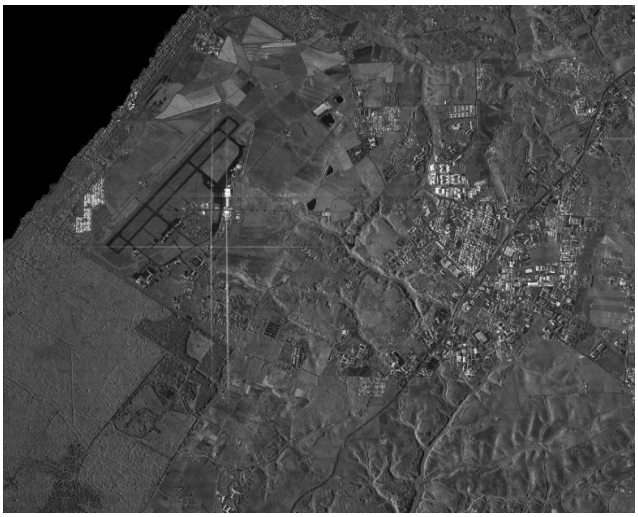

CSK 2 – ES (courtesy of ASI)
Single Look Complex
December 25th 2011
Right Ascending
Off-nadir angle = 37.52°

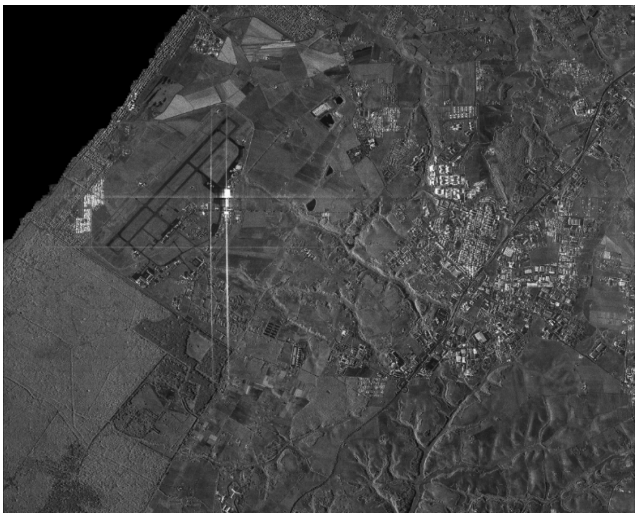

CSK 3 – ES (courtesy of ASI)
Single Look Complex
December 26th 2011
Right Ascending
Off-nadir angle = 37.52°

Fig. 4.10 – CSK one-day interferometric pair, B_n = 872 m, H_a = 9.8 m, Tab. 4.1 – code: 5-6.

In Fig. 4.11 coherence map and flattened, filtered interferogram are represented.

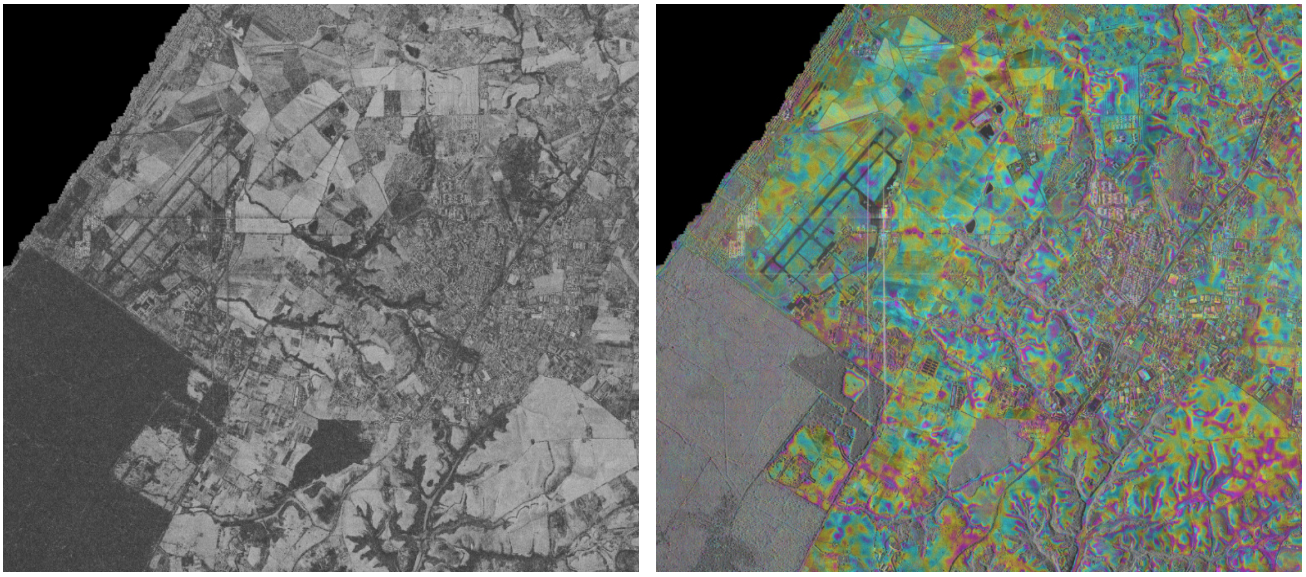

Fig. 4.11 – Left: coherence map; Right: flattened, filtered interferogram.

The coregistration accuracy, computed as the mean of the shift values over all the coregistration windows, is equal to:

Range: 0.06 pixel	**Azimuth: 0.07 pixel**

The coherence values were computed to be equal to:

Mean coherence: 0.45	**Standard deviation: 0.18**	**Modal value: 0.55**

In the interferogram, it is possible to see how increasing the normal baseline B_n, fringes density increases, improving the sensitivity to topographic changes but making phase unwrapping more difficult.

After phase unwrapping and phase-to-height conversion, a DEM was generated and geocoded, Fig. 4.12, with a posting of 2 m.

In tandem-like orbital configuration, with one-day temporal decorrelation between interferometric acquisitions, beyond the decorrelation of the acquired scene (e.g. vegetation has a very low decorrelation time and pulls down the mean coherence value), also different atmospheric conditions which may arise during acquisitions and cannot be controlled yield lower coherence values. This consideration suggests that if an interferometric campaign is conducted for production purposes, CSK orbital configuration should be changed in order to reduce temporal decorrelation, maximize the probability of unchanged atmospheric conditions between acquisitions and control the coherence values. Moreover, in this case the higher normal baseline causes a lower correlation between acquisitions.

As reported in Tab. 4.5, it is possible to observe how a lower mean coherence value has a direct impact on the DEM quality, because coherence affects phase dispersion, which in turn affects height dispersion.

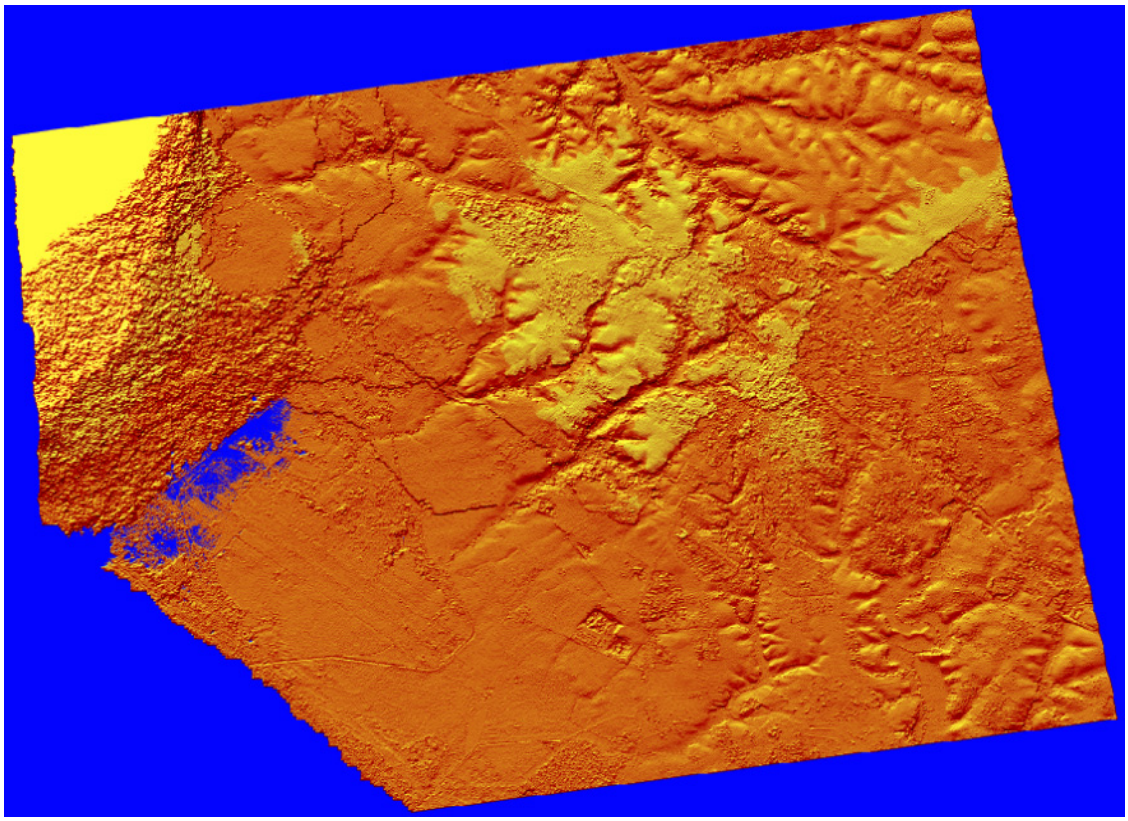

Fig. 4.12 – DEM generated from CSK interferometric data (DEM-assisted coregistration and CBF).

Comparison between DEM and validation GCP height values	
Min differences	-17.2 m
Max differences	28.01 m
Absolute Vertical Accuracy LE90	**23.31 m**
Relative Vertical Accuracy LE90	**20.48 m**

Tab. 4.5 – CSK-generated DEM quality parameters (with DEM-assisted coregistration and CBF).

A third interferometric pair, Fig. 4.13, was used for DEM generation, in order to further improve the sensitivity analysis respect to different acquisition parameters.

Both DEM-assisted coregistration and Common Band Filtering were applied during processing, and calibration GCPs were used.

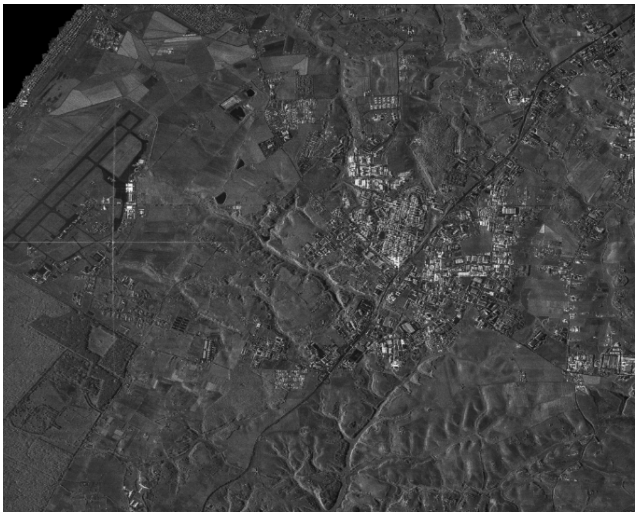

CSK 2 – ES (courtesy of ASI)
Single Look Complex
December 30th 2011
Right Ascending
Off-nadir angle = 30.85°

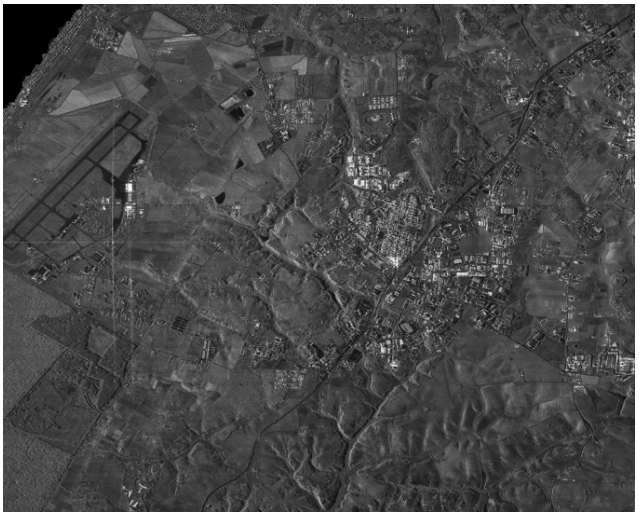

CSK 3 – ES (courtesy of ASI)
Single Look Complex
December 31th 2011
Right Ascending
Off-nadir angle = 30.85°

Fig. 4.13 – CSK one-day interferometric pair, B_n = 1412 m, H_a = 4.6 m, Tab. 4.1 – code: 7-8.

In Fig. 4.14 coherence map and flattened, filtered interferogram are represented.

The coregistration accuracy, computed as the mean of the shift values over all the coregistration windows, is equal to:

Range: 0.06 pixel	**Azimuth: 0.04 pixel**

The coherence values were computed to be equal to:

Mean coherence: 0.49	**Standard deviation: 0.18**	**Modal value: 0.55**

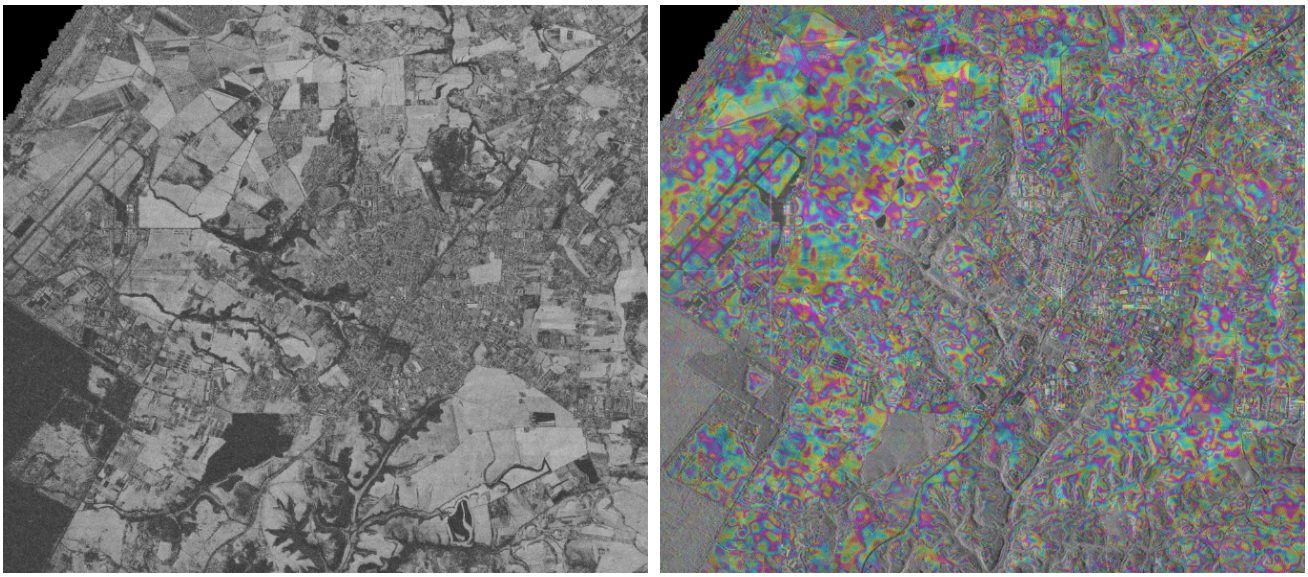

Fig. 4.14 – Left: coherence map; Right: flattened, filtered interferogram.

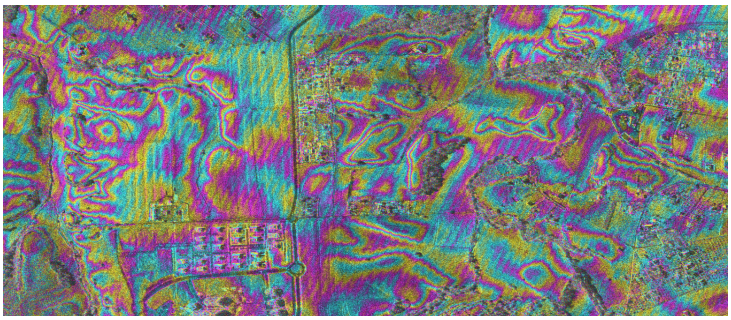

Fig. 4.15 – Zoom of the flattened, filtered interferogram.

In the interferogram, the higher normal baseline B_n produced a higher fringes density, as shown in Fig. 4.15, while the low coherence areas are mainly due to the vegetation low decorrelation time. After phase unwrapping and phase-to-height conversion, a DEM was generated and geocoded, Fig. 4.16, with a posting of 2 m, whose accuracies are summarized in Tab. 4.6.

Comparison between DEM and validation GCP height values	
Min differences	-20.8 m
Max differences	6.75 m
Absolute Vertical Accuracy LE90	**11.1 m**
Relative Vertical Accuracy LE90	**8.45 m**

Tab. 4.6 – CSK-generated DEM quality parameters (with DEM-assisted coregistration and CBF).

The worsening in the coherence values, compared to the interferometric pair in Fig. 4.2, was partially compensated by the higher normal baseline, for the purposes of the DEM quality, in accordance to equation 4.6:

$$\sigma_h = \sigma_\phi \frac{R\lambda \sin\vartheta}{4\pi B_n} \tag{4.6}$$

where σ_ϕ and σ_h are respectively the phase and height dispersions, and σ_ϕ increases for lower coherences γ.

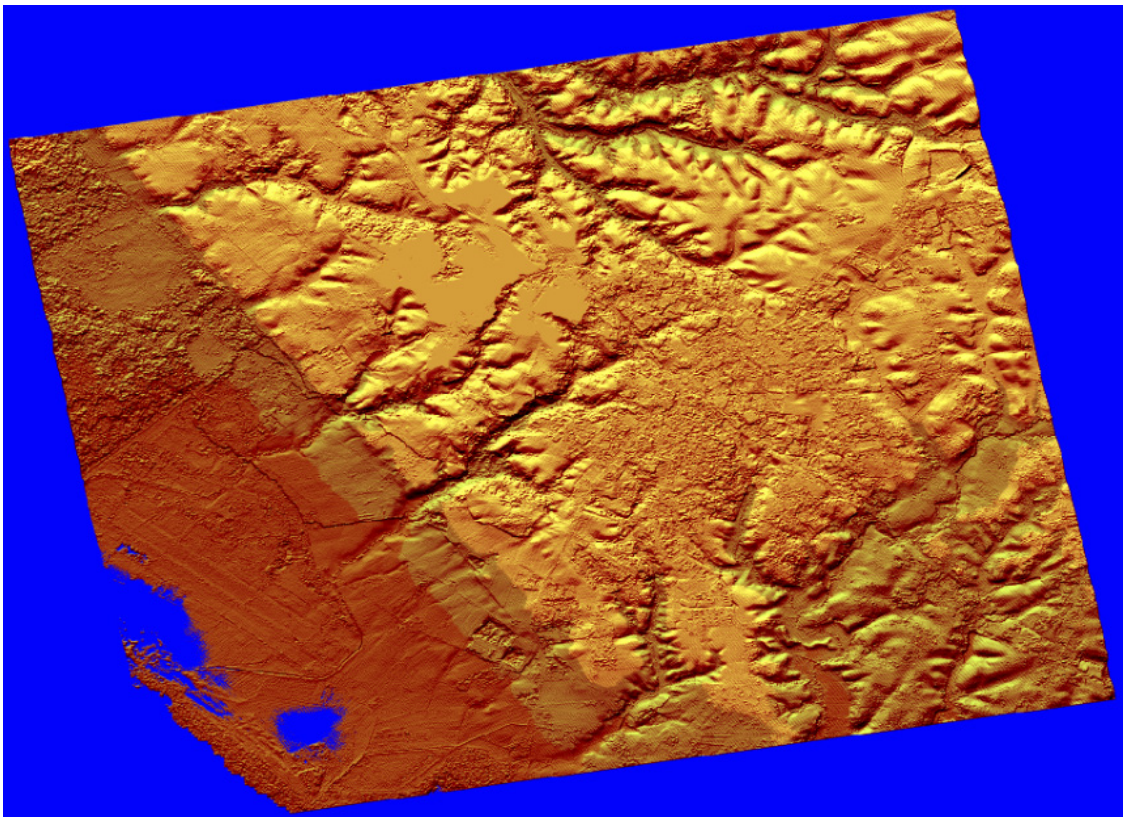

Fig. 4.16 – DEM generated from CSK interferometric data (DEM-assisted coregistration and CBF).

4.4. DEM Merging Strategies

In the previous paragraphs, a sensitivity analysis was performed to assess how the quality of a DEM generated through interferometric techniques from CSK interferometric pairs can be improved by a proper choice of several acquisition parameters such as normal baseline and incidence angle, and by a proper processing options selection, such as a DEM-assisted coregistration, the application of Common Band Filtering and the usage of calibration GCP during processing.

In the following, different DEM merging strategies will be pointed out and analyzed, in order to improve DEM quality and accuracies. In particular, a first merging technique will be applied to interferometric DEMs generated respectively from ascending and descending pairs in order to mitigate layover and shadow effects. A second merging technique will consist in the fusion, based on a wavelet approach, of a high accuracy DEM generated from CSK interferometric pairs and a low accuracy DEM deriving from SRTM mission (e.g. DTED-1), in order to mitigate the

atmospheric disturbances due to the repeat-pass interferometry, which reside in the low frequencies, by injecting the low spatial frequencies of the low accuracy SRTM DEM, which was corrected for the atmospheric effects, preserving at the same time the high spatial frequencies and details information of the high accuracy CSK DEM.
In both cases, a quantitative assessment of the achieved improvements will be performed.

4.4.1. Ascending-Descending Merging

Interferometric DEMs generated from CSK ascending and descending pairs were combined to mitigate the effects of geometric distortions such as layover and shadow. Then, a quantitative assessment of the accuracies improvement was performed.
The merging principle which was used is based on a weighted mean of the height values of the merged DEMs, where the weights are the *height precisions* which are computed from the phase standard deviations in accordance to equation 4.6, and depend on normal baseline and coherence, (P. Rosen, 2000).

$$\sigma_h = \sigma_\phi \frac{R\lambda \sin\vartheta}{4\pi B_n} \tag{4.6}$$

where σ_ϕ is given by equation 4.7:

$$\sigma_\phi = \frac{1}{\sqrt{2NL}} \frac{\sqrt{1-\gamma^2}}{\gamma} \tag{4.7}$$

The previous equations mean that dividing by 2π the height of ambiguity, it is achieved the height which is possible to discriminate with the normal baseline B_n for every degree of interferometric phase. So, multiplying this value for the phase dispersion an estimate of the DEM local vertical accuracy is achieved.
Fig. 4.17 shows, from left to right, respectively the DEM generated from the CSK interferometric pair coded 3-4 (ref. Tab. 4.1), right descending, and the DEM generated from the CSK interferometric pair coded 7-8 (ref. Tab. 4.1), right ascending, along with the main features of each DEM.
In particular, the right descending DEM was generated with a posting of 2.5 m, an absolute vertical error of **11.88 m** and a relative vertical error of **8.17 m**, from a CSK pair with an off-nadir angle of 33.93°, a normal baseline B_n of 220 m and a height of ambiguity H_a of 33 m. The right ascending DEM was generated with a posting of 2.5 m, an absolute vertical error of **10.85 m** and a relative

vertical error of **8.65 m**, from a CSK pair with an off-nadir angle of 30.85°, a normal baseline B_n of 1412 m and a height of ambiguity H_a of 4.6 m.

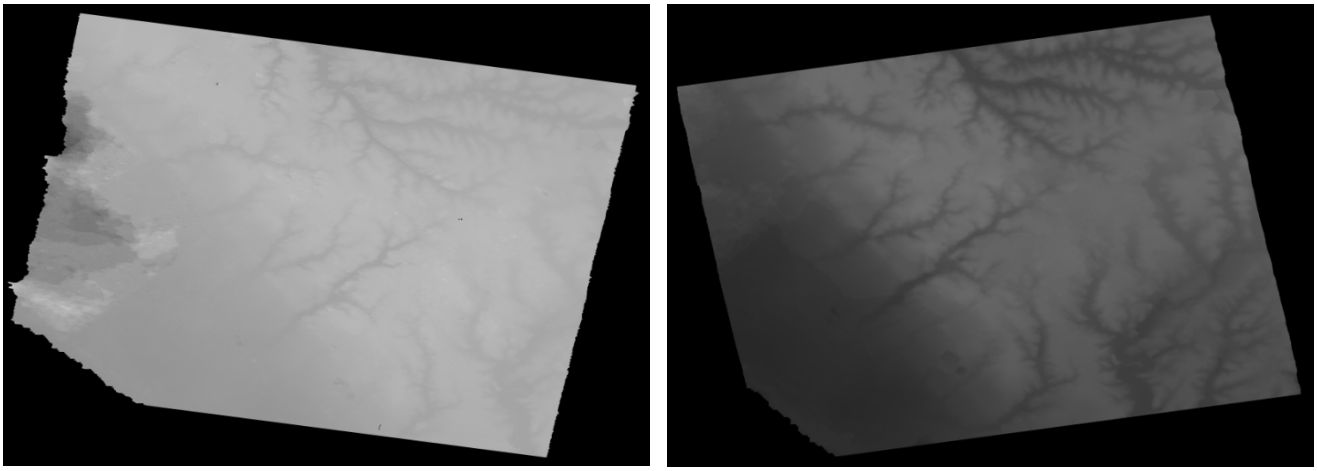

Right Descending DEM
Off-nadir = 33.93°; B_n = 220 m; H_a = 33 m
Posting = 2.5 m; Abs Err = 11.88 m; Rel Err = 8.17 m

Right Ascending DEM
Off-nadir = 30.85°; B_n = 1412 m; H_a = 4.6 m
Posting = 2.5 m; Abs Err = 10.85 m; Rel Err = 8.65 m

Fig. 4.17 – DEM generated from CSK pair 3-4 (left) and CSK pair 7-8 (right).

In Fig. 4.18 the height *precision* maps are shown, computed according to equations 4.6 and 4.7.

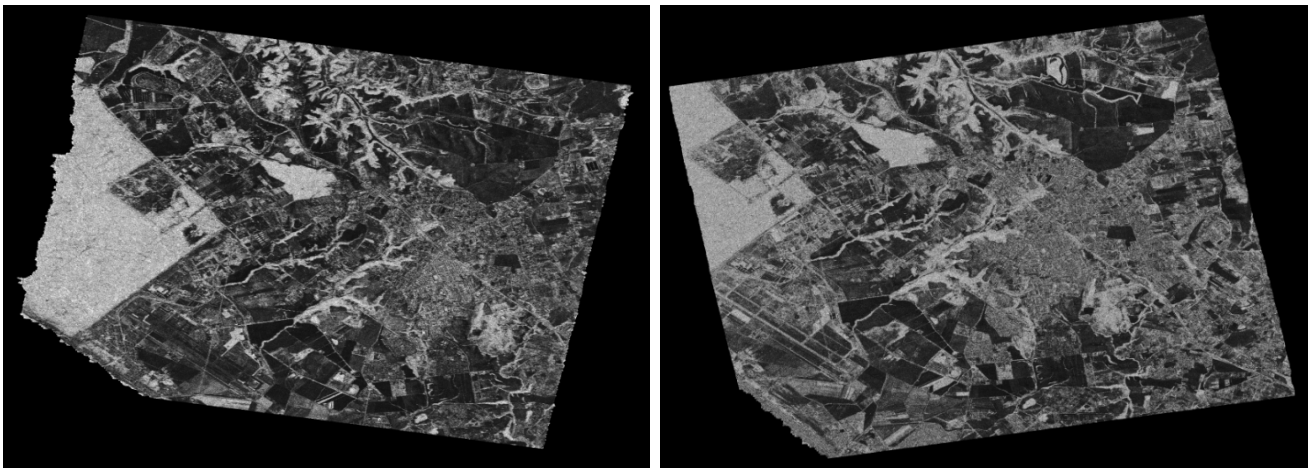

Fig. 4.18 – Height precision maps for DEM generated from CSK pair 3-4 (left) and CSK pair 7-8 (right).

In Fig. 4.19 the combined DEM is proposed, deriving from the merging of the ascending and descending DEMs. The merged DEM quality was assessed and compared with input DEMs. The absolute vertical error is equal to **10.3 m** and the relative vertical error equal to **7.81 m**.
It means that the ascending and descending merging strategy based on the *height precision* principle allowed an improvement in the vertical accuracy of the merged DEM approximately equal to the **5%** respect to the higher quality input DEM, even if the topographic variability was very slight.

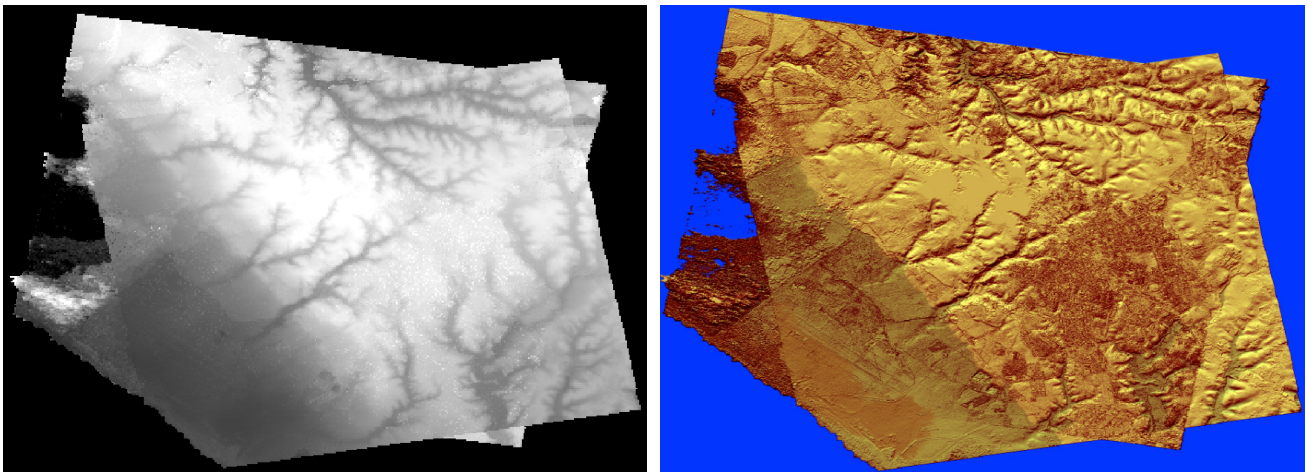

Fig. 4.19 – Ascending/Descending combined DEM.

4.4.2. Wavelet Fusion

If the refraction index profiles along the atmosphere are different for the generation of the two CSK images used as interferometric pair, the result is an alteration of the interferometric phase (atmospheric mask).

If the variation of the refraction index profiles between the two CSK acquisitions represents a *bias* which is constant for every pixel, it is easy to be removed. If different variations for different pixels arise, the result will consist in changed phase information and then changed relative heights among pixels.

The results presented in this paragraph derive from a quantitative evaluation of the advantages which can be achieved through a wavelet-based fusion between a high accuracy DEM generated from CSK interferometric pairs, and a low accuracy DEM deriving from SRTM mission, in order to mitigate the atmospheric disturbances at low frequencies due to the repeat-pass interferometry. The technique is based on the injection of the low spatial frequencies of the low accuracy DEM, preserving the high spatial frequencies and details information of the DEM generated from CSK.

This technique is very useful to remove the *bias* introduced from the atmosphere in those cases when GCP for calibration purposes are not available during processing.

In Fig. 4.20 the low accuracy SRTM DEM and the high accuracy CSK DEM are represented, respectively on the left and right side. In particular, the low accuracy SRTM DEM is a DTED-1 re-sampled with a posting of 2 m, with an absolute vertical accuracy equal to **30 m**, while the high accuracy CSK DEM was generated without using calibration GCP during processing, with a posting of 2 m and an absolute vertical accuracy equal to **9.1 m**.

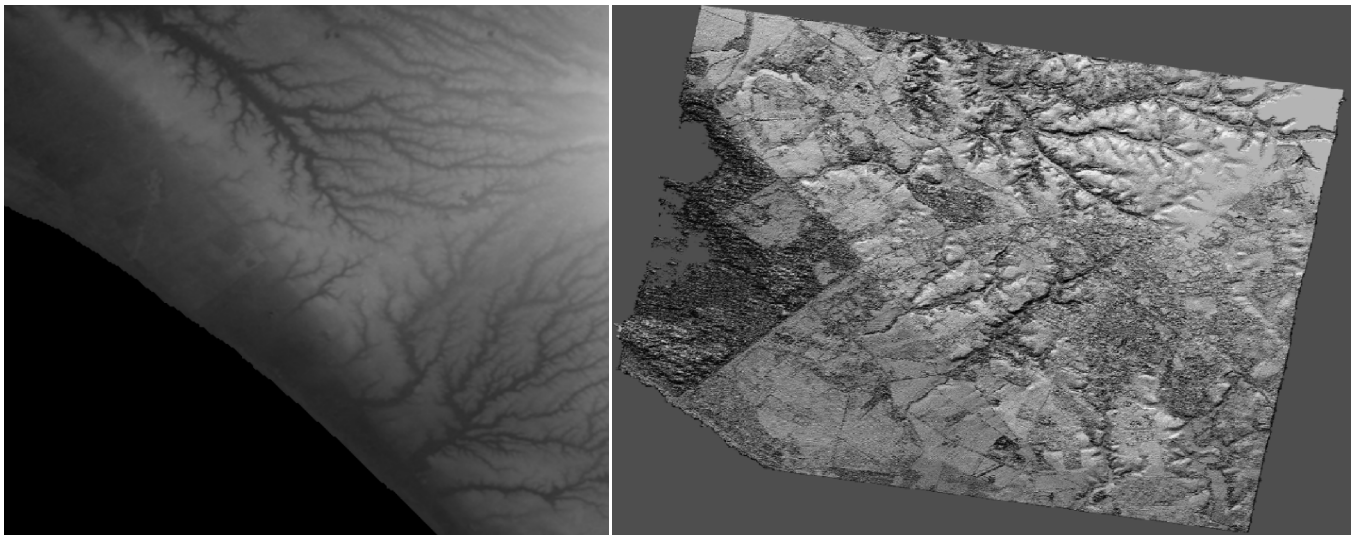

SRTM DTED-1 re-sampled with posting of 2 m
Absolute vertical accuracy of 30 m.

CSK DEM
Posting of 2 m; absolute vertical accuracy of 9.1 m.

Fig. 4.20 – Low accuracy SRTM DEM (left) and high accuracy CSK DEM (right).

Four decomposition levels were chosen during the wavelet-based fusion. In Fig. 4.21 the DEM obtained from the wavelet-based fusion process of the low and the high accuracy DEM in Fig. 4.20 is shown.

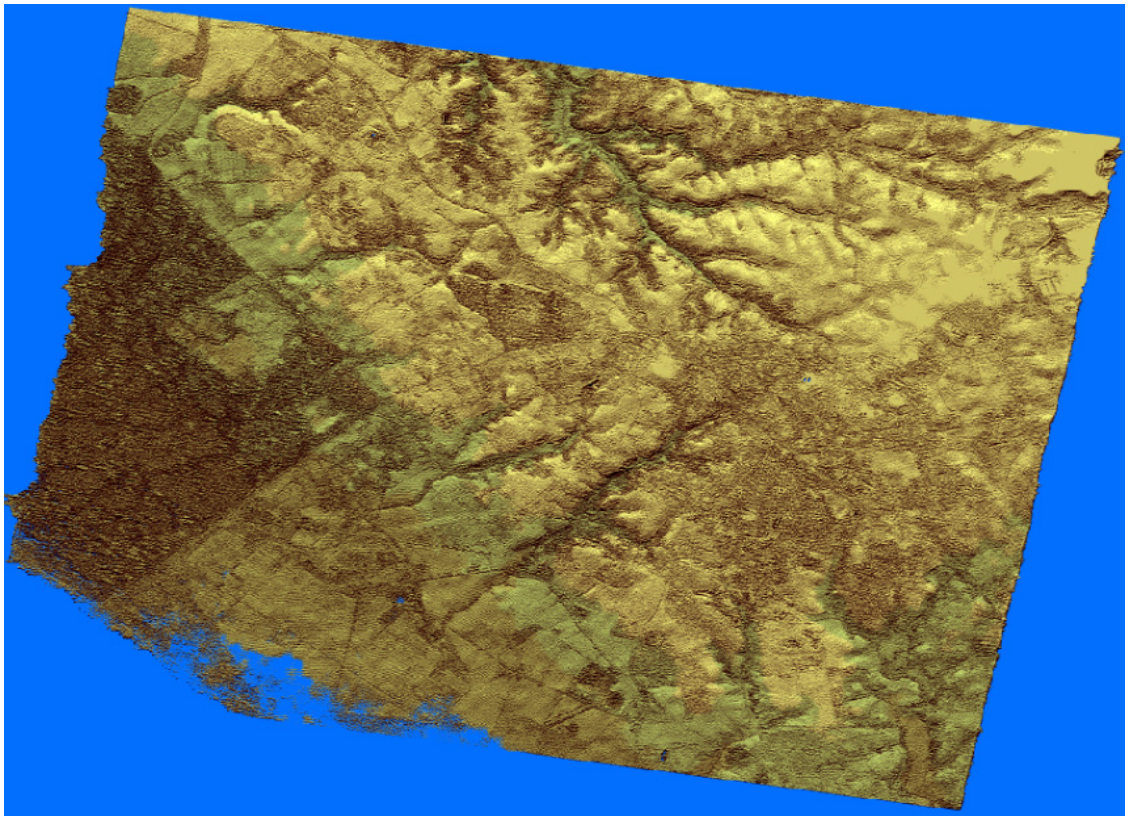

Fig. 4.21 – DEM generated through a wavelet fusion of a low and a high accuracy DEM.

The absolute vertical accuracy which was estimated for the fused DEM is equal to **7.08** m, corresponding to an improvement of the **20%** respect to the input DEM generated from CSK. The improvement in the absolute accuracy is a consequence of a *bias* introduced by the atmosphere.

4.5. Critical Analysis

SAR interferometry allows to obtain high-resolution topographic measurements, but the achievable performances mainly depend on the acquisition parameters (e.g. incidence angle, spatial and temporal baselines), ancillary data accuracies (e.g. orbital data, external DEM/GCPs for calibration), the observed scene (e.g. sea/ice, vegetated terrain, urban areas) and the error induced by data processing (e.g. co-registration, phase unwrapping). In general, interferometric DEMs are affected by two kinds of errors: systematic and random. Systematic errors can be reduced after a calibration process, whose results strongly depend on the quality of the reference data. In this paragraph all the critical issues will be deepened and analyzed.

4.5.1. Orbital Considerations

The previously presented results, based on an interferometric processing, were achieved from CSK one-day temporally decorrelated interferometric acquisitions, with CSK in Tandem-like orbital configuration (i.e. two satellites on the same orbital plane with a relative phasing of 67.5°). Due to one-day temporal decorrelation, coherence values may be low in local regions, mainly in vegetated areas where quickly changing backscattering conditions give a low intrinsic decorrelation time, or because of different atmospheric conditions (i.e. refraction index) at the times of the interferometric acquisitions, which imply a different path followed by the two signals. This first issue can be addressed, with a consequent improvement of the coherence and the interferometric quality, by an orbital configuration change aimed at reducing the temporal decorrelation between the interferometric acquisitions, even if at the expenses of CSK revisit time performances.

Several interferometric Tandem configurations are possible: two satellites can orbit on the same orbital plane with a separation only in anomaly or they can orbit separated in phase and on two different orbital planes slightly different in the longitude of the ascending node (i.e. LTAN), such to obtain a distance between ground tracks adjusted to the interferometric baseline. The second configuration is preferable because it allows a higher along-track separation between the satellites, the temporal decorrelation being equal, with lower impact risks and less demanding satellites control strategy. In general, the relative position between the two satellites in Tandem configuration

depends on the required interferometric baseline, the time decorrelation between interferometric acquisitions and the safe distance to avoid collision risks.

Considering CSK Sun-Synchronous orbit (SSO) at 619.6 km and SAR access capabilities only through electronic beam steering between on-ground incidence angle from 25° to 50°, the interferometric baseline is in the range from 100 m to 3.500 m with an accuracy around 20%. Furthermore, it implies an accuracy requirement in controlling the relative distance between the two satellites ground tracks (i.e. the projection of the interferometric baseline on the ground), which shall be maintained during an interferometric mission within the same order of magnitude and accuracy of the interferometric baseline.

For the first solution, i.e. in-plane Tandem configuration, Tab. 4.7 shows the results of a trade-off analysis among decorrelation time, along-track separation and interferometric baseline.

Temporal Decorrelation (sec)	60	50	40	30	20	15	10	3
Along-track separation (km)	450	377	302	226	151	113	75	23
Ground tracks shift / interferometric baseline, @equator (km)	27.8	23.2	18.6	13.9	9.3	7.0	4.6	1.4

Tab. 4.7 – Trade-off Analysis for CSK in-plane Tandem Configuration.

From Tab. 4.7 it is possible to understand that in order to do not exceed the convenient interferometric baseline values, a maximum in-plane phasing of 3 seconds shall be chosen, which on the other hand sets the two satellites very close each other, at an along-track distance of only 23 km, increasing the collision risk. Safer configurations do not allow to achieve baseline values useful for interferometric applications.

These considerations represent the reason why different orbital plane have to be chosen for Tandem configuration, by changing the ascending node according to equation 4.8.

$$\Delta\Omega_{tandem} = \Omega_{CSK\#n} - \Omega_{CSK\#m} = \left(\frac{2\pi}{86164} - \dot{\Omega}_{CSK\#m}\right)\Delta t_{tandem} \tag{4.8}$$

Where Ω represents the right ascension of the orbital plane and Δt represents the decorrelation time due to the phasing of the two satellites.

In Tab. 4.8 the results of a trade-off analysis are summarized among temporal decorrelation, along-track separation, node difference and the Delta-V cost required to perform a cross-track maneuver to "instantaneously" change the node of an angle equal to the node difference starting from a nominal configuration (i.e. four satellites orbiting on the same orbital plane and equally separated in

anomaly), in order to choose the best Tandem orbital configuration in terms of fuel budget saving, interferometric products quality and system safety.

Temporal Decorrelation (sec)	60	50	40	30	20	15	10	3
Along-track separation (km)	450	377	302	226	151	113	75	23
Node difference (deg)	0.25	0.21	0.17	0.13	0.08	0.06	0.04	0.01
Delta-V cost (m/s)	32.9	27.4	22.0	16.5	11.0	8.2	5.5	1.6

Tab. 4.8 – Trade-off Analysis for CSK Tandem Orbital Configuration.

In Tab. 4.8, the highlighted column shows the best trade-off choice among parameters, representing a Tandem orbital configuration with two satellites separated of 1.22° in true anomalies, corresponding to an along-track separation equal to 151 km, and in different orbital planes with a separation of 0.08° in RAANs. This orbital condition guarantees a temporal decorrelation between interferometric acquisitions equal to 20 seconds, allowing a sensitive improvement in coherence value. It is worth to be noted that increasing the along-track separation among satellites, on one hand this implies a relaxation of the constellation control requirements, on the other hand it entails an increased decorrelation time between interferometric acquisitions, with consequent implications on DEM quality and Delta-V (and propellant) required to perform all the necessary orbital maneuvers starting from the nominal orbital configuration.

In order to reduce the costs related to a change of orbital plane it is possible to act on the node rate $\dot{\Omega}$. For instance, accepting a transition time of 30 days, it is possible to achieve a decorrelation time of 60 seconds with a Delta-V cost reduced to 18 m/s.

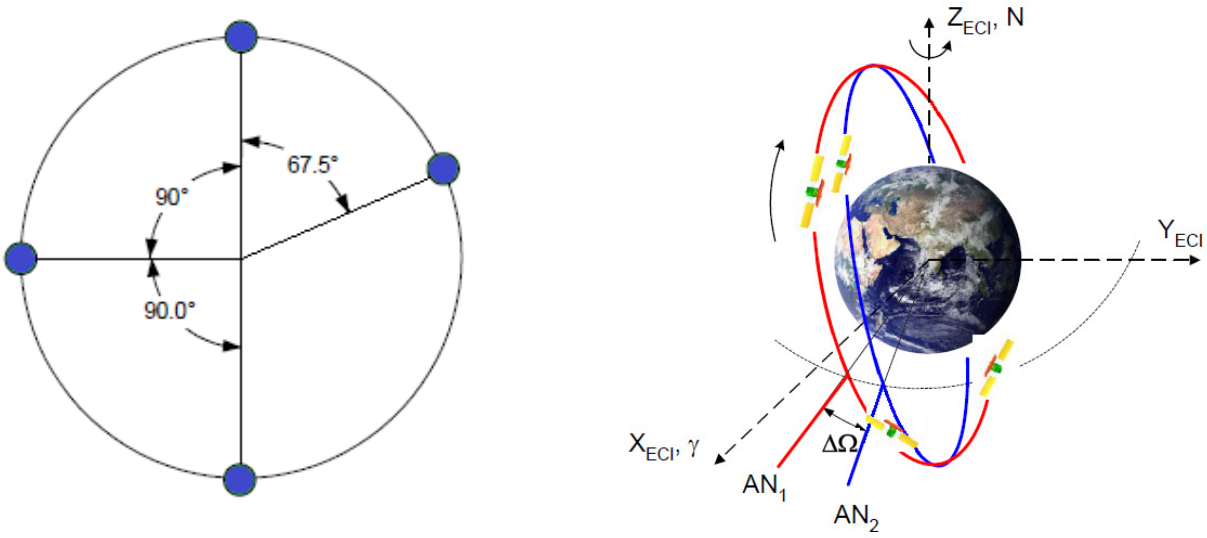

Fig. 4.22 – CSK Orbital Configurations, left: Tandem-like, right: Tandem.

Therefore, the strategy to achieve a Tandem orbital configuration envisages first the satellite in-plane replacement, and then the out-of-plane maneuver consisting in consequent phases such as "braking" phase, "coasting" phase and "boosting" phase, with a series of maneuvers in approximately four days, during which imaging is not possible.

During the interferometric mission, the along-track separation has to be dynamically tuned in order to achieve the desired baseline value for each specific application. The baseline value has to be strictly controlled, because it is very sensitive to along-track adjustments: a variation of only 2 seconds in along-track separation entails a change of 1 km in the interferometric baseline.

4.5.2. Baseline Calibration

A baseline error can be introduced by the inaccuracy in orbit estimation. The error in the baseline estimation can be decomposed in an orthonormal reference system $(\hat{v}, \hat{n}, \hat{c})$, where $\hat{v}$ is the along-track direction, $\hat{c}$ is the cross-track direction and $\hat{n}$ the versor along the radial direction. The induced error on the DEM due to inaccurate baseline estimation depends on the particular interferometric configuration in terms of baseline length, angle between baseline and look direction, angle between baseline and master along track direction ($\pi/2$ for parallel orbits). The baseline inaccuracies impact on the across-track position and target elevation. It is possible to show that a small error on the baseline components B_n and $B_{\parallel}$ with respect to line of sight causes a large error on the target position and elevation due to the high sensitivity.

The baseline error is a systematic error, differently from phase errors, thus it can be minimized through a geometric calibration based on the availability of a low resolution DEM or GCPs over the image. The calibration processing aims at minimizing the difference between the measured interferometric phase and the phase calculated as in equation 4.9, where r is the slant range distance, ϑ is the look angle, B is the baseline length, B_{nad} the baseline component along nadir, B_{cross} the baseline component in the direction perpendicular to the nadir and the SAR velocity.

$$\phi = \frac{4\pi}{\lambda}\left[\sqrt{r^2 + B^2 - 2r(B_{nad}cos\vartheta + B_{cross}sin\vartheta)} - r\right] \tag{4.9}$$

The result mainly depends on the quality of the reference DEM and the interferometric phase coherence. In particular, a bias on the reference DEM causes a bias on the estimated parameters, while phase noise and relative errors in the reference DEM cause uncertainty on the estimated parameters.

It is possible to demonstrate that only the phase constants of the interferometric phase, namely B_n and $B_\parallel$, are mutually independent parameters having a significant effect on the target determination, and they can be used to determine the residual error after the calibration processing.

An error on the baseline components and the phase constant cause a systematic error on the measured elevation and on the horizontal location.

Assuming B_n and $B_\parallel$ mutually independent phase constants, the covariance matrix C gives the power of each residual error after the calibration process, due to phase noise and relative reference DEM accuracy, equation 4.10 where h is the target height.

$$C = \begin{bmatrix} \sigma_\phi^2 & - & - \\ - & \sigma_{B_n}^2 & - \\ - & - & \sigma_{B_\parallel}^2 \end{bmatrix} = \begin{bmatrix} \sum \frac{1}{\sigma_h^2} \left|\frac{\partial h}{\partial \phi}\right|^2 & \sum \frac{1}{\sigma_h^2} \frac{\partial h}{\partial \phi} \frac{\partial h}{\partial B_n} & \sum \frac{1}{\sigma_h^2} \frac{\partial h}{\partial \phi} \frac{\partial h}{\partial B_\parallel} \\ \sum \frac{1}{\sigma_h^2} \frac{\partial h}{\partial \phi} \frac{\partial h}{\partial B_\parallel} & \sum \frac{1}{\sigma_h^2} \left|\frac{\partial h}{\partial B_n}\right|^2 & \sum \frac{1}{\sigma_h^2} \frac{\partial h}{\partial \phi} \frac{\partial h}{\partial B_\parallel} \\ \sum \frac{1}{\sigma_h^2} \frac{\partial h}{\partial \phi} \frac{\partial h}{\partial B_\parallel} & \sum \frac{1}{\sigma_h^2} \frac{\partial h}{\partial \phi} \frac{\partial h}{\partial B_n} & \sum \frac{1}{\sigma_h^2} \left|\frac{\partial h}{\partial B_\parallel}\right|^2 \end{bmatrix}^{-1} \tag{4.10}$$

The error on the reconstructed DEM does not depend on the baseline length. In particular, an horizontal or vertical offset on the reference DEM distorts the range distance, and this distortion causes a mismatch between the true and the estimated position of the control point on the SAR image. The critical misplacement depends on the rate of variation of the observed topography, but it shall be smaller than the reference DEM resolution.

The quality of InSAR products are significantly affected by the accuracy of the baseline estimation. Further methods for baseline calibration and estimation techniques are proposed in (Costantini, et al., 2003) and in (Zhang, et al., 2009).

4.5.3. Phase Errors

The phase error can be decomposed in a contribution due to the atmospheric phase delay, one due to phase noise, one due to phase unwrapping errors and one to layover and shadow effects.

Larger baselines allow a more precise reconstruction of the three-dimensional target position, but this increases the signal decorrelation and makes phase unwrapping not feasible.

Each contribution to phase errors will be analyzed in the following paragraphs, from which some open issues to repeat-pass interferometry will arise, such as atmospheric disturbances, scene decorrelation and the calibration of the interferometer.

4.5.3.1. Atmospheric Phase Delay

The atmospheric phase delay error source is dominant respect to the others. As the refraction index changes according to the atmospheric conditions, the length of the radiation path travelled during the two interferometric acquisitions at different times, which depends on the integral of the refraction index over the path, can vary by some centimeters, inducing phase delay up to 4 cycles. In particular, the relation between the radiation length delay due to atmosphere, δ_{atmo}, and the induced phase delay, ϕ, can be quantified through the equation 4.11.

$$\delta_{atmo} = \frac{\lambda\phi}{4\pi} \tag{4.11}$$

The different phase delays are erroneously interpreted as due to the topography. One phase cycle, corresponding to a delay in the order of 3 cm, causes an error in the measured height in the order of the height of ambiguity.

Atmospheric phase delay is not a systematic error and cannot be removed with a calibration procedure. In fact, since the length of the radiation path is proportional to the real part of the refraction index, then the propagation delay for each pixel can be considered as the sum of a medium delay due to refraction profile averaged on the scene and a variable delay which depends on the spatial fluctuations of the refraction profile on a scale larger than a pixel and lower then the swath. Different phase variations for different pixels, due to different refraction index profiles, do not produce a bias but do modify the phase information and then the relative heights among pixels, strongly affecting DEM accuracy. It is possible to reduce the impact of the atmospheric artifact by using large baselines, with other drawbacks. The only way to address the atmospheric issue is to reduce the temporal baseline between the two interferometric acquisitions to few seconds (e.g. CSK Tandem configuration, SRTM and TanDEM-X missions), because in this case the atmospheric phase delay is negligible.

In (M. Albani, 1998) a numerical simulation was carried out to assess the errors induced by changes of the tropospheric refractive structure in the heights derived through repeat-pass InSAR with ERS data, using about 7000 radio-surveys. The statistics highlighted higher atmospheric delays during hotter months, and a maximum standard deviation during autumn, while wintry period seems to represent the more stable situation, with minimum values of both atmospheric delays and standard deviation, because of the minimum quantity of vapor for low temperatures. According to the simulation performed, when the variation of the refraction index between the interferometric acquisitions is uniform, there are effects on the DEM accuracy only if the surface is not flat: in fact,

in correspondence to reliefs, the thickness of the troposphere varies causing variations of the phase differences related to pixels located at different heights.

To summarize, the atmospheric error can be decomposed in a ionospheric path delay and a tropospheric path delay.

The ionosphere, located at a height of approximately 50 km – 1500 km, is characterized by the existence of free electrons and ions that define the refractive index in that area. The Total Electron Content (TEC) specify the number of free electrons in a column of 1 m^2 along the signal path. TEC Units (TECU) are 1016 electrons/m^2. The number of free electrons interacting with the signal causes a path delay depending by the signal frequency *f*. In accordance with (Jehle, et al., 2004), the path delay through the ionosphere can be evaluated by equation 4.12:

$$\Delta\Phi_{iono} = 2K\frac{TEC}{f^2 cos\vartheta} \tag{4.12}$$

where *K* is a refractive constant and ϑ the off-nadir angle.

The tropospheric path delay is composed by an hydrostatic, a wet and a liquid component. The hydrostatic component is the standard atmosphere, the wet component takes into account the water vapor, the liquid component considers the liquid water content and can be neglected for SAR applications. The hydrostatic and the wet components can be modeled as in equation 4.13:

$$\begin{gathered}\Psi_{hyd} = 10^{-6}k_1\frac{R_d}{g_m}P_0 \\ \Psi_{wet} = 10^{-6}\left(\frac{(k_2'T_m + k_3)R_d e_0}{T_0(g_m(\varepsilon+1) - \beta R_d)}\right)\cdot\left(1 - \frac{\beta h}{T_0}\right)^{\frac{(\varepsilon+1)g_m}{R_d\beta}-1}\end{gathered} \tag{4.13}$$

where g_m is the acceleration due to local gravity, $k_1 = 77.6\left[\frac{K}{mbar}\right]$, $k_2' = 23.3\left[\frac{K}{mbar}\right]$ and $k_3 = 3.75\cdot 10^5\left[\frac{K^2}{mbar}\right]$ are refractive constants, $R_d = 287\left[\frac{J}{K\cdot Kg}\right]$ is the ideal gas constant, $\beta = 6.5\left[\frac{K}{Km}\right]$ is the temperature lapse rate, T_0 $[K]$ is the temperature, e_0 $[hPa]$ is the water vapor pressure above sea level, T_m $[K]$ is the mean temperature of water vapor, h is the target height and ε is the average water vapor decrease.

The a ionospheric path delay consists both in variations of the total electron content along the path, which depends on the time of day and influences the whole scene homogeneously, and in traveling ionospheric disturbances, which cause localized artifacts. The tropospheric path delay is the dominant dry part, it is small but it has highly variable wet part which is caused by the strong temporal and spatial variability of the water vapor concentration. The tropospheric water vapor is a

very localized, heterogeneous effect, which represents the most limiting factor for SAR interferometry.

4.5.3.2. Phase Noise

The phase noise is due to several contributions, such as focusing, SNR, coregistration errors, baseline decorrelation, azimuth spectral decorrelation, time decorrelation, and so on.

Increasing the coherence value γ and the number of look N_L, the phase noise will decrease. However, a lower bound of the phase noise is defined by the Cramér-Rao bound in equation 4.14, as stated by Rodriguez and Martin, (E. Rodriguez, 1992).

$$\sigma_{\phi}^{2} = \frac{1}{2N_L}\frac{1-\gamma^2}{\gamma^2} \tag{4.14}$$

The theoretical probability density function of the interferometric phase, under the assumption of circular Gaussian signals, is given by equation 4.15, (Lee, et al., 1994).

$$p_{\phi}(\phi, NL, \gamma) = \frac{\Gamma\left(NL + {}^{1}/_{2}\right)(1-\gamma^2)^{\mathrm{NL}}\beta}{2\sqrt{\pi}\Gamma(NL)(1-\beta^2)^{NL+{}^{1}/_{2}}} + \frac{(1-\gamma^2)^{\mathrm{NL}}}{2\pi}F\left(NL; 1; {}^{1}/_{2}; \beta^2\right) \tag{4.15}$$

$$\beta = \gamma cos(\phi - \bar{\phi})$$

Where $F\left(NL; 1; {}^{1}/_{2}; \beta^2\right)$ is a Gaussian hypergeometric function.

From above equations, it is possible to observe that the phase standard deviation decreases by increasing the coherence value and by increasing the number of looks. In particular, for lower numbers of looks, the phase standard deviation decreases with coherence faster for higher coherence values; while for higher numbers of looks, the phase standard deviation decreases with coherence faster for lower coherence values.

Assuming that the contributions to the phase noise error listed above are independent, the total coherence γ is the product of the terms relative to the different kinds of decorrelation, as in equation 4.16.

$$\gamma = \prod_{i=1}^{n} \gamma_i \tag{4.16}$$

Then, from equation 4.14 it is possible to have an estimation of the phase noise.

The first contribution to the phase noise error can be added by SAR data focusing: the focusing processor should be phase preserving.

An additional contribution is given by SNR: the thermal noise decorrelation is defined as in equation 4.17, (P. Rosen, 2000).

$$\gamma_{SNR} = \frac{1}{\sqrt{1 + SNR_1^{-1}}} \frac{1}{\sqrt{1 + SNR_2^{-1}}} \tag{4.17}$$

Where SNR_1 and SNR_2 are the signal-to-noise ratios of the master and slave images.

Considering coregistration errors in azimuth and range directions, respectively *dx* and *dy*, and the ideal radar impulse response (point target) in equation 4.18:

$$I_1 = \frac{\sin(2\pi x)}{2\pi x} \frac{\sin(2\pi y)}{2\pi y} \tag{4.18}$$

in order to take into account coherence reduction caused by errors in images coregistration, it is possible to substitute $I_2(x, y) = I_1(x + dx, y + dy)$ in the equation for coherence estimation (4.19):

$$\gamma = \frac{E\{I_1 I_2^* e^{-j\phi}\}}{\sqrt{E\{|I_1|^2\} E\{|I_2|^2\}}} \tag{4.19}$$

achieving the contribution to the coherence, equation 4.16, given by errors in the coregistration, equation 4.20 and Fig. 4.23.

$$\gamma_{COR} = sinc(2\pi\, dx) \cdot sinc(2\pi\, dy) \tag{4.20}$$

A further contribution to the phase noise is given by the baseline decorrelation, (Gatelli, et al., 1994). The spectrum received from the two antennas during the interferometric acquisitions with a certain baseline are shifted due to the different look angles. The consequent decorrelation depends on the normal baseline length, the range distance *r*, the range resolution *dr* , the incidence angle θ, as in equation 4.21.

$$\gamma_B = 1 - \frac{2B_\perp dr}{\lambda r\, tan\theta} \tag{4.21}$$

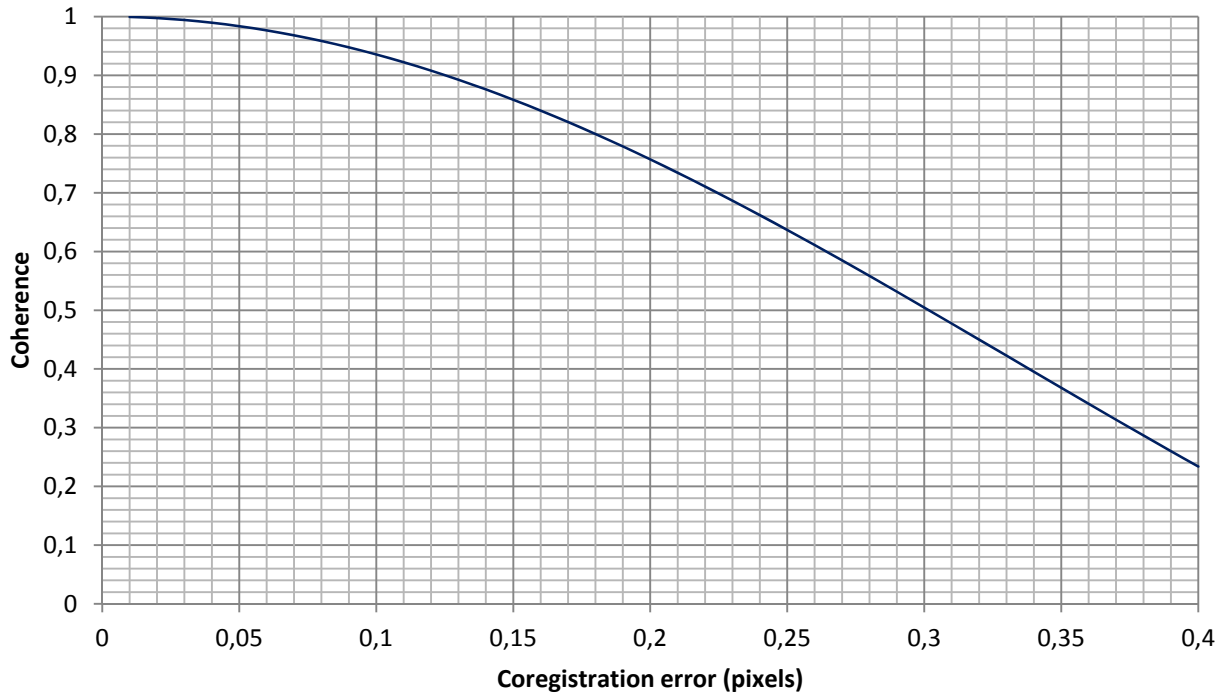

Fig. 4.23 – Contribution of the coregistration errors to the coherence value for a point target.

Fig. 4.24 shows the coherence as a function of the incidence angle θ for different values of the normal baseline $B_{\perp}$, with a range resolution of 1m and a wavelength of 3.125 cm.

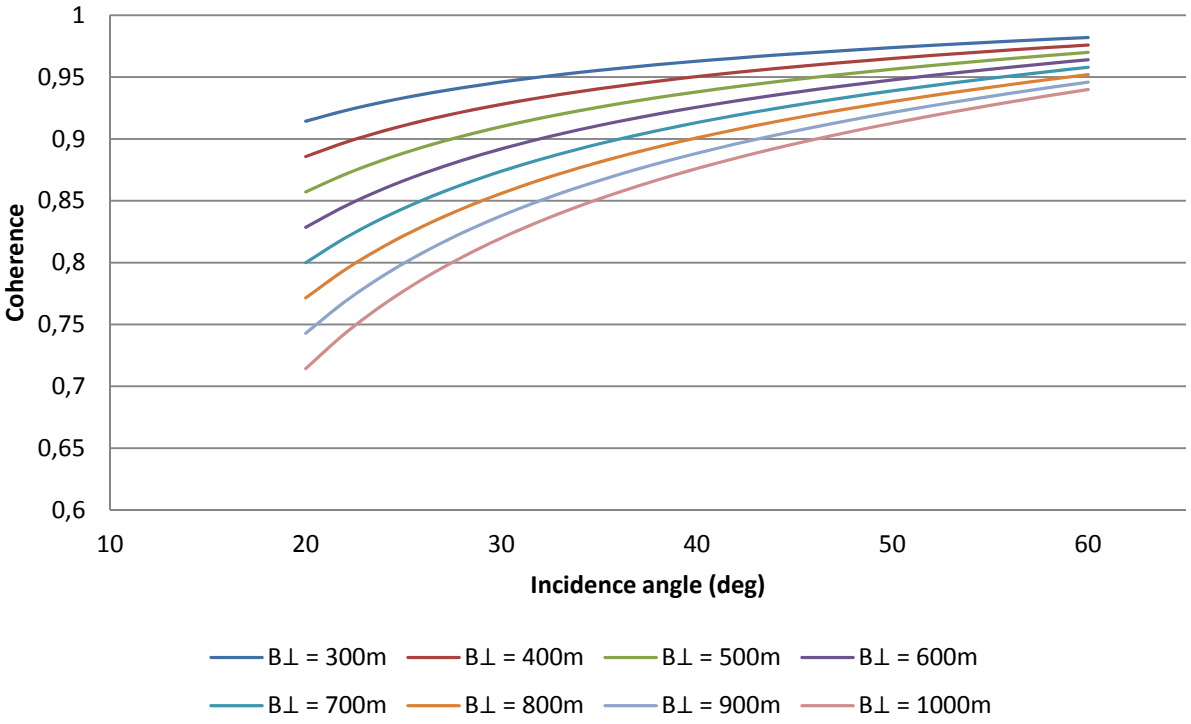

Fig. 4.24 – Contribution of the baseline decorrelation to the coherence value.

Another significant contribution to the phase noise is represented by the azimuth spectral decorrelation, which occurs when the spectral components coming from the interferometric

acquisitions along the azimuth direction are different. For Stripmap acquisition mode this is due to a difference of squint angles $\Delta\varsigma$, which causes a Doppler centroid shift in focusing process, given by equation 4.22.

$$\Delta f_{Dc} \cong \frac{2v}{\lambda}\Delta\varsigma \tag{4.22}$$

A Doppler centroid shift, in turns, yields a a spectral decorrelation quantified in equation 4.23.

$$\gamma_{\mathrm{A}} = 1 - \frac{\Delta f_{Dc}}{B_{az}} \tag{4.23}$$

Referring to Fig. 4.25, the Doppler spectral width is determined by the azimuth beam width of the SAR. Furthermore, the Doppler center frequency (i.e. Doppler centroid) is determined by attitude, antenna and Earth rotation. In particular, an azimuth pointing bias would affect the Doppler centroid shift between interferometric acquisitions and consequently the azimuth spectral decorrelation.

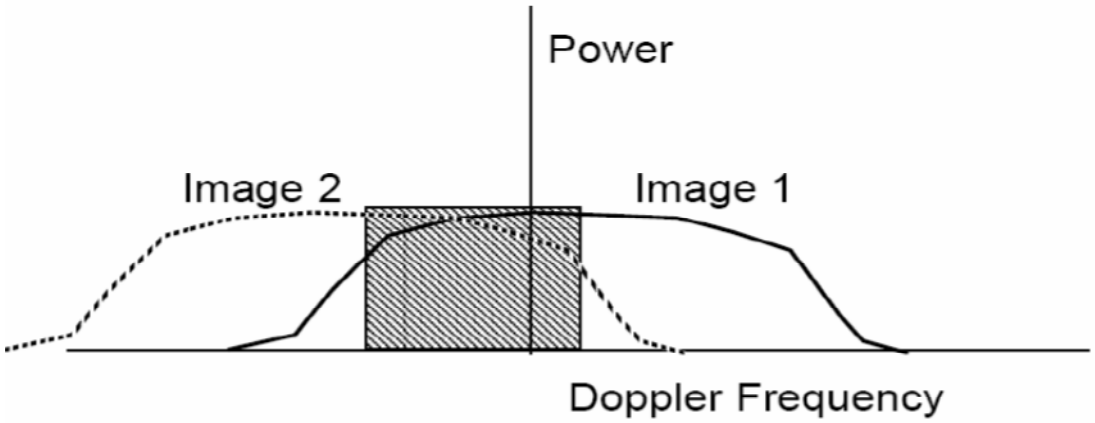

Fig. 4.25 – Non-overlapping Doppler spectral energy.

To maximize the coherence between interferometric acquisitions, it is convenient to filter out non-overlapping energy (i.e. Common Band Filtering).

In the specific case, (Porfilio, et al., 2012), interferometric pairs CSK2-CSK3 show coherence histograms affected by a bias in azimuth pointing, Fig. 4.26. In fact, the consequence of the pointing bias is that the azimuth beam irradiates targets with different angles between the interferometric acquisitions. Different angles yield radar echoes received with different Doppler frequencies. In particular, the Doppler centroids difference is in the order of 600-700 Hz for Stripmap acquisitions, compared with a focused Doppler band of 2.5 kHz, and in the order of 3 kHz for Spotlight-2 acquisitions, compared with a Doppler band acquired with a power higher than -3dB equal to 7.8 kHz (because of the azimuth steering which shall be performed, which implies a larger variation of the Doppler centroid during the acquisition), Fig. 4.27. Even with this Doppler centroids shift

amount, in actual acquisition scenarios, with PRF values in the order of 3 KHz, ambiguity is zero being the Doppler centroid at center scene in the range [-PRF/2, PRF/2]. Due to a partial spectral overlap, the phase of distributed targets can be different in the two images (speckle phase variance), while the phase of point targets is unchanged (processing at zero-Doppler).

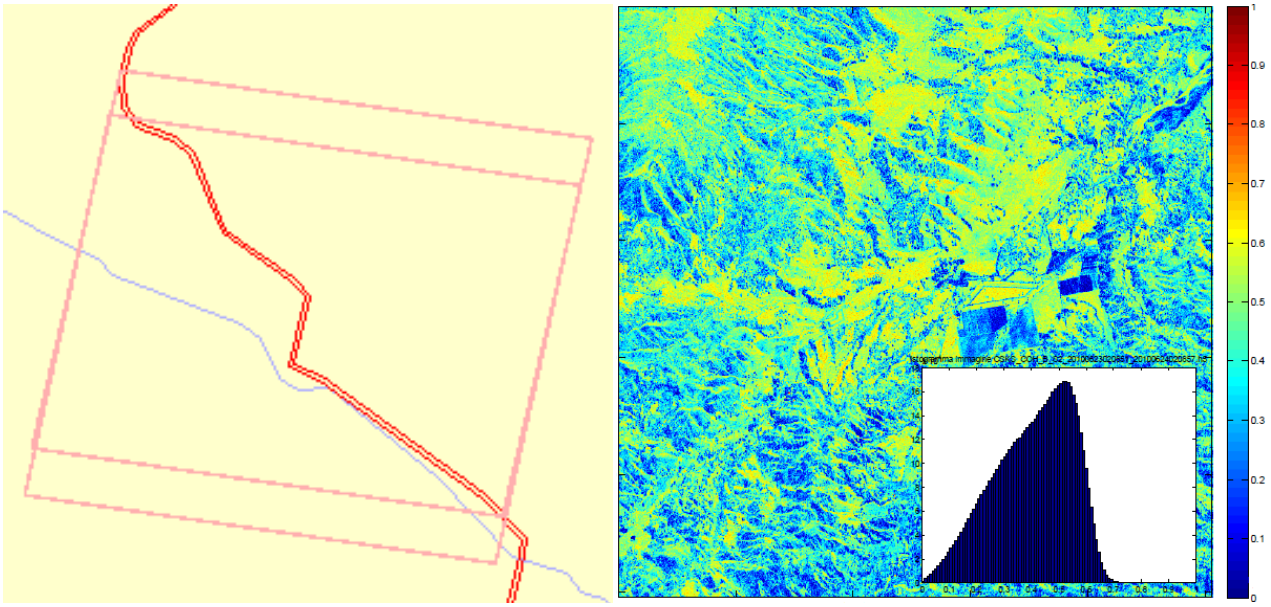

Fig. 4.26 – CSK2-CSK3 ES interferometric pair, from left: pointing bias; coherence.

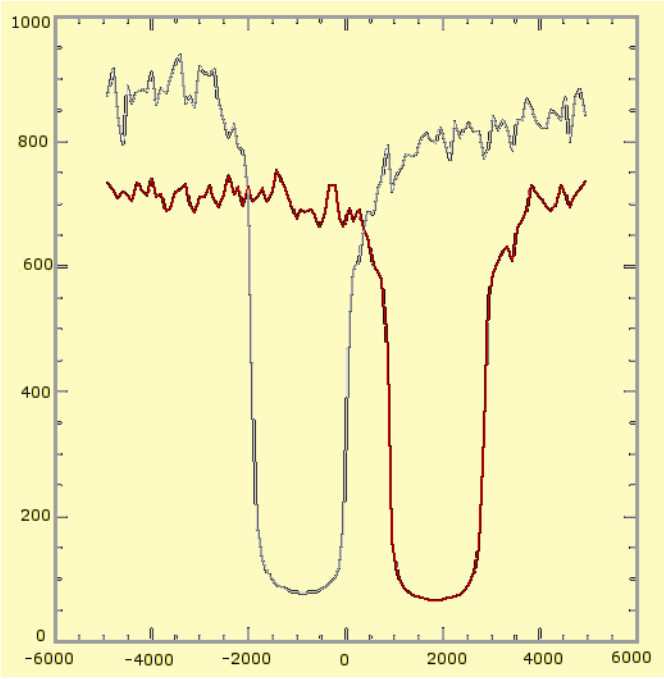

Fig. 4.27 – Azimuth spectrum from CSK2-CSK3 coregistered data.

The effect of a partial overlap of the Doppler spectra and a Doppler centroids shift between interferometric acquisitions is a drop in the coherence value. In fact, coherence is maximized when the complex versors originated by the interferogram are aligned among them and the vector sum is

constructive. Complex versors are aligned when their content conveys equal Doppler frequencies. If different spectral components are present, non-homogeneity elements are introduced in the phase evolution of master and slave signals, which make vector sum more and more destructive, decreasing coherence value.

In general, the main causes of an azimuth pointing bias have both a mechanical and electrical origin, such as:

- Assembling angles of the radar panel on the satellite;
- Deflections generated by residual mechanical bias (e.g. star-trackers assembling, gyros, etc);
- T/R modules status;
- General parameters of the electronics relevant to beam forming;
- SAR electronic fine pointing features (temperature and static residual tolerances).

Furthermore, the satellite is continuously interested by the application of the yaw-steering law, to keep the satellite attitude orthogonal to its relative velocity respect to the Earth surface. The satellite moves in a plane inclined of 97.86° over the equatorial plane, which is quite stable in an inertial reference system and experiences only an annual precession motion aimed at guaranteeing the LTAN parameter. If the satellite orbited with a yaw angle = 0°, the radar would transmit pulses orthogonally to the satellite inertial velocity. But the Earth in the meanwhile rotates around its axes, so the points of the observed scene have a velocity which is maximum at the equator and null at the poles, therefore the radar pulses would not be transmitted orthogonally to the relative velocity, causing squinted images, with a Doppler different from zero. At the equator scenes with a Doppler centroid in the order of 18kHz (Doppler ambiguity equal to 6) would be acquired. It means that if the satellite orbited with a yaw angle equal to zero, the image would not be ortoghonal to the satellite-target relative velocity and the Doppler conditions would be far from the ideal scenario of zero Doppler. So, the satellite continuously performs a yaw maneuver in order to guarantee acquisitions at zero Doppler, according to equation 4.24.

$$y_{aw} = -3.92\, cos(\omega t) \tag{4.24}$$

Where ω is the mean orbital angular rate and t is the time, which is equal to 0 at the ascending node. Considering the access region of about 600 km both in right and in left acquisition direction, the zero Doppler condition cannot be fulfilled in every point. If the yaw angle has a value such as to guarantee a Doppler centroid null at the equator for a right acquisition with the central beam, the residual Doppler excursion in the overall right access region is about 200 Hz.

Each satellite is independent and able to guarantee a repetitivity of the pointing conditions at different latitudes from an orbit to another one. Different satellites can show different azimuth pointing conditions.

In presence of partial spectral overlap, a work-around which can be implemented at processing level is represented by Common Band Filtering (CBF), whose purpose is to remove the part of the Doppler spectra of the two images which is not common, thus enhancing the coherence at the expenses of the azimuth resolution which worsens as much as the Doppler bandwidth is reduced, equation 4.25.

$$\rho_{az} = K_{Br} \cdot 0{,}886 \cdot {}^{v_{st}}/_{B_D} \tag{4.25}$$

Where K_{Br} is the broadening factor due to Hamming weighting, v_{st} is the satellite-target relative velocity, and B_D is the processed Doppler bandwidth. The results of the application of CBF to a CSK2-CSK3 Spotlight interferometric pair, (Porfilio, et al., 2012), show that by reducing the available bandwidth of both images from about 8 kHz to about 5 kHz, the azimuth resolution passed from 1 m to 1.6 m, the average coherence increased from 0.36 to 0.60 and the number of points with a coherence greater than 0.7 grew from 0.02% to 38%, Fig. 4.28. It was also verified that a further cut of the bandwidth, to better match the overlap band, yields a very small improvement of the coherence, basically resulting only in a further loss of azimuth resolution, Figg. 4.29-4.30.

Furthermore, the reduction of the spectral band has as a consequence also the loss of details in the interferometric fringes. In fact, a loss of azimuth resolution entails that the phase value of each pixel of the interferometric pair is representative of a wider area, so the phase information is more heterogeneous and noisy. The consequence is a degradation of the DEM absolute and relative vertical accuracies, which shall be compared with the improvement due to the increased coherence.

Moreover, an inter-satellite Doppler calibration can be performed in order to maximize the spectral overlap of the interferometric signals, by increasing the azimuth pointing similarity among satellites. The activity which shall be performed for an inter-satellite Doppler calibration consists in:

- Characterize the pointing behavior of each satellite along the entire orbit and in every acquisition condition;
- Identify a residual Doppler model;
- Translate the residual Doppler model in corrective attitude maneuvers (mainly pitch maneuvers);
- Verify that these maneuvers allow the mitigation of the phenomenon.

The previous tasks need a significant amount of images (i.e. several hundreds) to be performed, both for a full characterization of the current pointing behavior of each satellite, and for a complete verification after having implemented the corrective actions. Since each acquisition configuration

(e.g. Sensor Modes, Beam, Polarization, Look Side, Orbit Direction, etc) can show different pointing characteristics, it would be necessary at least one image for each one of the following combinations, even if this scenario can be conveniently simplified: four satellites, two look sides (i.e. left and right), about 140 different beams, four polarizations, several acquisitions during the orbital period.

Furthermore, even after a calibration activity, considering the margins of 0.01° on the beam-forming accuracy, a residual Doppler misalignment of about 150 Hz for Stripmap acquisitions and about 500 Hz for Spotlight-2 acquisitions may remain among satellites.

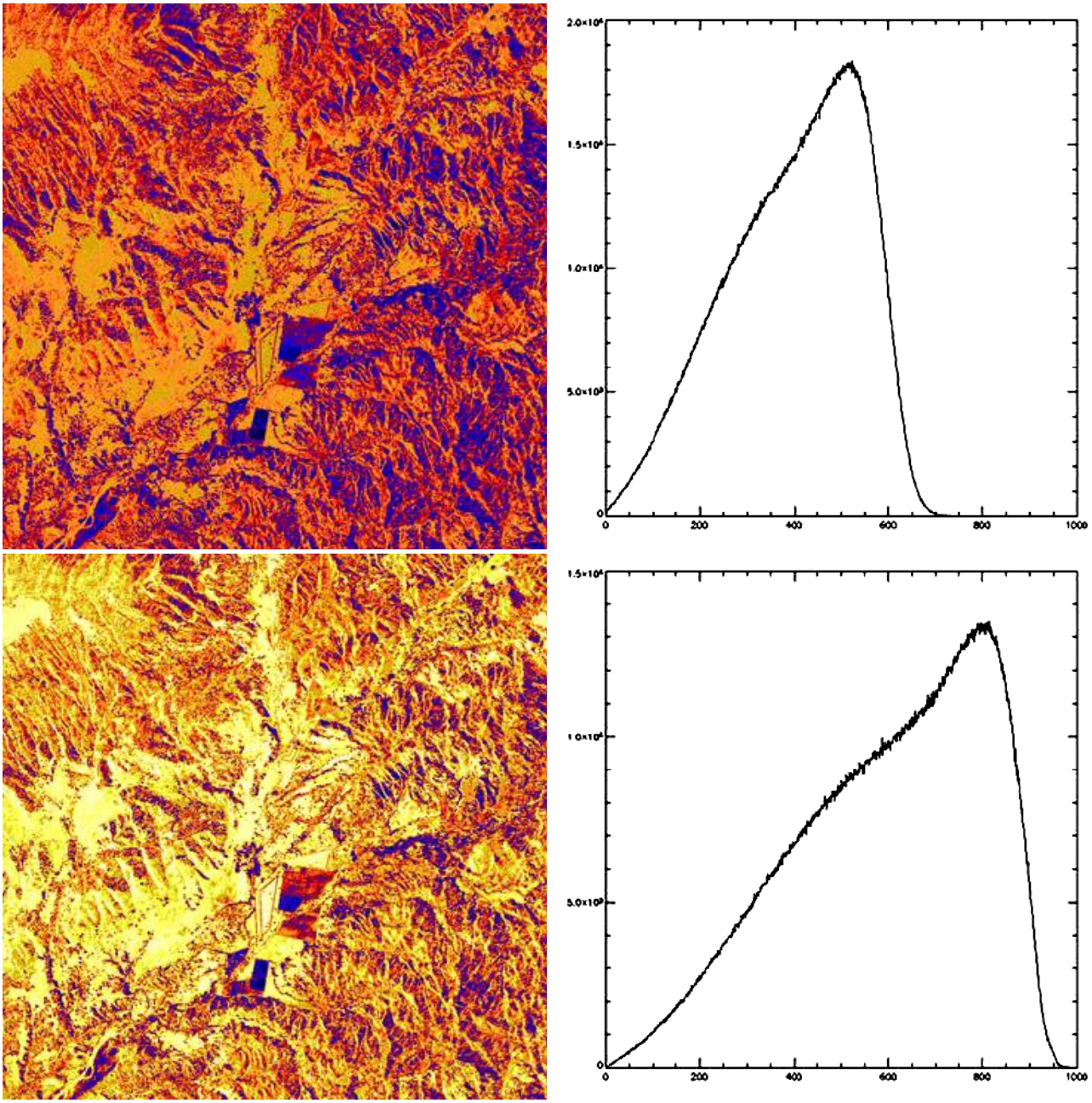

Fig. 4.28 – Top: coherence map (left) and histogram (right) for a Spotlight-2 interferometric pair with a Doppler centroids shift of 3 kHz over 7.8 kHz of Doppler band . Down: coherence map (left) and histogram (right) after having applied CBF, preserving 4.8 kHz of common Doppler band.

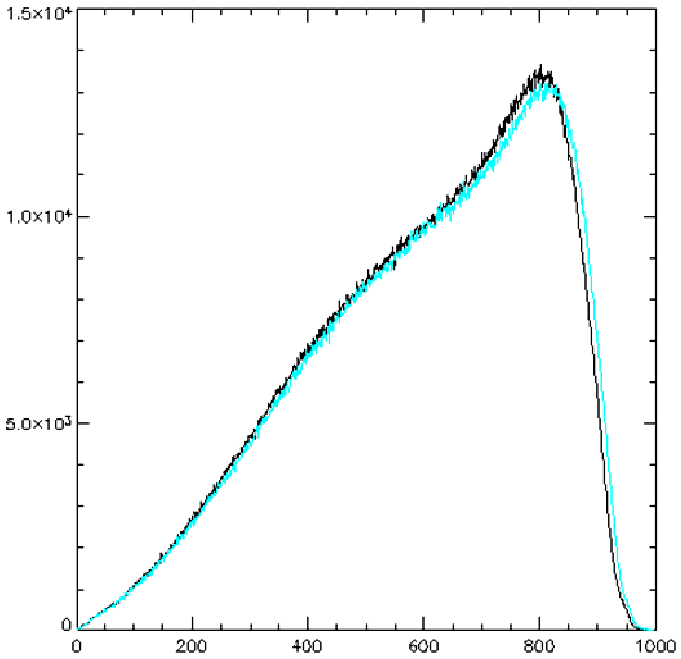

Fig. 4.29 – Coherence histogram with CBF preserving a common Doppler band of 4.8 kHz (black) and preserving a common Doppler band of 3.5 kHz (cyan).

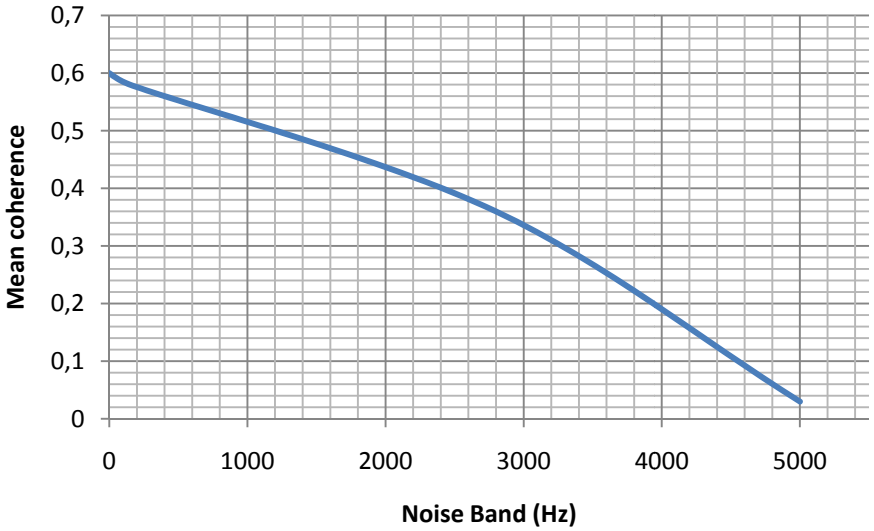

Fig. 4.30 – Mean coherence as a function of the noise band over a Doppler full band of 5 kHz.

Finally, an additional contribution to phase noise is given by temporal decorrelation, which depends on the observed scene because different scenes have different decorrelation times. In particular, in (Zebker, et al., 1994) temporal correlation is expressed as a function of the *rms* motion of the scatterers, as in equation 4.26.

$$\gamma_T = e^{-\frac{1}{2}\left(\frac{4\pi}{\lambda}\right)^2\left(dx^2\sin^2(\theta)+dy^2\cos^2(\theta)\right)} \tag{4.26}$$

where *dx* and *dy* represent the *rms* motion respectively in the cross-track and vertical directions.

Temporal decorrelation, which is dependent on time between the first and the second acquisition, is due to a change of scattering within a resolution cell or electrical properties, and can be caused by vegetation, soil moisture, wind effects, snow fall, farming activities, etc.

4.5.3.3. Phase Unwrapping Errors

Phase unwrapping can induce errors of integer multiples of 2π on the phase. However, this error should be concentrated on a small number of pixels. The probability of such a kind of error increases with the density of the interferogram fringes and with the decorrelation phase noise, which in turns are related to pixel spacing and baseline length.

Considering the slant range resolution *dr*, the number of looks in range NL_r, the slant range *r*, the incidence angle θ and the local slope *a*, the relation between fringe frequency N_f and the baseline length is given by equation 4.27.

$$B_{\perp} \leq \frac{\lambda r}{2\, dr\, NL_r} N_f sin\theta \frac{sin\,(\theta - \alpha)}{sin\alpha} \tag{4.27}$$

In any case, as already analyzed, the baseline value should be lower than the critic value at which the radar signals completely decorrelate, equation 4.28.

$$B_{\perp} \leq \frac{\lambda r}{dr\, NL_r} \tan\,(\theta - \alpha) \tag{4.28}$$

Case by case, it is necessary to perform a simulation to select a suitable baseline in order to make phase unwrapping feasible for all the terrain slopes involved in the area of interest.

At a certain fringe frequency and coherence value, if the effective number of looks is increased, the phase unwrapping error and thus the phase noise decrease. Increasing the fringe frequency, the phase noise has to be reduced in order to make phase unwrapping feasible, so it is necessary to increase the effective number of looks. For each value of coherence and fringe frequency, there is a minimum value of effective number of looks necessary to maintain the phase unwrapping error below a certain threshold able to make phase unwrapping feasible (e.g. 1%). In any case, for fringe frequencies too high, the phase unwrapping process can fail even for high values of the effective number of looks.

4.5.3.4. Layover and Shadow

The phase noise is strongly affected also by shadow and layover effects, which are intrinsically related to SAR acquisition geometry. Actually shadow regions, where the signal is almost absent,

are characterized by low SNR, while layover is characterized by very strong return, but the phase information is completely loss because of the collapse of multiple scatterers at different positions. Therefore, data on these regions are not reliable and shall be masked out, by applying some restriction to the maximum resolvable slope and the look angle for instance, or shall be completed by other complementary data acquired through different looking geometries, as shown in paragraph 4.4.1.

4.5.4. Timing Accuracy

Two kind of timing errors have to be considered and can affect the horizontal target location and height determination accuracies: a datation error, which causes an along-track timing error and can be stated in terms of the effective azimuth location error, and an electronic phase delay, which affects the slant range distance of the observed target.

In particular, a bias or a drift of the onboard clock causes an erroneous association between image lines and acquisition time. Considering a datation error Δt_{az} and a velocity module v, the along-track position error is given by equation 4.29.

$$\sigma_y^2 = (\Delta t_{az} \cdot v)^2 \tag{4.29}$$

On the other hand, an electronic phase delay $\sigma_{\Delta t_0}$ has an impact on the across-track position and on the height determination. For CSK these errors are negligible. Moreover, CSK civilian geolocation performances can be further improved by developing a new processor which can use both DEM, allowing accurate knowledge of the atmospheric path of the radar electro-magnetic wave, both ionospheric/tropospheric wave propagation model giving electro-magnetic time delays as function of the some basic variables, such as epoch of the year (to take into account seasonal effects), scene latitude and thickness of atmospheric stratus.

4.6. Complementary Techniques

Some of the previously analyzed limitations and constraints of the tandem-like interferometric technique can be overcome or mitigated through the combined exploitation of complementary techniques such as radargrammetry, which works on amplitude data and allows to do not suffer atmospheric artifacts and all the drawbacks introduced by the phase. Possible techniques can be implemented to make a fusion between interferometric and radargrammetric DEM. The fusion may be both at product level, by reducing systematic error effects and improving DEM accuracy, both at techniques level, by exploiting radargrammetry to solve the phase ambiguity during phase

unwrapping, useful especially in the regions at latitudes over 60°, where SRTM DEM are not available as a reference.

Preliminary analysis performed on specific areas with two CSK Spotlight-2 stereo-pairs (one ascending and one descending), validated with an high resolution LIDAR DEM, show that radargrammetric DEMs can be produced with an horizontal posting of 5 x 5 m^2, and a vertical error (RMS) of 4 m for slopes lower than 20% and 6 m for slopes lower than 100%.

Obviously, also radargrammetry has some drawbacks, for instance in the matching of corresponding points, especially in high density urban areas where multipath and complex scattering effects can degrade the results. Moreover, feature-less areas do not allow radargrammetry to extract height information. Finally, geometric distortions such as layover and shadow make matching phase difficult because of the high difference in the look angle between the acquisitions, and it is possible to mitigate this issue by using different acquisition geometries (e.g. ascending and descending, left and right).

In order to cope with the effects of terrain topography, seasonal effect and land use on the radargrammetric DEM, it is important, during the stereo-pair selection, to set the incidence angle difference larger for flat terrain and smaller for strong-slope terrain. High relieves, with steep slopes, are affected by strong geometric distortions, causing a decreased DEM quality. A snow coverage can reduce the matching accuracy because of missing features, in addition snow and ice decrease the radar backscatter. Moreover, on cultivated, forested and sandy areas, the temporal decorrelation must be as short as possible, not for phase considerations like for interferometry, but to reduce possible change in the scene.

To summarize, with radargrammetry it is not necessary the orbital control required by interferometry to achieve the desired baseline values; atmospheric artifacts and other phase effect are not critical as for interferometry; a reference DEM is not strictly required; the areas where radargrammetry does not perform well are very densely forested or featureless areas, very steep slopes and probably high-density urban areas in certain critical conditions.

Other complementary techniques exist to refine the produced DEM, such as Permanent Scatterers Interferometry (PS-InSAR), (Ferretti, et al., 2001), which is an effective technique for monitoring surface deformation with millimetric accuracy and land subsidence velocity, but which can be very useful also for determining Permanent Scatterers (PSs) height with accuracy in the order of meters. The technique takes as an input a large amount of SAR data, only time-coherent pixels which exhibit phase stability over a long period of time (i.e. PSs) are considered (e.g. man-made structures such as buildings, bridges, antennae). PS-InSAR estimates and remove atmospheric phase contribution, temporal decorrelation, DEM error and system/thermal noise. The interferometric

phase is used to estimate displacement and 3-D coordinates of SAR targets (PSs). In particular, PSs are coherently observed during a long period of time and from different looking angles, the interferometric phase is considered only in correspondence of PSs and then unwrapped and interpolated all over the image. By applying spatial filtering and re-sampling the height data on a regular grid, a digital terrain map is retrieved. The theoretical precision of the estimate of the target height h can be expressed as a function of the number N of images of the data set, of the dispersion of their normal baselines σ_{Bn}, and of the phase noise $\sigma_{\Delta\phi}$, as in equation 4.30:

$$\sigma_h^2 = \left(\frac{\lambda R_0 sin\theta}{4\pi}\right)^2 \frac{\sigma_{\Delta\phi}^2}{N\sigma_{\mathrm{Bn}}^2} \tag{4.30}$$

where λ is the wavelength, θ the incidence angle, and R_0 the sensor-target distance.

The main issue to be tackled for creating DEMs by means of the PS technique is the spatial density of measure points, and thus voids filling, as well as the huge number of images required to achieve high accuracies.

An addition complementary technique is SAR tomography, (Zhu, et al., 2010), which allow to improve the performance of SAR interferometry especially for layover effect. Tomography-based SAR imaging is a recent technique that extends the concept of SAR interferometry to increase the density of measurements points by handling situations where multiple stable scatterers interfere in the same resolution cell. SAR Tomography can be used as complementary technique especially in the monitoring of areas where layover phenomena of SAR image are visible, when several scatterers are within the same resolution cell (urban areas, forest, complex structures, etc.). The drawback of the technique is still the high number of images required, about 30 images, to achieve an accuracy in the order of meters.

4.7. Comparison with the State-Of-The-Art

The first homogenous and highly reliable DEM with DTED-2 specifications was provided by SRTM mission (i.e. Shuttle Radar Topography Mission), performed for ten days in 2000. SRTM represents the first spaceborne single-pass interferometer, obtained by adding to the Shuttle a C-band and a X-band second receive antenna, mounted at the tip of a 60 m deployable mast structure. Within a ten day mission, SRTM collected interferometric data for a near global DTED-2 Earth surface coverage. DTED-2 is commonly said to be the current basic high resolution elevation data source for all military activities and civil systems that require landform, slope and elevation in a

digital format. SRTM mapped the Earth between 60° N and 56° S, for a total of 80% of the lands. In particular, two typologies of products have been processed:

- DTED-1 products, with a resolution in longitude of 3 arc-sec between 0° and 50° of latitude, and of 6 arc-sec between 50° and 60° of latitude, a resolution in latitude always equal to 3 arc-sec, an absolute vertical accuracy better than 30 m with a confidence level of 90%;
- DTED-2 products, with a resolution in longitude of 1 arc-sec between 0° and 50° of latitude, and of 2 arc-sec between 50° and 60° of latitude, a resolution in latitude always equal to 1 arc-sec, an absolute vertical accuracy better than 16 m with a confidence level of 90%.

However, even if SRTM products were properly edited over oceans, lakes and layover/shadow areas, there are still wide voids, in particular at the lower latitudes. For instance, the coverage over Italy is complete at 55%.

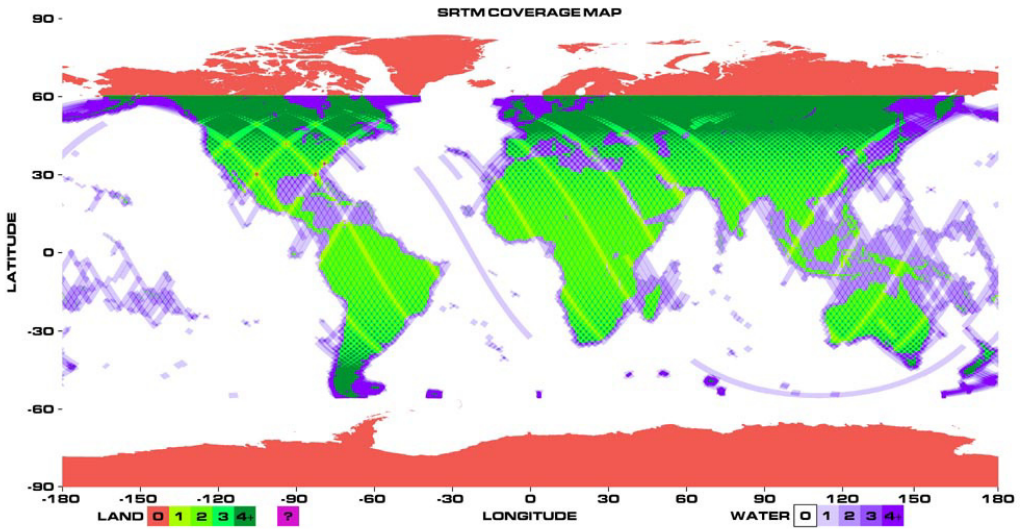

Fig. 4.31 – SRTM data coverage.

Even if electro-optical satellites, also French SPOT satellites are used for DEM production. Available data, known as DEM SPOT 3D, were generated from stereoscopic acquisitions of HRS sensor (i.e. High Resolution Stereoscopic) of SPOT-5 satellite. DEM SPOT 3D products include:

- The Reference3D database, Fig. 4.32, which is a geocoded database with three informative layers (i.e. HRS SPOT-5 derived DEM, images HRS SPOT-2 and quality maps with final DEM accuracies). In 2009, the Reference3D coverage amounted to 50 millions of km^2;
- SPOT DEM, with a final accuracy related to the required area extension and to the availability of Reference3D data, Tab. 4.9;
- SPOT DEM Precision, with an accuracy consistent with DTED-2 standard.

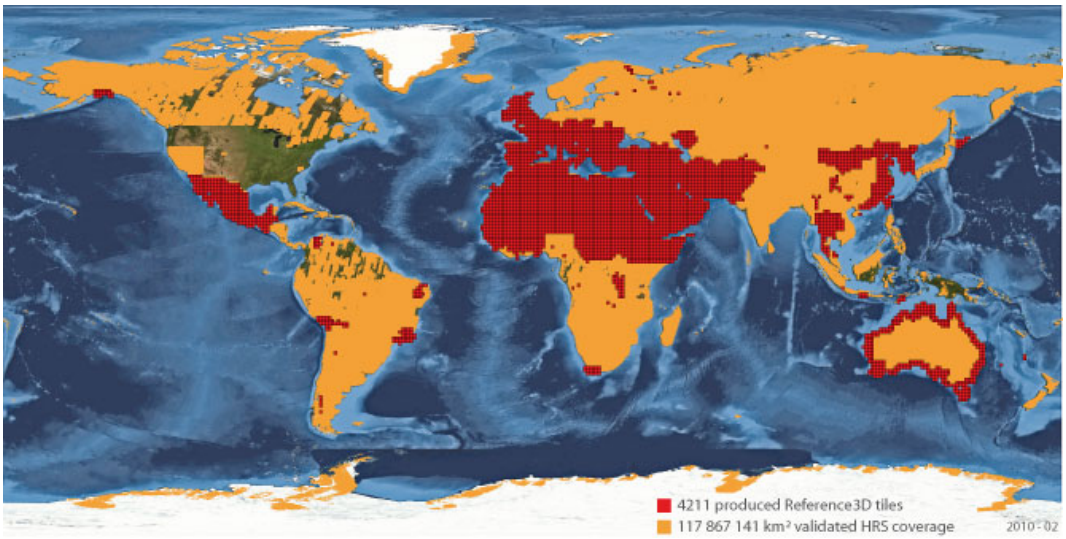

Fig. 4.32 – HRS SPOT-5 Reference3D coverage, updated at February 2010 (117.867.141 km², 4.211 tiles), courtesy of Spot Image.

Absolute Accuracy	Area covered by Reference 3D	Area of 100.000 to 150.000 km^2	Area < 7.200 km^2
Horizontal	< 15 m	< 15 m	< 30 m
Vertical (slope < 20%)	< 10 m	< 10 m	< 20 m

Tab. 4.9 – SPOT DEM features, without GCPs, confidence level of 90%, courtesy of Spot Image.

An additional global DEM was generated by the ASTER sensor (i.e. Advanced Spaceborne Thermal Emission and Reflection Radiometer), which was taken on-board the satellite TERRA, developed as a cooperative effort by NASA, Japanese Ministry of Economy, Trade and Industry (METI) and Japan Space Systems. ASTER GDEM (i.e. Global Digital Elevation Model) is the most accurate global DEM. Data acquired by ASTER sensor are in the near-infrared region of the electro-magnetic spectrum, and the sensor has both nadiral and backward acquisition capabilities, in order to be able to acquire stereoscopic scenes. Since 1999, when the satellite was launched, one million and a half scenes have been acquired, which have been automatically treated for photogrammetric restitution based on auto-correlation principle. The final DEM was released on a grid 1° of latitude x 1° of longitude for a total number of 22.600 tiles, with a grid spacing of 1 arc-sec, after having implemented several filtering treatments for clouds removal and anomalies correction. The estimated absolute vertical accuracy after post-processing is 20 m with a confidence level of 95%, while the absolute horizontal accuracy is 30 m with a confidence level of 95%. The coverage of the ASTER GDEM is larger than SRTM coverage, going up to 83° N and 83° S.

Finally, TerraSAR-X/TanDEM-X mission (i.e. TerraSAR-X Add-On for Digital Elevation Measurement) has the potential to close the above listed gaps, fulfilling the requirement of a global homogeneous high-resolution coverage DEM, providing vital information for several applications.

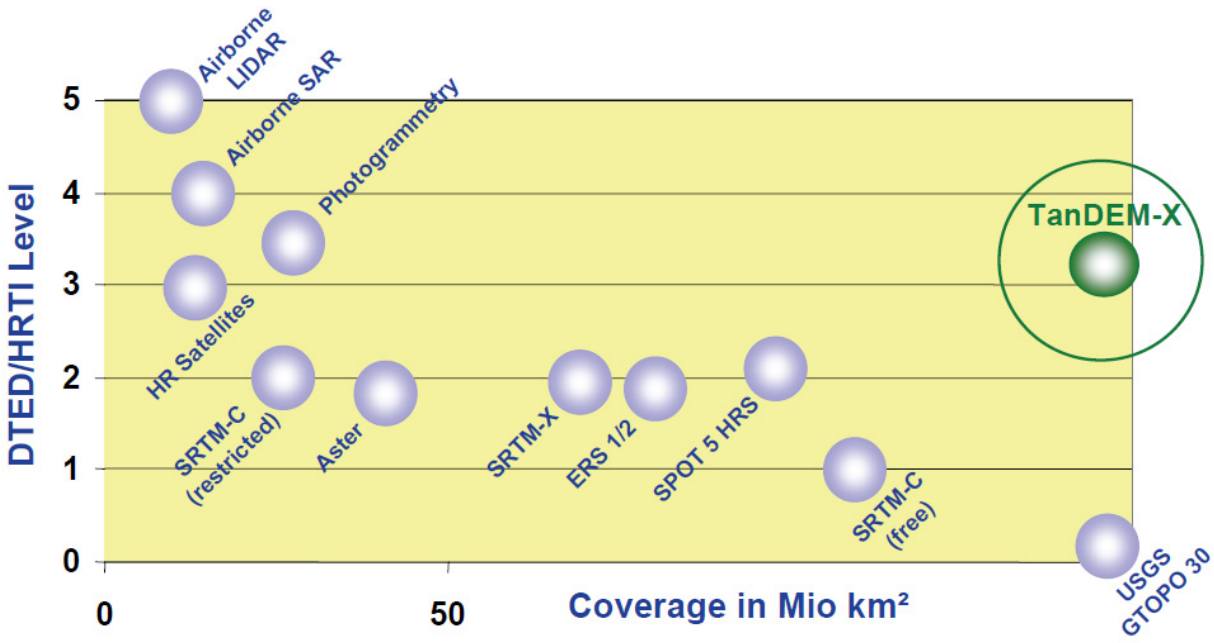

Fig. 4.33 – Existing DEM: state-of-the-art, coverage versus accuracies, courtesy of DLR.

TerraSAR-X/TanDEM-X mission, based on the German SAR remote sensing satellites TerraSAR-X and TanDEM-X, is aimed at the acquisition of the dataset required for the generation of:

- a global homogeneous DEM of a quality level consistent with NGA (i.e. National Geospatial-Intelligence Agency) standard HRE-GP (i.e. High Resolution Elevation - Geographic Projection, Fig. 4.34), (National Geospatial-Intelligence Agency, 2009);
- a very high accuracy DEM on specific local areas of a quality level consistent with NGA standard HRE-40, Fig. 4.34, (National Geospatial-Intelligence Agency, 2009).

In particular, the DEM generated from TerraSAR-X/TanDEM-X mission on a global scale will have:

- a spatial resolution (i.e. posting) equal to 12 x 12 m^2;
- an absolute vertical accuracy better than 10 m (90% confidence interval);
- a relative vertical accuracy (point-to-point errors in geo-cells of 1° latitude x 1° longitude, 90% confidence interval) better than 2 m for terrain slopes below 20% and better than 4 m for terrain slopes above 20%.

Instead, the very high accuracy DEM which will be generated on specific local areas will have:

- a spatial resolution equal to 6 x 6 m^2;
- an absolute vertical accuracy better than 5 m (90% confidence interval);
- a relative vertical accuracy better than 0.8 m (90% confidence interval).

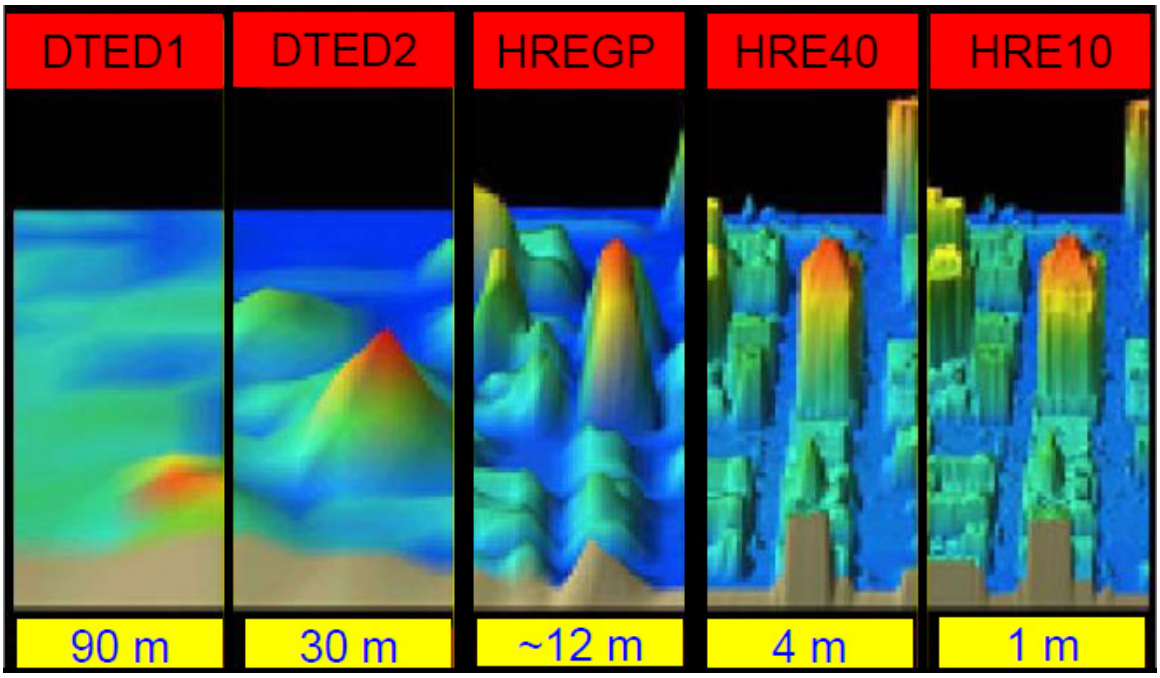

Fig. 4.34 – NGA standards for elevation data, courtesy of NGA .

Currently, the global DEM generated from TerraSAR-X/TanDEM-X has the highest accuracies respect to any other global DEM generated from satellite SAR data. To achieve these accuracies, the two radar satellite orbit in an innovative "Helix" formation, with relative distances variable along the orbit both in the along-track direction and in the across-track direction, achieving some hundreds of meters.

TerraSAR-X satellite was launched into orbit in June 2007, TanDEM-X satellite in June 2010. They were developed through a Public and Private Partnership (PPP) consortium between the German Aerospace Center DLR and the EADS ASTRIUM Society, and the Infoterra GmbH Society, German part of Astruim GEO-Information Services, detains the commercial rights, while DLR is responsible of the exploitation for scientific purposes. The acquisition of the dataset started in December 2010, after the completion of the Commissioning phase of TanDEM-X, and at the beginning 2012 the first global acquisition campaign was completed. The second global acquisition campaign, with higher baseline values, is currently ongoing and the end is foreseen for the middle 2013. It will be useful to refine the DEM generated at the end of the first global acquisition campaign, thanks to a "dual-baseline" phase unwrapping processor which allows to increase the robustness of the DEM product. At the interferometric acquisitions also ad-hoc radargrammetric acquisitions are added in order to solve the phase ambiguity during phase unwrapping step, mainly useful for the regions at latitudes over 60°, where also SRTM reference DEMs are not available, which are required to increase the robustness of phase unwrapping algorithm. A third and a fourth ad-hoc acquisition campaign are required for areas with higher complexity (e.g. Antarctica, sandy

areas with low backscattering levels, etc), with residual phase unwrapping errors or characterized by strong layover/shadow effects, for missed acquisitions, which allow to guarantee an homogeneous quality of the final DEM product. Further six months will be dedicated to the local DEM production at very high resolution (i.e. HRE-40).

To summarize, many DEMs exist, with different accuracies and different coverage, and among them the DEM which offers the best quality features is the TerraSAR-X/TanDEM-X global DEM, which at present is being acquired and processed.
In this framework, the DEM generated from CSK interferometric data is absolutely competitive with the state-of-the-art (i.e. DEM from SAR satellites) in terms of accuracies, but the operational concept behind the CSK employment is completely different from the operational concept of TanDEM-X. In fact, TanDEM-X is a satellite exclusively dedicated to the mission of generating a global DEM, while CSK constellation has several purposes and has to fulfill different user classes needs, therefore only a part of the satellites resources can be addressed to the generation of a DEM, and this is one of the reasons why the operational concept in DEM generation from CSK data is centered on the capability to quickly generate on-demand a very high accuracy DEM on a specific selected area.
In order to be consistent with this operational concept, it is necessary to characterize the quality of a DEM which can be generated from CSK data (previous paragraphs as an articulated case study) and it is necessary to develop a procedure to apply on-demand and which allows to easily make all the passages up to the production of the final DEM, consistent with all the relevant standards. This second issue will be analyzed in the following paragraph.

4.8. Innovative Procedure for On-Demand DEM Production from CSK

As clearly shown in Fig. 4.35, and quantified in equation 4.31, the DEM vertical accuracy strongly affects the geolocation accuracy of a SAR image which is geocoded using that DEM, (Koppe, et al., 2010). The geolocation accuracy is one of the most important image parameter for an operational user.

$$loc_{err} = \frac{h_{err}}{tan(\alpha_{inc})} \tag{4.31}$$

In equation 4.31, h_{err} is the DEM absolute vertical error, loc_{err} represents the range geolocation error and α_{inc} is the incidence angle.

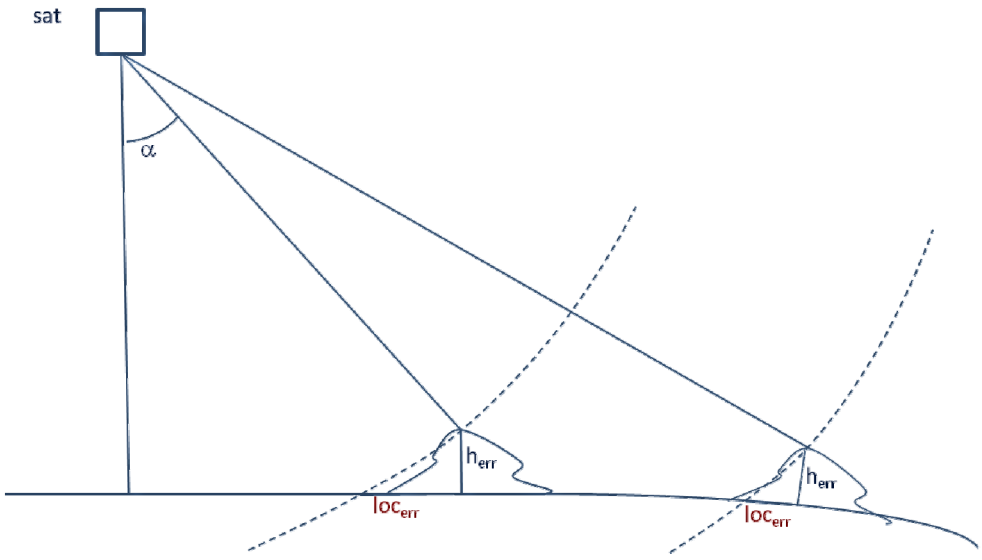

Fig. 4.35 – Influence of DEM vertical accuracy on the range geolocation accuracy.

In particular, at higher incidence angles, the same DEM vertical error yields a lower geolocation error, as shown in the parametric graphic in Fig. 4.36, from which it is possible to observe how it is necessary to have a very high accuracy DEM for processing SAR images in order to do not introduce high geolocation errors during the geocoding process only caused by a DEM absolute vertical error.

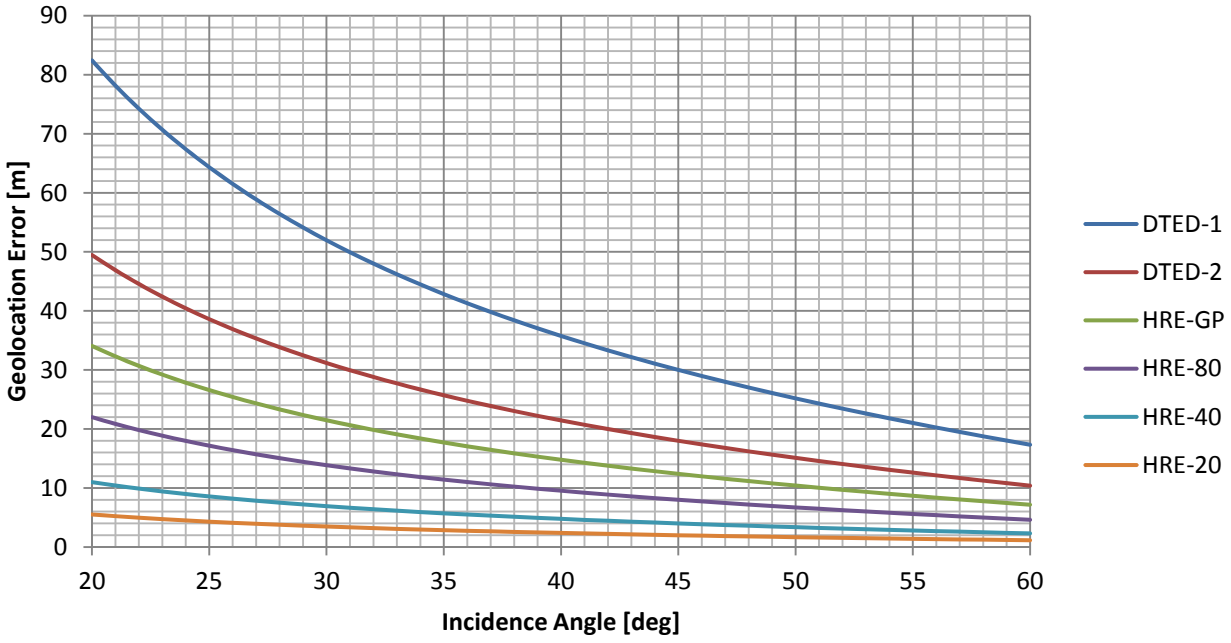

Fig. 4.36 – Behavior of geolocation error with incidence angle, for different DEM absolute vertical errors.

The aim of this paragraph is to create a procedure which can be applied in accordance with the CSK operational concept for DEM production, fulfilling on-demand the need of quickly generation of

very high accuracy DEM on a specific selected area. This procedure will allow the user to easily make all the passages up to the production of the final DEM, consistent with all the relevant standards.

In Fig. 4.37 all the passages of an end-to-end DEM production procedure from CSK interferometric data are synthesized, and analyzed in the following part of this paragraph.

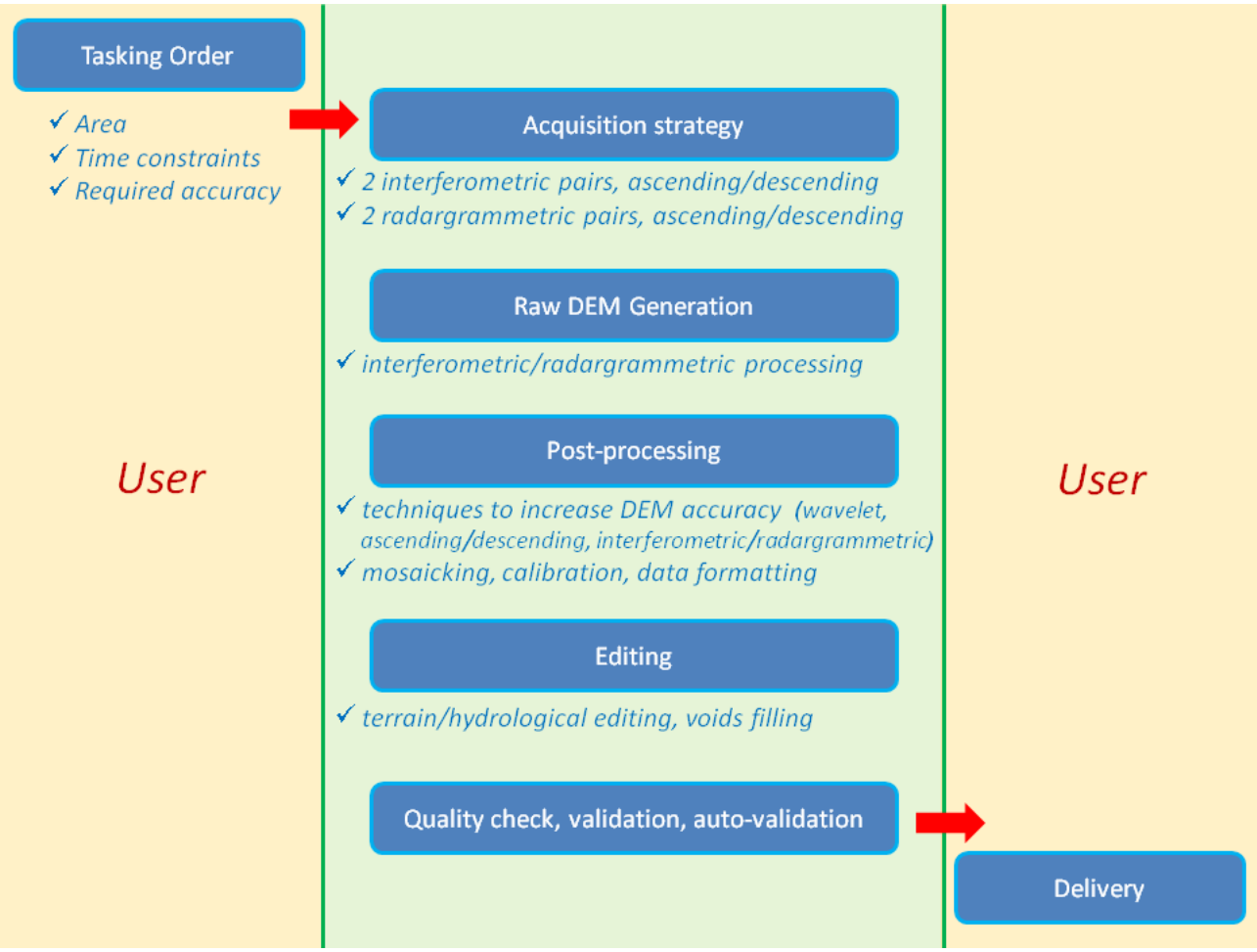

Fig. 4.37 – CSK DEM production procedure.

As a first step of the process, in accordance with a tasking order in input to the procedure, which describes the area where a DEM has to be produced and in what time the user requires the DEM with a defined accuracy, the acquisition phase of the CSK dataset starts, exploiting the high revisit time of the constellation on the same site to obtain both interferometric and radargrammetric images.

In particular, as described in the previous paragraphs, the acquisition strategy mainly depends on:

- the time and the accuracy constraints, which affect the opportunity to acquire ascending and descending images in order to increase the DEM accuracy through a data fusion;
- the site orography, which affects the selection of a proper interferometric baseline or the opportunity to acquire several interferometric pairs with different baseline in order to perform a

"dual-baseline" phase unwrapping to increase the robustness of the DEM product, (M. Lachaise, 2010).

Furthermore, depending on the site orography, radargrammetric pairs or triplets can be acquired in order to:

- solve the phase ambiguities during the phase unwrapping step for orography difficult to be reconstructed, useful especially in the regions at latitudes over 60°, where SRTM DEM are not available as a reference, (Sowter, et al., 2003);
- increase the interferometric DEM accuracy in low coherence areas through an InSAR and radargrammetry data fusion, (Crosetto, et al., 1999);
- extract 3D coordinates (i.e. measured coordinates) through space intersection for DEM calibration purposes;
- if required by the user, generate detailed local 3D models (e.g. building in urban scenarios) to superimpose to the DEM, Fig. 4.38.

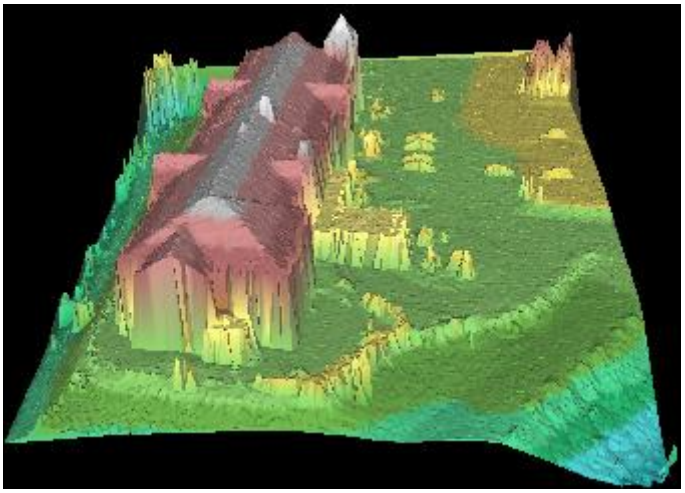

Fig. 4.38 – Concept example: 3D model superimposed to a DEM. Courtesy of Mosaic 3D ©.

A reference dataset required for the previously detailed purposes is composed by:

- two CSK radargrammetric pairs, one in ascending orbit and one in descending orbit, both pairs with a difference in look angle of about 15-20°. This dataset allows all the possible combinations of same-side and opposite-side radargrammetry.
- two CSK one-day interferometric pairs, one in ascending orbit and one in descending orbit. This dataset allows, among other advantages, the mitigation of layover-foreshortening through different viewing geometries.

CSK constellation is able to perform at least four acquisitions per day at the equator, one left looking and one right looking at 6 A.M. local time (ascending orbit), one left looking and one right looking at 6 P.M. local time (descending orbit). In Fig. 4.39 it is represented an example of data

take opportunities (DTO) analysis on a timeframe of one week on a selected site at the equator (worst case), showing how many acquisition opportunities exist if all the satellites of the constellation are used and both right and left looking geometries are enabled.

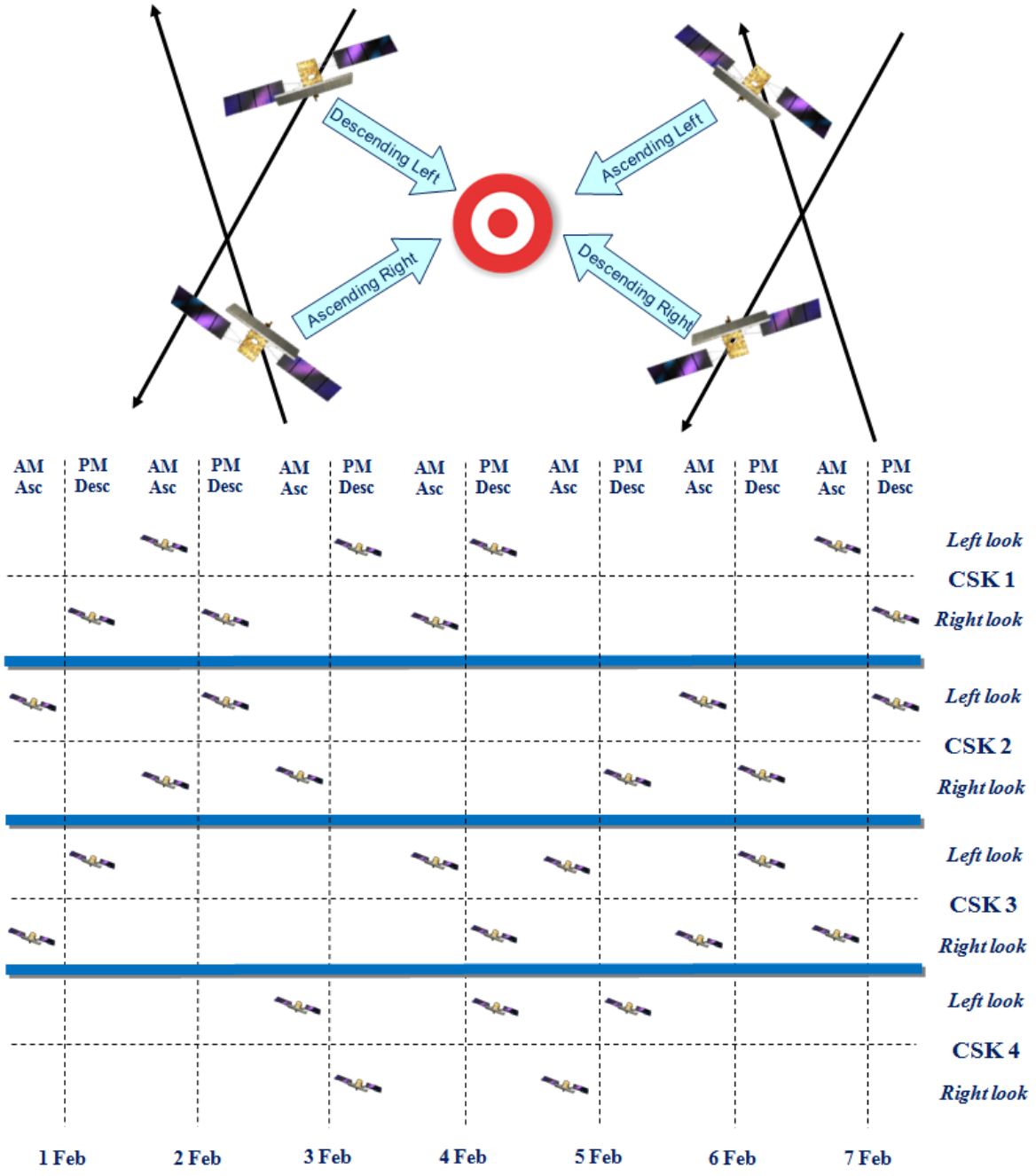

Fig. 4.39 – CSK constellation unconstrained revisit on a selected site.

The revisit shown in Fig. 4.39 does not take into account any constraint. If interferometric pairs have to be acquired, some constraints arise, such as fixed beam, looking side, orbit direction, affecting the results of the DTO analysis. In particular, during a repetitivity period of 16 days there are four interferometric acquisitions with defined parameters, and two of them are one-day

interferometric acquisitions (CSK-2/3), Fig. 4.40. It means that since every day there are at least four DTOs on a site, every day it is possible to start four series of interferometric acquisitions, and each series has four interferometric DTOs in a 16 days repetitivity cycle.

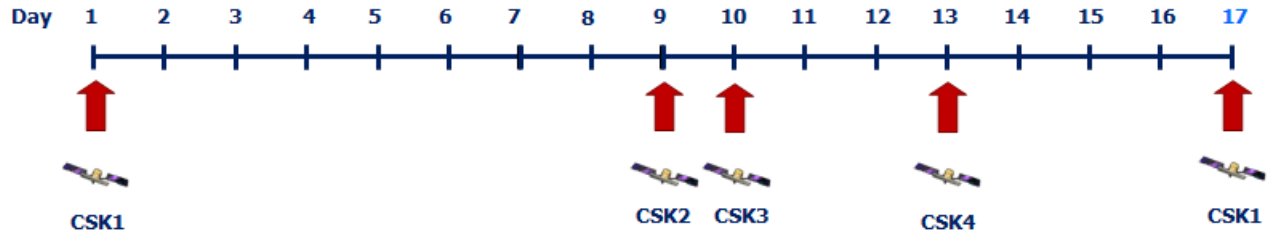

Fig. 4.40 – CSK interferometric DTOs.

The above analysis show that it does not take so long to acquire the required dataset for the DEM generation purposes. According to the time constraints in input to the procedure, it is possible to acquire a partial dataset which nevertheless allows to obtain DEM product of lower quality.

After the dataset acquisition phase, the raw DEM generation phase is performed, through interferometric and radargrammetric processing, following all the processing steps extensively described in the previous part of the Thesis.

After the generation of the raw DEM, it is necessary to apply the post-processing techniques proposed in the previous paragraphs to increase the accuracy of the DEM, and to perform mosaicking if necessary, calibration and data formatting. Auxiliary data, such as globally distributed reference height values given by ICESAT data, can be used for calibration purposes.

As a further step, an editing phase is convenient before the delivery of the DEM product to the user. The editing level of effort is very demanding, but according to the proposed operational concept of DEM generation with CSK, it is probable that the area where an updated DEM is required by the user is quite narrow, thus the editing effort can be limited and can be supported only if allowed by the time constraints. The editing concerns terrain editing and voids filling, as well as hydrological editing, related to wrong height values along water bodies. A void can be considered as a geolocation value that was not well sensed, thus the processor knows that the corresponding height value is inaccurate and the relevant pixels do not contain valid height information. The editing includes paved areas, pylons, vegetated-wooded areas and snow-ice, water bodies, urban areas special processing to suppress building-trees with ortho-photos, etc.
The main terrain editing and voids filling steps include:

- the removal of spikes and wells;
- the interpolation for voids with a maximum diameter of 9 pixels or less;

- the infilling for voids with a larger diameter through external dataset.

The main hydrological editing steps include:

- delimitation of water bodies;
- derivation of related heights values;
- oceans, seas and lakes flattening to constant heights;
- rivers local height setting to the same height gradient of the terrain.

As the last step of the procedure, a quality check is necessary in order to validate the DEM product that was generated and to fulfill the quality specifications required by the user in accordance to NGA standards, (National Geospatial-Intelligence Agency, 2009). Classical DEM quality check and validation techniques are based on an analytical, visual and statistical quality control. If a reference ground truths are available with a guaranteed accuracy at least one order of magnitude higher than the expected accuracy of the DEM product, it is possible to perform a comparison and to compute the classical statistical errors such as Linear Error 90% (LE90) and Circular Error 90% (CE90) respectively for vertical and horizontal accuracy, Root-Mean-Square Error (RMSE) and so on.

Unfortunately, quite often suitable ground truths are not available for validation purposes, however it is necessary to perform a validation of the DEM product. For these reasons, an innovative DEM auto-validation technique was conceived and it is under consolidation, in order to exploit available data with high horizontal accuracy to assess also the DEM vertical accuracy. The motivation why this technique was conceived is given by the consideration that data with very high vertical accuracy, at least one order of magnitude better than the expected accuracy of the produced data, are very difficult to obtain and usually require very expensive instruments and procedures to be collected (e.g. LIDAR, differential GPS, etc), while data with very high horizontal accuracy are more easily achievable.

The proposed model gets the vertical accuracy of the produced DEM from the planimetric error obtained from the comparison between the SAR image Geocoded Terrain Corrected (GTC) on the same DEM and an image with very high geolocation accuracy, such as Google Earth optical images, open source even if with a poor information age.

The flow which describes the DEM auto-validation technique is represented in Fig. 4.41.

After having generated a DEM from the Single Look Complex Slant Range (SCS) interferometric pair, the SCS SAR image is geocoded on the produced DEM, obtaining a Geocoded Terrain Corrected (GTC) SAR image. A quantitative assessment is then performed of the planimetric shift between targets in the GTC image and in the Google Earth image. Therefore, the DEM absolute vertical error can be estimated from equation 4.31, taking into account a model of the geocoding error which can be introduced in the process.

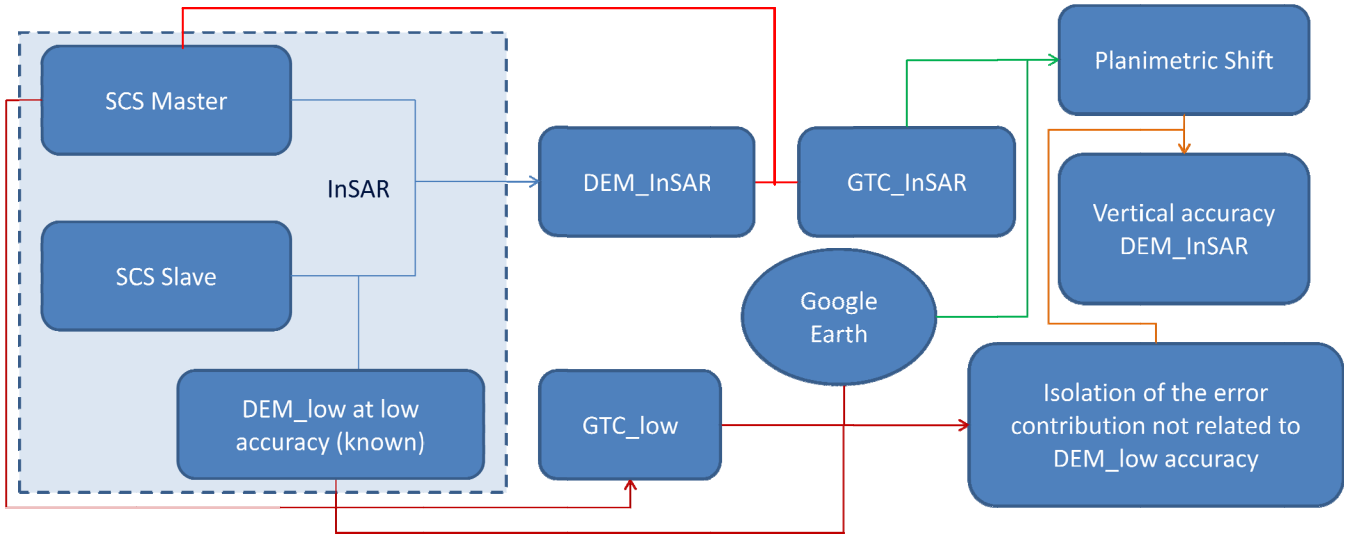

Fig. 4.41 – Flow describing the DEM auto-validation technique.

The main advantages of the DEM auto-validation technique are listed in the following:

- Possibility to easily perform a large scale DEM quality control;
- Possibility to automate the validation process;
- Possibility to validate also DEM in non accessible areas or where ground truths are not available.

Considering Fig. 4.35, it is important to understand one of the reasons which justify the proposed technique. In particular, the geolocation accuracy of Google Earth is very high, (Potere, 2008), especially in the developed Countries, because the geolocation accuracy of GeoEye optical images is around 3 m, and the images are mosaicked among them, which further increases the geolocation accuracy. On the other hand, the vertical accuracy of Google Earth is quite poor (e.g. DTED-1).

It is important to consider that the geolocation error of the GTC SAR image is given also by the DEM vertical accuracy, but other contributions affect this figure, such as the geocoding process intrinsic error, and other elements listed in Tab. 4.10.

Error contributions related to the platform	Along-track position errors Across-track position errors Radial position error Velocity errors
Error contributions related to SAR Payload	Phase and amplitude errors On-board electronics delay errors Echo datation accuracy
Errors contributions related to the processor	Intrinsic geocoding accuracy Orbital data availability and accuracy
Errors contributions related to DEM quality	Local topography knowledge accuracy locale

Tab. 4.10 – Main contribution to geocoding error.

In fact, the geocoding algorithm with respect to a DEM, to generate a GTC product, is essentially based on a re-sampling of the input image onto a uniform spaced Earth fixed map grid. The re-sampling positions on the input image are calculated based on a rigorous map-to-image resection algorithm. Starting from the generic output position, expressed in (East, North, h) coordinates, the corresponding geodetic coordinates (lat, lon, h) are computed, and then the cartesian coordinates (x, y, z). At this point, an iterative process is started, searching for the slant range and the azimuth position of the target which satisfy the SAR Doppler equation assuming data at Zero Doppler ($f_{Dc} = 0$) and the SAR slant range equation, equation 4.32:

$$f_{Dc} = \frac{2}{\lambda_r R}\left(\overrightarrow{X_s} - \overrightarrow{X_T}\right) \cdot \left(\overrightarrow{V_s} - \overrightarrow{V_T}\right) = 0$$
$$sr_j = sr_0 + m_r \cdot j = R \tag{4.32}$$

Where f_{Dc} is the Doppler centroid frequency (Hz), λ_r the radar wavelength (m), $\overrightarrow{X_s}$ the sensor position vector, $\overrightarrow{X_T}$ the target position vector, $\overrightarrow{V_s}$ the sensor velocity vector, $\overrightarrow{V_T}$ the target velocity vector, R the distance between the sensor and the target, j the slant range index of the pixel, sr_0 the slant range distance of the first pixel, sr_j the slant range distance of pixel with index j and m_r the slant range pixel spacing.

The computed slant range and the azimuth position values are used to interpolate the radiometric value of the input image to be inserted at the corresponding output position. The re-sampling procedure gives a localization performance depending on the accuracy of the following input data:

- Orbital data used to locate the sensor during the acquisition process;
- Doppler centroid estimated during the SAR focusing process;
- The slant range distance;
- The Earth model used as reference Earth surface.

This means that among the previously mentioned contributions that affect the geolocation error, there are also orbital data accuracy, Doppler centroid estimation accuracy, the effect of on-board electronics delay errors on the slant range distance, coregistration accuracy of the DEM used for the geocoding with the SCS image, and finally DEM vertical accuracy.

In order to isolate the DEM vertical accuracy among all the contributions previously described, a technique was conceived which consists in geocoding with the same technique the same SCS SAR image both on the produced DEM and on another DEM with a known absolute vertical accuracy, (W.Koppe, 2010), as in the flow in Fig. 4.41. In this latter case, the comparison of the geocoded image with the Google Earth image allows to quantify the geocoding errors that are not related to

the known DEM vertical error, which is known and can be removed. The estimated geocoding errors can be taken into account in the first case in order to isolate the generated DEM vertical error contribution to the geolocation error.

4.9. Interferometric Specifications for New Generation SAR Satellites

Based on the lesson learnt from CSK, in order to improve the coherence among interferometric acquisitions from different satellites, and thus the accuracy of the generated DEM, it is necessary:

- to foreseen as a requirement that an inter-satellite pointing calibration shall be performed to guarantee a certain overlap of the Doppler bandwidth between interferometric acquisitions, with a maximum value of the Doppler centroid shift;
- to provide the User Ground Segment (UGS) with a Common Band Filtering algorithm inside the coregistration processor, which can be optionally run according to the final application, giving the User the possibility to set the size of the common bandwidth to be filtered.

  Furthermore, in order to increase DEM accuracy, further specifications at UGS-level for next generation SAR satellites are related to the development of a DEM processor able to:

- to recover areas affected by layover/shadow and reduce both systematic and noise errors in the DEM thanks to the multiple information available in overlapping areas, providing the UGS with a multi-pass data-fusion processor to take advantage of multiple acquisitions on the same site to drastically reduce the random noise;
- to apply a multi-baseline phase unwrapping and geocoding processor, in order to obtain a higher robustness and sensitivity to the topography, making phase unwrapping feasible also in difficult areas;
- to exploit an orbital processor which can take advantage of differential GPS measurements in order to obtain accurate interferometric baseline measurements (in the order of 1 mm).

Previous statements can be summarized in the following requirements:

- Interferometric DEM multiple geometry data fusion: the DEM processor shall be able to merge interferometric pairs obtained with different acquisition geometries in order to reduce data voids due to layover/shadow regions;
- Interferometric DEM multi-baseline phase unwrapping: the DEM processor shall be able to merge interferometric pairs obtained with different baselines in order to make phase unwrapping feasible also in difficult topography areas;
- Interferometric DEM cross-calibration: the DEM processor shall be able to merge interferometric pairs obtained with different acquisition geometries in order to correct the acquisition geometry parameters.

- Radargrammetric DEM: the DEM processor shall be able to perform radargrammetric processing.

4.10. Conclusions

The analysis performed in this Chapter allowed to explore the interferometric capabilities of CSK constellation for DEM generation, and several test cases were studied on a single scenario where ground truths were available for quality check and validation purposes. The obtained results permitted to appreciate the DEM accuracies that CSK satellites allow to achieve in favorable cases. Even if a more extensive experimental campaign would be necessary if DEM quality certification aims wanted to be pursued, the results of the analysis performed are sufficient to understand the potentialities of CSK constellation for DEM generation according to the proposed operational concept described in the previous paragraphs. These results allow to state that the DEM which is possible to generate from CSK data can be compliant with HREGP NGA standard, with accuracies between HREGP and HRE-80 quality levels, (National Geospatial-Intelligence Agency, 2009). Referring to Fig. 4.36, the contribution of this DEM vertical error on the geolocation accuracy of GTC products using the generated DEM is lower than 10 m for high incidence angles.

The study conducted in this Chapter can be further extended in order to take into account also scenarios more challenging according to a topographic point of view. Obviously, the driver in the selection of the challenging area should be the availability of ground truths for quality check and validation purposes, even if the auto-validation method proposed in the previous paragraphs may be applied once certified as a validation technique. A challenging scenario which would allow the assessment of CSK potentialities in DEM generation also in difficult areas is represented by Uluru Ayers Rock, where a very steep heights gradient would be a serious test case also for phase unwrapping processors.

Furthermore, a theoretical error study and an experimental sensitivity analysis was performed based on CSK data in order to understand the dependencies of DEM accuracy on several relevant parameters such as normal baseline length, coregistration accuracy (DEM-assisted or not), usage of calibration GCP during processing and application of CBF.

In addition, a trade-off analysis was performed to understand if and how much it is possible to achieve improvements in the DEM final accuracy through a proper interferometric processing or other ad-hoc techniques. In particular, an analysis of the improvement of the DEM accuracy through a combination of acquisitions on the same site from ascending and descending passages was performed, in order to solve part of the errors introduced by shadowing and layover effects. Also a wavelet-based fusion between the generated DEM and a low resolution SRTM DEM was

performed in order to mitigate the atmospheric disturbances at low frequencies due to the repeat-pass interferometry, through the injection of the low spatial frequencies of the low accuracy SRTM DEM, preserving the high spatial frequencies and details information of the DEM generated from CSK.

A critical analysis was performed to discuss all the factors and parameters which limit the achievable performances, as well as a combined analysis of complementary techniques was performed in order to mitigate drawbacks of interferometry through techniques and data fusion, with the aim of maximizing the final DEM accuracy. Furthermore, the critical analysis outputs allowed to point out possible interferometric specifications for next generation SAR satellites.

Finally, an innovative procedure for on-demand DEM production from CSK data was elaborated, which fulfill a proposed operational concept focused on the capability to quickly generate on-demand a very high accuracy DEM on a specific selected area. An innovative DEM auto-validation method was also introduced and it is under review, to perform a quality analysis of a generated DEM even without vertical ground truths.

CHAPTER 5
SHIP MONITORING TECHNIQUES: STATE-OF-THE-ART

This Chapter focuses on ship monitoring techniques based on single/multi-platform multi-channel SAR data. The basic principles of Ground Moving Target Indication (GMTI) are described, in particular two GMTI techniques are analyzed, such as Displaced Phase Center Antenna (DPCA) and Along-Track Interferometry (ATI), (Rizzato, 2012).

5.1. Ground Moving Target Indication

Historically, the purpose of Moving Target Indication (MTI) radars was to suppress from signals every static or slow-moving scatterers, in order to keep the only moving targets information. MTI systems based on fixed ground radars exploited the Doppler shift in the received echoes to separate moving targets from clutter, considered that the spectral displacement is related to the target velocity in range direction (Skolnik, 1989). For spaceborne systems, MTI is significantly more complex, since the moving platform carrying the radar also induces a Doppler spectrum on a fixed scene, allowing to form a synthetic aperture. However, it is not possible to separate the Doppler shift contribution due to a moving target from the contribution due to the clutter. In order to isolate the moving target, it is necessary to suppress the clutter. In single channel SAR systems moving targets can be detected only if their velocity is high enough to come out from the clutter spectrum, while two channels SAR systems allow to suppress the clutter or to estimate the target velocity (Ender, 1996).

5.2. Dual Receive Antenna

In single-channel SAR data, there is an intrinsic ambiguity in the Doppler signature of a target because Doppler shift can be related to the azimuth position of the scatterer in the antenna beam or to its radial velocity. This ambiguity can be solved through multichannel SAR systems, (Ender, 1996). Several operational and next generation spaceborne SAR systems are limited to two receiving chains and have programmable antenna arrays, like a Dual Receive Antenna mode of operations used in TerraSAR-X (J. Mittermayer, 2003) and RADARSAT-2 (Chiu, et al., 2008).
In a Dual Receive Antenna mode, the transmission of the signal exploits the full aperture of the antenna, while the reception is performed, at the same time, by two half partitions in the along-track

direction of the antenna array. The signals of both receiving antennas are demodulated, sampled and recorded separately.

5.3. Moving Target and Sea Clutter Signal Models

A mathematical formulation of a moving target signal model is provided in this paragraph to introduce GMTI techniques. Considering a flat-Earth model and the geometry shown in Fig. 5.1, the range history *r(t)* between the satellite and the moving target on the Earth's surface can be modeled through equation 5.1.

$$r(t) = \sqrt{\left[x_1 + (v_{x1} - v_s)t + a_{x1}\frac{t^2}{2}\right]^2 + \left[y_1 + v_{y1}t + a_{y1}\frac{t^2}{2}\right]^2 + h^2} \tag{5.1}$$

where *v* and *a* respectively represent target velocity and acceleration, *x* and *y* the target along-track and across-track position, *h* the satellite altitude, v_s and *t* the satellite velocity and the azimuth slow time.

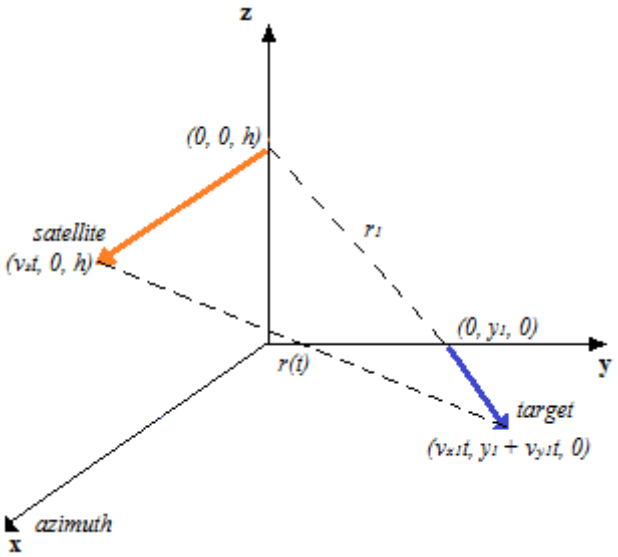

Fig. 5.1 – Range history *r(t)* of a target moving with constant velocity in a flat-Earth geometry.

The target velocity (v_{xT}, v_{yT}) and position (x_T, y_T), at time *T* when the azimuth positions of the satellite and the moving target coincide, are given by equation 5.2:

$$\begin{aligned} v_{xT} &= v_{x1} + a_{x1}T \\ v_{yT} &= v_{y1} + a_{y1}T \\ x_T &= x_1 + v_{x1}T + a_{x1}\frac{T^2}{2} \end{aligned} \tag{5.2}$$

$$y_T = y_1 + v_{y1}T + a_{y1}\frac{T^2}{2}$$

By neglecting the acceleration components in the hypothesis of constant target velocity (thus $v_{xT} = v_{x1} = v_x$ and $v_{yT} = v_{y1} = v_y$), and approximating the range history equation (5.1) by its second-order Taylor expansion around T, (Gierull, 2006), equation (5.3) is obtained:

$$\begin{aligned} r(t) &\cong r(T) + r'(T)(t-T) + r''(T)\frac{(t-T)^2}{2} = \\ &= r_T + v_y\gamma(t-T) + \frac{v_{rel}^2}{2r_T}(t-T)^2 \end{aligned} \tag{5.3}$$

with:

$$\begin{aligned} r_T &= \sqrt{y_T^2 + h^2} \qquad \gamma = \frac{y_T}{r_T} \\ v_{rel}^2 &= (v_x - v_s)^2 + v_y^2(1-\gamma^2) \end{aligned} \tag{5.4}$$

Replacing equation (5.3) in the expression of the demodulated two-dimensional baseband signal received from the target, and considering a range compression via matched filtering, the received signal from a moving target is given by equation (5.5):

$$s(t) = B\ exp\left[-j\frac{4\pi}{\lambda}r(t)\right] \tag{5.5}$$

valid in the interval $[-T_e/2; +T_e/2]$, where B is a complex amplitude taking into account the antenna pattern and the reflectivity of the scatterer, *r(t)* is the range history given by (5.3) and T_e is the target exposure time defining how long the target stays in the antenna beam (in the -3 dB limit).

Specializing equation (5.5) for a Dual Receive Antenna, the received signals from the two parts of the antenna are expressed in equation (5.6), valid in the interval $[-T_e/2; +T_e/2]$:

$$\begin{aligned} s_1(t) &= B\ exp\left[-j\frac{4\pi}{\lambda}r(t)\right] \\ s_2(t) &= B\ exp\left[-j\frac{4\pi}{\lambda}r(t)\right] exp\left[-j\frac{2\pi}{\lambda}u(t)d\right] \end{aligned} \tag{5.6}$$

where *d* is the distance between the two receive sub-apertures and *u(t)* is the directional cosine approximated by, (Gierull, 2006):

$$u(t) = \cos(\alpha(t)) \cong \frac{v_x - v_s}{r_T}(t-T) \tag{5.7}$$

where $\alpha(t)$ is the angle between the antenna-target line of sight and the azimuth direction (Fig. 5.2), and the distance target-satellite is large enough to consider the echo signal wavefronts arriving parallel to the two sub-apertures.

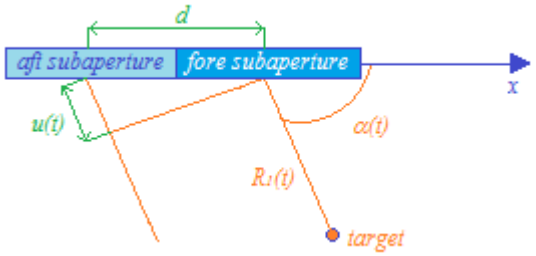

Fig. 5.2 – Two antenna sub-apertures in a dual receive antenna.

Considering the sea surface for ship monitoring purposes, the sea clutter can be characterized through a K-distribution, as suggested in (Antipov, 1998), or through several point-like scatterers per resolution cell whose reflectivity follows a circular complex Gaussian distribution. Following the second approach, the mean reflectivity coefficient σ_0 for the Gaussian distribution is extrapolated for the X-band from (F. Nathanson, 1999), while the decorrelation time τ_c of the sea surface is given by equation 5.8 (S.J. Frasier, 2001):

$$\tau_c \cong 3\frac{\lambda}{u} erf^{-1/2}\left(2,7\frac{x}{u^2}\right) \tag{5.8}$$

where u is the wind speed, x is the spatial resolution in ground range and *erf (x)* is the Gauss error function.

5.4. Displaced Phase Center Antenna

The Displaced Phase Center Antenna (DPCA) is a technique for clutter suppression and moving target indication in SAR data, (Ender, 1996). To apply DPCA technique, two along-track displaced antennas (or sub-apertures) are needed, whose phase centers have to coincide in successive time instants t_1 and t_2.

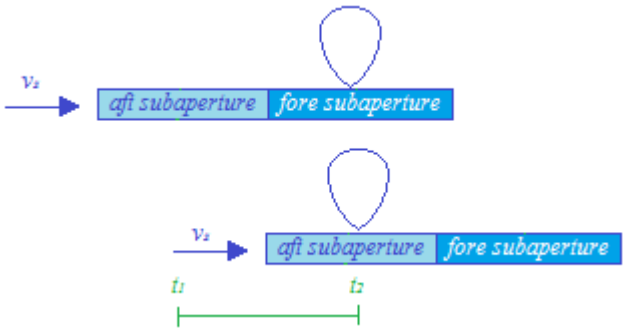

Fig. 5.3 – Classical DPCA.

DPCA technique consists in making a difference between complex SAR data from two channels, in order to remove stationary objects (clutter) which appear in the same position, and to preserve echoes from moving targets. Theoretically, the value of the Pulse Repetition Frequency (PRF) has to be fixed according to satellite velocity and the distance between the antennas. This constraint can be overcome, as shown in (R.G. White, 1997), it is only required to perform "channels coregistration" (i.e. time shifting one signal by re-sampling it). With an ideal radar, without noise and with a perfectly stationary clutter, sea clutter and static targets are completely removed after DPCA processing. However, for real system, clutter suppression is mainly limited by radar intrinsic noise, coregistration errors and amplitude or phase imbalance of the receive channels, (Sharma, 2004).

Considering equations (5.6) for signals $s_1(t)$ and $s_2(t)$ received by the two antenna sub-apertures, the DPCA output, equal to the difference between the two co-registered channels by a time shift of $d/2v_s$, where d is the physical separation of the antenna centers, is given by equation (5.9):

$$DPCA(t) = s_1(t) - s_2\left(t + \frac{d}{2v_s}\right) = Be^{-j\frac{4\pi}{\lambda}r(t)}\left(1 - e^{-j\frac{2\pi}{\lambda}E(t)}\right) =$$
$$= Be^{-j\frac{4\pi}{\lambda}r(t)}e^{-j\frac{\frac{2\pi}{\lambda}E(t)}{2}}\left(e^{j\frac{\frac{2\pi}{\lambda}E(t)}{2}} - e^{-j\frac{\frac{2\pi}{\lambda}E(t)}{2}}\right) = Be^{-j\frac{4\pi}{\lambda}r(t)}e^{-j\frac{\frac{2\pi}{\lambda}E(t)}{2}}2jsin\left(\frac{\pi E(t)}{\lambda}\right) \quad (5.9)$$

valid in the interval $[-T_e/2; +T_e/2 - d/2v_s]$, where B takes into account target reflectivity, transmitted power, antenna pattern and propagation loss, while $E(t)$ can be approximated by equation (5.10), (Gierull, 2006):

$$E(t) = 2r\left(t + \frac{d}{2v_s}\right) + u\left(t + \frac{d}{2v_s}\right)d - 2r(t) \cong \frac{v_y y_T d}{r_T v_s} \quad (5.10)$$

The detection of moving targets is based on the magnitude of DCPA output, given by equation (5.11), obtained by substituting (5.10) in (5.9):

$$|DPCA(t)| \cong 2|B|\left|sin\left(\frac{\pi}{\lambda}\frac{v_y y_T d}{r_T v_s}\right)\right| \quad (5.11)$$

It is important to observe that the argument of the sine depends only on the across-track velocity v_y of the target and does not depend on time t. By plotting the DPCA output amplitude as a function of the across-track velocity v_y, it is possible to note a notch-like filtering DPCA pattern around zero velocity. Additional ambiguous notches appear also at non-zero velocities, called blind velocities, because of array spatial sampling. Therefore, a moving target with zero across-track velocity and only an along-track velocity component is very attenuated by DPCA.

5.5. Along-Track Interferometry

Along-Track Interferometry (ATI) is a multi-aperture technique used for SAR moving target indication. As for DPCA, also ATI requires multiple antennas displaced in the along-track direction, which observe the same scene at different times. Considering a two-channel SAR system, the ATI signal is computed by multiplying the signal from one channel by the complex conjugate of the other channel, as in equation (5.12):

$$ATI(t) = s_1(t)s_2^*(t) = |s_1(t)||s_2(t)|e^{j[\phi_1(t)-\phi_2(t)]} \quad (5.12)$$

where $s_1(t)$ and $s_2(t)$ are the co-registered received signals, the symbol * means complex conjugation, and $\phi_1(t)$ and $\phi_2(t)$ are the phases of the two signals.

While a stationary target has zero ATI phase since the two signal phases $\phi_1(t)$ and $\phi_2(t)$ are identical, a moving target has a non-zero ATI phase, which is dependent on its motion. Therefore, it is possible to exploit ATI phase of the detected targets to estimate the across-track velocity.

ATI phase experiences several ambiguities, (Sharma, 2004), affecting target detection and velocity estimation (blind velocities), such as when the slant range variation of the moving target within the two channels is several times the operational wavelength, in a way that the ATI phase is out of the range $\pm\pi$ (a similar occurrence implied the necessity of phase unwrapping in the interferometric processing for the generation of Digital Elevation Models). In addition, Doppler ambiguities are induced due to finite azimuth bandwidth of the system.

Furthermore, ATI does not suppress clutter like DPCA, therefore the estimation of target velocity suffers of clutter contamination. A way to overcome this drawback is to perform ATI processing after clutter suppression through DPCA, but at least three channels are required (Fig. 5.4).

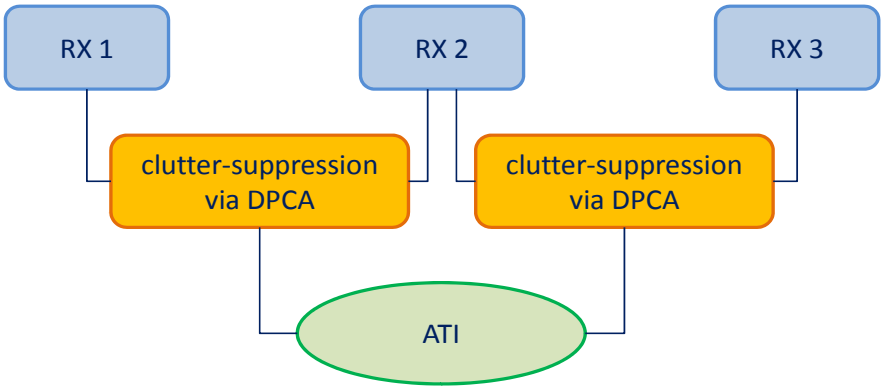

Fig. 5.4 – ATI performed in two clutter-suppressed images obtained through DPCA.

In current and next generation satellites, cost and technological constraints often limit the number of physical receiving chains up to two. Additional virtual channels can be achieved by a clever programming of the phased array antennas (the operational modes which use virtual channels are

called *toggle modes*). In toggle modes, (Chiu, 2006), pulses are transmitted exploiting the full antenna aperture and echoes are received varying the excitations of the antenna from pulse to pulse. Thus, in order to avoid ambiguities the operational PRF should be doubled, implying that the energy-per-pulse has to be reduced by the same amount in order to keep the same power consumption, and SNR decreases.

5.6. Target Detection and Velocity Estimation through DPCA and ATI

The moving target detection probability shall be maximized in accordance with a defined false alarm probability threshold, statistically characterized by the Probability Density Function (PDF) of the signal in the domain where the detection is performed, e.g. the magnitude of the DPCA output signal. Detectors with a fixed false alarm probability are called Constant False Alarm Rate (CFAR) detectors, (Golikov, et al., 2008).

DPCA and ATI techniques can be respectively implemented in a DPCA Constant False Alarm Rate (CFAR) detector and in an across-track velocity estimator, as in the following paragraphs, while to estimate the moving target along-track velocity a Fractional Fourier Transform (FrFT) can be applied.

5.6.1. CFAR DPCA Detector

After DPCA processing, in an ideal case of perfectly stationary clutter and no noise, the DPCA output is modeled as a complex Gaussian distribution, equation (5.13).

$$f_{DPCA}(DPCA) = \frac{1}{2\pi\sigma_D^2} e^{-\frac{1}{2\sigma_D^2}[\Re(DPCA)]^2+[\Im(DPCA)]^2} \tag{5.13}$$

where *DPCA* is the DPCA output, σ_D^2 is the variance of the real and imaginary parts, supposed uncorrelated, and $\Re(DPCA)$ and $\Im(DPCA)$ are respectively the real and imaginary parts.

The input of the CFAR DPCA detector is the magnitude of the DPCA signal, $A = |DPCA|$, modeled as a Rayleigh distribution because it is the absolute value of a complex Gaussian distributed signal.

$$f_A(A) = \frac{A}{\sigma_D^2} e^{-\frac{1}{2\sigma_D^2}A^2}, \qquad A \geq 0 \tag{5.14}$$

The *DPCA* magnitude has to be compared with a threshold η_{th}, which is set according to a defined false alarm probability P_{FA}.

$$P_{FA} = \int_{\eta_{th}}^{\infty} f_A(A)dA \tag{5.15}$$

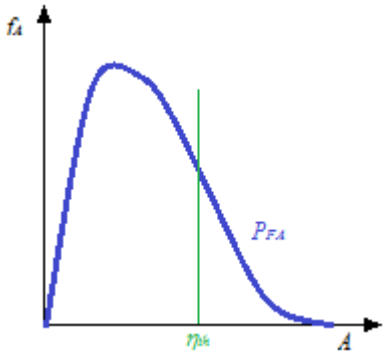

Fig. 5.5 – DPCA output signal magnitude, Rayleigh distribution
(ideal case of perfectly stationary clutter and no noise).

Other possible approaches of CFAR detection exist, based only on ATI phase, or both on ATI phase and magnitude (two-dimensional ATI detector if phase and magnitude are coupled, with a threshold described by a joint probability density), (Dong, 2010), (Chiu, 2005).

5.6.2. Velocity Estimation

A moving target across-track velocity induces an azimuth Doppler shift in the signal, while an along-track velocity affects the Doppler slope (i.e. azimuth frequency modulation rate). Generally, SAR processors consider a stationary scene and the targets are focused at their zero-Doppler position, through a Stationary World Matched Filter (SWMF) to perform azimuth compression. As a consequence of the Doppler shift, moving targets with non-zero across-track velocity are focused in a shifted azimuth position, while moving targets with non-zero along-track velocity are defocused and smeared due to the mismatch compared to the SWMF in terms of Doppler rate or slope. The estimation of target velocity vector also allows to adjust displacement and defocusing.
The estimation of the moving target across-track velocity v_y is based on the ATI phase. Assuming a SWMF, a zero-acceleration moving target and applying ATI equation (5.12), the ATI phase is given by (5.16).

$$\phi_{ATI} = \frac{2\pi}{\lambda}\frac{1}{2r_1} dy_1 v_y \left(\frac{1}{v_s} - \frac{v_x - v_s}{(v_x - v_s)^2 + v_y^2\left(1 - \frac{y_1^2}{r_1^2}\right)} \right) \tag{5.16}$$

where λ is the wavelength, d the distance between antenna phase centers, r_1 and y_1 respectively the range of closest approach and the distance target-nadir as in Fig. 5.1, and v_s the satellite velocity. The ATI phase can be approximated by equation (5.17), (C.E. Livingstone, 2002).

$$\phi_{ATI} \cong \frac{2\pi}{\lambda 2 r_1 v_s} dy_1 v_y \tag{5.17}$$

In this way, the across-track velocity v_y is directly proportional to the ATI phase, equation (5.18).

$$v_y = \frac{r_1 v_s \lambda}{\pi d y_1} \phi_{ATI} \tag{5.18}$$

The estimation of the along-track velocity v_x can be achieved through several approaches. A first approach consists in compressing the signal with a bank of filters matched to different along-track velocities, (Sharma, 2004), and maximizing the target response in the final image. This technique gives poor results because the along-track velocity is very small compared to the satellite velocity, and the output of the bank of filters is almost the same for the different velocities. A second approach is proposed in (Chiu, 2005), based on a Fractional Fourier Transform (FrFT) technique and on the transformation of the signal in a hybrid time-frequency domain, (Almeida, 1994). The FrFT, depending on a parameter α, can be considered as a rotation by an angle α in the time-frequency domain. The SAR signal is a linear chirp in the azimuth slow time domain. Exploiting this property, each target, fixed or moving, is characterized by a given rotation angle, and can be accordingly focused in an optimum Fractional domain. The FrFT is performed in range compressed but azimuth uncompressed SAR data, and also DPCA and ATI techniques can be applied to azimuth uncompressed data. The limited SNR of an uncompressed azimuth data is compensated by the FrFT capability to concentrate the moving target energy in few samples in the optimum Fractional domain, improving the SNR. With FrFT a good along-track velocity estimation is achieved. The optimum rotation angle α for a specific target is directly related to its Doppler slope k_a, and it is given by equation (5.19).

$$\alpha = atan\left(-\frac{PRF^2}{k_a N}\right) \tag{5.19}$$

where *PRF* is the pulse repetition frequency and *N* the analyzed number of samples of the signal. Finally, the along-track velocity v_x is estimated from the rotation angle α by equation (5.20).

$$v_x = v_s - \sqrt{\frac{r_1 \lambda PRF^2 cot\alpha}{2N} - v_y^2\left(1 - \frac{y_1^2}{r_1}\right)} \tag{5.20}$$

where the v_x depends also on the across-track velocity v_y, which shall be estimated first.

5.6.3. Algorithm for Dual Receive Antenna

An algorithm for moving target detection and velocity estimation for a Dual Receive Antenna is proposed in this paragraph, (Rizzato, 2012), and summarized in Fig. 5.6.

The two received signals have to be co-registered before DPCA.

The first two steps of the Range-Doppler focusing algorithm, range compression and range cell migration correction, are applied to the co-registered signals.

From these co-registered and range-compressed channels a single DPCA image is generated.

In order to preserve all the energy of the moving targets, the detection is performed over the azimuth uncompressed signals, because a SWMF can defocus the targets.

Each azimuth line, i.e. vector of all azimuth samples, of the DPCA output image is transformed into a specific Fractional domain, which is given, for each azimuth line, by a peak of maximum magnitude obtained by varying the rotation angle α. This specific Fractional domain is associated with an optimum rotation angle $\alpha_{\mathrm{opt,i}}$, where i refers to the different range lines. It is assumed that only a single moving target exists for each azimuth line, therefore the optimum rotation angle $\alpha_{\mathrm{opt,i}}$ is achieved by looking for only one maximum peak.

The peak magnitude value is compared with a threshold η_{th} for a CFAR detection. If the peak magnitude exceeds the threshold, a moving target is detected. The value of the azimuth line rg_i where the moving target is detected, the optimum rotation angle $\alpha_{opt,i}$ and the peak position $u_{p,i}$ in the Fractional domain are used also to perform velocity estimation.

In order to estimate the moving target velocity vector, first it is computed the across-track velocity component and after the along-track one.

The signal before the DPCA, which is range compressed, azimuth uncompressed and co-registered, for every azimuth line rg_i and for both channels, is transformed into the Fractional domain using the optimal rotation angle $\alpha_{opt,i}$ obtained during the previous detection phase.

The peaks for both channels will be exactly in the $u_{p,i}$ position. Since the original signals have still clutter and noise, the peaks extraction is performed through bandpass filtering using as a filter an ideal rectangular single-sample window centered at $u_{p,i}$ position and zero elsewhere.

By applying an inverse FrFT, two clutter suppressed moving targets filtered signals are reconstructed. From these signals an interferogram can be generated, and from the ATI phase, through the equation (5.18), it is possible to estimate the across-track velocity v_y.

Finally, the along-track velocity v_x is estimated through the equation (5.20), using v_y value and the optimum rotation angle α_{opt} found during the detection phase.

As previously described, the detection is performed in the Fractional Fourier time-frequency hybrid domain after DPCA processing. An important step is the selection of the detection threshold η_{th}. Assuming that, as in the time domain, also in the Fractional domain the signal magnitude A after DPCA is characterized by a Rayleigh distribution, equation (5.21), the parameter σ^2 can be estimated from samples a_i in the Fractional domain by equation (5.22), (J. Sijbers, 1999).

$$f_A(A) = \frac{A}{\sigma^2} e^{-\frac{1}{2\sigma^2}A^2}, \qquad A \geq 0 \tag{5.21}$$

$$\sigma^2 \approx \frac{1}{2N} \sum_{i=1}^{N} a_i^2 \tag{5.22}$$

The threshold η_{th} can be computed, according to a defined false alarm probability, by numerically solving the equation (5.23).

$$P_{FA} = \int_{\eta_{th}}^{\infty} f_A(A) dA \tag{5.23}$$

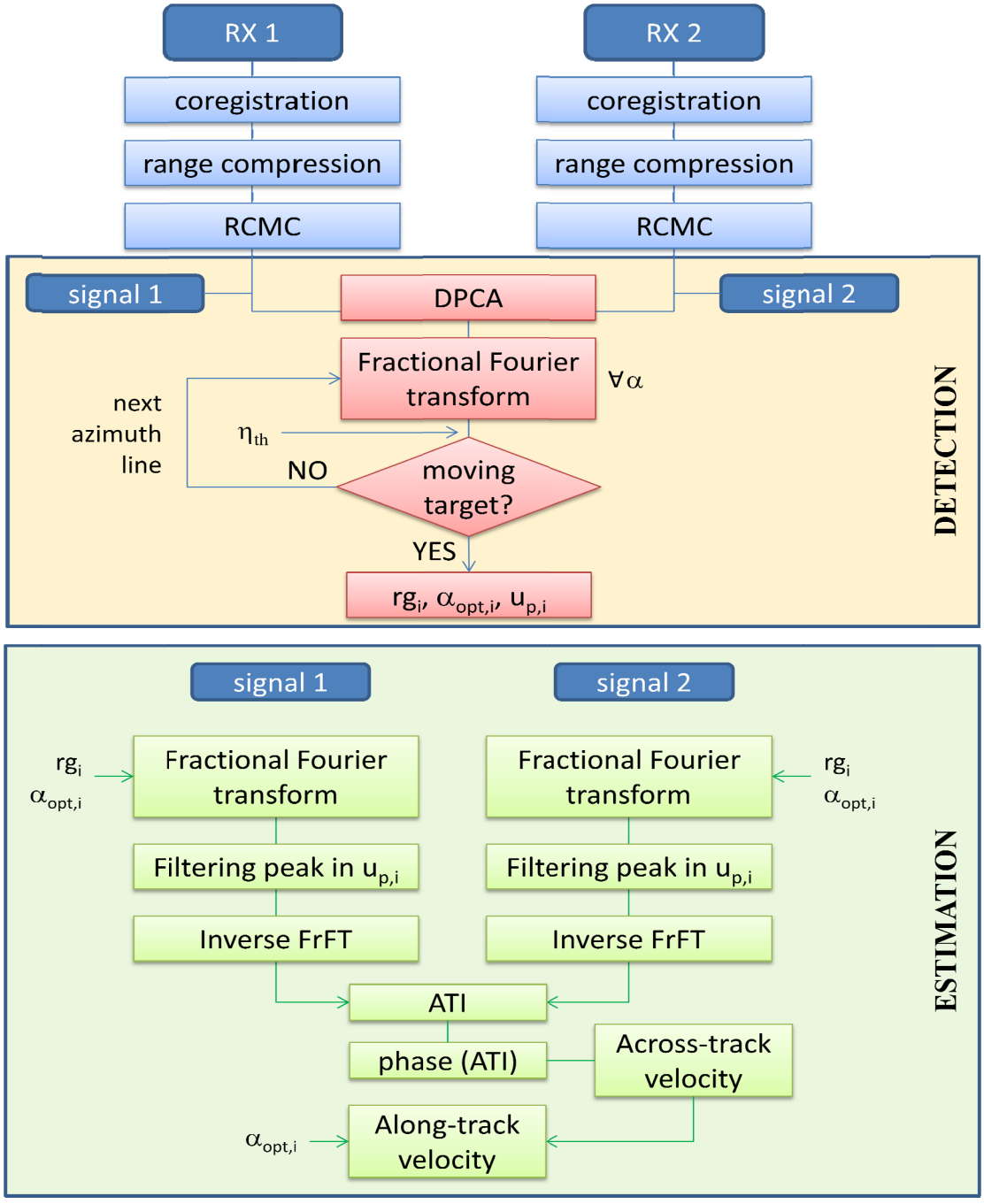

Fig. 5.6 – Moving target detection and velocity estimation algorithm for Dual Receive Antenna.

5.7. Ship Monitoring from TanDEM-X and TerraSAR-X satellites

The above considerations are applicable for instance to TerraSAR-X Dual Receive Antenna mode (S. Suchandt, 2010), which splits the antenna in two halves and records the signals of both with separate electronics. Some additional consideration has to be done for TanDEM-X and TerraSAR-X satellites, which fly with an across-track and along-track separation which varies along each orbit in a Helix configuration, with two separate antenna channels on each platform, providing a total of four receiving channels.

By choosing the along-track baseline between the satellites in the order of several kilometers (time delay of few seconds), the moving targets are observed from the two satellites at different times, and the displacements of the moving targets in the two SAR images will be different due to time delay and target motion. In (S. Baumgartner, 2007), an optimal time delay giving the best performance is estimated to be approximately 2.5 seconds, corresponding to an along-track baseline in the order of 20 km. Each satellite is operated in a Dual Receive Antenna mode in order to enable the application of DPCA technique for clutter suppression. By estimating the relative target displacements between both clutter suppressed DPCA images, it is possible to derive the moving targets motion parameters.

5.7.1. Mathematical Approach

According to Fig. 5.7, where the Cartesian acquisition geometry should be extended to a spherical one to take into account also the approximately circular flight orbits of the satellites, the SAR platform moves with constant velocity v_s in the along-track direction, (S. Baumgartner, 2007).

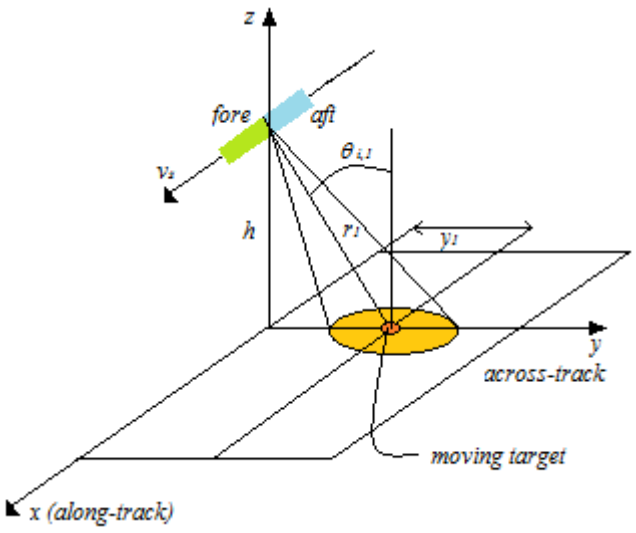

Fig. 5.7 – Two-channel SAR geometry.

At time $t = 0$, the moving target is located at $x = x_1 = 0$, $y = y_1$ and $z = 0$, having an instantaneous along-track velocity v_{x1} and acceleration a_x, an instantaneous across-track velocity v_{y1} and acceleration a_y. It is assumed that target does not move in z-direction and the acceleration components remain constant in time.

The along-track displacement Δx_1 of the moving target after SAR processing, for non-squinted and Nyquist sampled case is given by, (V.C. Chen, 2002):

$$\Delta x_1 \cong -v_s \frac{f_{DC,1}}{k_{a,1}} \tag{5.24}$$

where $f_{DC,1}$ is the Doppler shift and $k_{a,1}$ is the Doppler slope of the received moving target signal. Considering that $v_s >> v_{x1}$, v_{y1} and the observation time is in the order of only one second, Doppler shift and Doppler slope can be approximated by equation (5.25).

$$\begin{aligned} f_{DC,1} &\cong -\frac{2}{\lambda}\frac{y_1}{r_1}v_{y1} = -\frac{2}{\lambda}v_{y1}sin\theta_{i,1} \\ k_{a,1} &\cong -\frac{2}{\lambda r_1}\left[(v_s - v_{x1})^2 + y_1 a_y\right] \end{aligned} \tag{5.25}$$

where r_1 is the slant range distance at $t = 0$, $y_1$the across-track distance at $t = 0$, $\theta_{i,1}$ the incidence angle and λ the radar wavelength, as in Fig. 5.7.

The across-track displacement Δy_1 of the moving target, due to the same chirp scaling processing of the stationary case, is given by equation (5.26):

$$\Delta y_1 \cong \frac{\Delta x_1}{2v_s}v_{y1} = \frac{1}{\lambda k_{a,1}}\frac{y_1}{r_1}v_{y1}^2 = \frac{sin\theta_{i,1}}{\lambda k_{a,1}}v_{y1}^2 \tag{5.26}$$

Considering a second radar platform, it is assumed to be displaced of d_a from the first one only in the along-track direction, Fig. 5.8. This strong assumption will be removed in Par. 5.7.3.

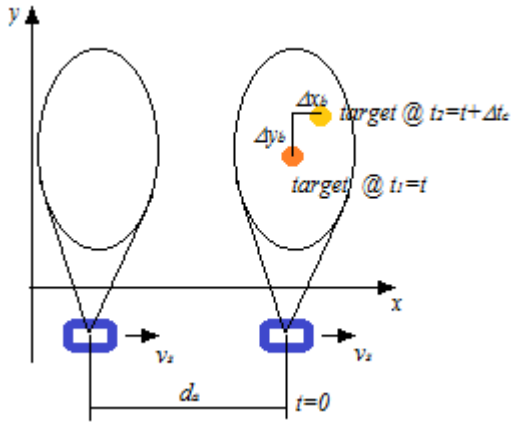

Fig. 5.8 – Along-track configuration.

Data acquired from the first and from the second platform have to be coregistered, with respect to stationary targets, by applying a time shift of $\Delta t_c = -{}^{d_a}/_{v_s}$. Assuming that at $t = 0$ the moving target is at broadside of the first platform, after a time delay of $\Delta t_b = {}^{d_a}/_{(v_s - \bar{v}_x)}$ it is at broadside of the second platform, where $\bar{v}_x$ is the average along-track velocity of the moving target during the time interval Δt_b. Since $v_s >> \bar{v}_x$ and in most practical cases the moving target does not travel through one full azimuth resolution cell during Δt_c, then $|\Delta t_c| \cong |\Delta t_b|$ is assumed.

During Δt_c the moving target travels on ground the distances in (5.27).

$$\begin{aligned} \Delta x_b &= v_{x1}\Delta t_c + \frac{1}{2}a_x{\Delta t_c}^2 = \bar{v}_x \Delta t_c \\ \Delta y_b &= v_{y1}\Delta t_c + \frac{1}{2}a_y{\Delta t_c}^2 = \bar{v}_y \Delta t_c \end{aligned} \tag{5.27}$$

where the distances actually travelled by the target on ground, Δx_b and Δy_b, do not coincide with the relative moving target displacements Δx_{img} and Δy_{img} in the focused SAR images.

The moving target relative along-track displacement Δx_{img} between the two coregistered and focused SAR or DPCA images can be expressed as in (5.28).

$$\Delta x_{img} = \Delta x_2 - \Delta x_1 = -v_s \frac{f_{DC,2}}{k_{a,2}} + \Delta x_b + v_s \frac{f_{DC,1}}{k_{a,1}} \tag{5.28}$$

where the index '2' indicates the moving target when it is at broadside of the second platform.

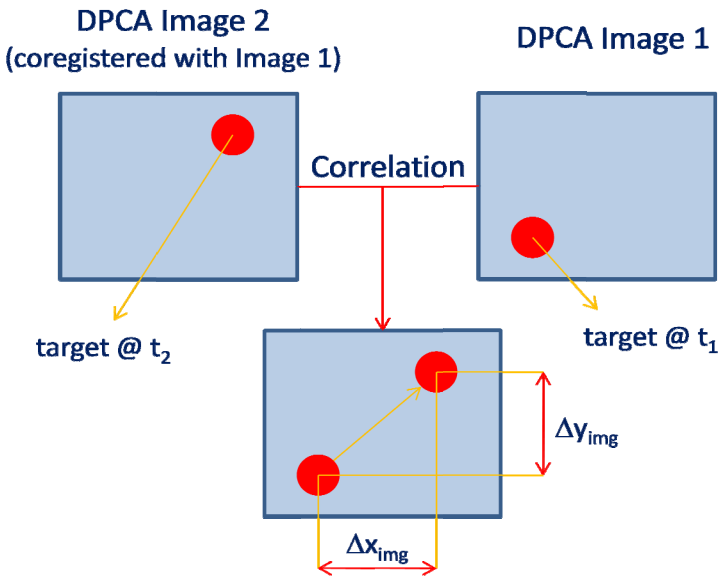

Fig. 5.9 – Relative target displacement in SAR or DPCA image domain, each DPCA image is obtained from each Dual Receive Antenna, the correlation between the DPCA images is very simple.

Assuming that the along-track baseline between the two antennas corresponds to a time delay of only few seconds, the incidence angle θ_i and the Doppler slope k_a of the moving target signal does not change significantly between the two acquisitions, and the approximations in equation (5.29) are valid:

$$k_{a,1} \cong k_{a,2} = k_a \quad and \quad \theta_{i,1} \cong \theta_{i,2} = \theta_i \tag{5.29}$$

Thus, moving target relative along-track and across-track displacements are given by eq. (5.30).

$$\begin{aligned} \Delta x_{img} &\cong v_s \frac{2sin\theta_{i,1}}{\lambda k_{a,1}} a_y \Delta t_b + \Delta x_b = \Delta x_{img,ay} + \Delta x_b \\ \Delta y_{img} &= \Delta y_2 - \Delta y_1 \cong \frac{sin\theta_{i,1}}{\lambda k_{a,1}} \Delta t_b (2 v_{y1} a_y + a_y^2 \Delta t_b) + \Delta y_b \end{aligned} \tag{5.30}$$

The displacement $\Delta x_{img,ay}$ caused by the moving target across-track acceleration a_y may be quite larger than the distance Δx_b traveled by the target during the interval Δt_b.

The first term of the relative across-track displacement Δy_{img} in the second equation (5.30) is in the order of one across-track resolution cell in most practical cases for TerraSAR-X and TanDEM-X, (S. Baumgartner, 2006), thus:

$$\Delta y_{img} \cong \Delta y_b \tag{5.31}$$

5.7.2. Velocity Estimation Technique

By applying DPCA technique both for TerraSAR-X and TanDEM-X, two independent clutter suppressed DPCA images are achieved. If the moving target is detected at least in one DPCA image, it is possible to estimate its Doppler slope $k_{a,1}$ through a matched filter bank or the FrFT (see par. 5.6.2) in order to refocus and increase the signal-to-clutter plus noise ratio (SCNR) of both DPCA images, based on the assumption $k_{a,1} \cong k_{a,2}$ in (5.29). Consequently, through a two-dimensional correlation process, it is possible to obtain the moving target relative displacements Δx_{img} and Δy_{img}, Fig. 5.9, which will allow to estimate the moving target velocity.

Since the moving target relative along-track displacement Δx_{img}, equation (5.30), is mainly affected by the product $a_y \Delta t_b$, a change in the Doppler slope $k_{a,1}$ of several *Hz* caused by a moving target does not change its value significantly. Therefore, by using with a good approximation the Doppler slope of a stationary target, from the first equation (5.30) an estimate of the moving target along-track displacement $\Delta \hat{x}_{img}$ is given by equation (5.32):

$$\Delta \hat{x}_{img} \cong -\frac{r_1 sin\theta_{i,1}}{v_s} \hat{a}_y \Delta t_b + \hat{\bar{v}}_x \Delta t_b \tag{5.32}$$

From equation (5.32), an estimate of the average along-track velocity $\hat{\bar{v}}_x$ can be obtained, where Δx_{img} was previously computed:

$$\hat{\bar{v}}_x = \frac{\Delta \hat{x}_{img}}{\Delta t_b} + \frac{r_1 sin\theta_{i,1}}{v_s} \hat{a}_y \tag{5.33}$$

To obtain an estimate of the across-track acceleration $\hat{a}_y$, equation (5.33) can be replaced in the Doppler slope equation (5.25), neglecting the small difference between $\bar{v}_x$ and v_{x1} compared to the product $y_1 a_y$, giving:

$$\hat{a}_y^2 + \hat{a}_y p + q = 0 \tag{5.34}$$

where:

$$\begin{aligned} p &= (2AB - 2Bv_s + y_1)\frac{1}{B^2} \\ q &= \left[(A - v_s)^2 + \frac{\lambda r_1 k_{a,1}}{2}\right]\frac{1}{B^2} \end{aligned} \tag{5.35}$$

with:

$$A = \frac{\Delta \hat{x}_{img}}{\Delta t_b}, \quad B = \frac{r_1 sin\theta_{i,1}}{v_s} \tag{5.36}$$

The only solution of physical relevance of equation (5.34) is given by (5.37).

$$\hat{a}_y = -\frac{p}{2} - \sqrt{\left(\frac{p}{2}\right)^2 - q} \tag{5.37}$$

To estimate the moving target across-track velocity, the following relation can be obtained from the second equation (5.27) and (5.31), where Δy_{img} was previously computed:

$$\hat{v}_{y1} = \frac{\Delta \hat{y}_{img}}{\Delta t_b} - \frac{1}{2}\hat{a}_y \Delta t_b \tag{5.38}$$

The along-track velocity estimate can be obtained from the second equation (5.25):

$$\hat{v}_{x1} = v_s - \sqrt{-\hat{k}_{a,1}\frac{\lambda r_1}{2} - y_1 \hat{a}_y} \tag{5.39}$$

The along-track acceleration estimate can be obtained from the first equation (5.27):

$$\hat{a}_x = \frac{2}{{\Delta t_b}^2}(\Delta \hat{x}_b - \hat{v}_{x1}\Delta t_b) \tag{5.40}$$

Where the along-track distance traveled by the target $\Delta \hat{x}_b$ is computed from equation (5.30):

$$\Delta\hat{x}_b = \Delta\hat{x}_{img} - v_s \frac{2sin\theta_{i,1}}{\lambda \hat{k}_{a,1}} \hat{a}_y \Delta t_b \tag{5.41}$$

Finally, the moving target repositioning values in along-track and across-track directions for image 1 can be computed from equation (5.24) and (5.25):

$$\begin{aligned} \Delta\hat{x}_{1,redisp} &= -\Delta\hat{x}_1 \cong -\frac{2v_s sin\theta_{i,1}}{\lambda \hat{k}_{a,1}} \hat{v}_{y1} \\ \Delta\hat{y}_{1,redisp} &= -\Delta\hat{y}_1 \cong -\frac{sin\theta_{i,1}}{\lambda \hat{k}_{a,1}} \hat{v}_{y1}{}^2 \end{aligned} \tag{5.42}$$

5.7.3. Discussion

Moving targets in conventional SAR images appear displaced from their true positions, with large and small displacements respectively in the azimuth and range direction, because of the Doppler shift due to moving target across-track velocity, and blurred in azimuth direction because of the moving target along-track velocity and across-track acceleration.

For a single platform with two phase centers, it is possible to achieve a small along-track baseline due to the short extension of the SAR antenna in flight direction, with time delays in the order of the *millisecond*, and very low target motion sensitivity:

$$\phi_{ATI} = \frac{4\pi d sin\theta}{\lambda v_s} v_y \tag{5.43}$$

where d is the along-track baseline between the two antenna sub-apertures and θ is the local incidence angle, as in (5.17). In this way, it is possible to estimate only very fast movements.

With longer baselines, allowed by two SAR platforms like TanDEM-X and TerraSAR-X flying in close proximity, time delays are in the order of the *second*, and it is possible to reduce the minimum detectable velocity and achieve higher sensitivities to measure target motions, while on the other hand very long along-track baselines increase the variety of blind velocities due to phase wrapping, (C. Schaefer, 2008). This last issue can be overcome by additional splitting of the SAR antenna for each satellite, allowing multiple ATI baselines and consequently reducing blind velocities and enabling clutter suppression through DPCA.

The processing steps can be summarized as:

1. Clutter suppression and detection through DPCA technique ($v_y \neq 0$);
2. 2D cross-correlation to estimate the relative displacements in along and across-track direction;
3. Once the target is detected, its Doppler slope can be estimated and the moving target images can be refocused for increasing the SCNR;

4. Estimation of the true geographical position and velocity vector for each detected moving target.

The above approach is based two platforms displaced of d_a only in the along-track direction, without any across-track baseline component. In the general case, it is necessary to take into account an hybrid baseline composed by an along-track and also an across-track component, and the extraction of target motion information is also challenging because of the need to compensate the across-track baseline component, (S. Suchandt, 2012). In the literature, two main approaches are suggested to remove the across-track effect from the hybrid interferogram. The first one consists in deriving from a very high accuracy Digital Elevation Model (DEM) on the area of interest an across-track phase according to the satellite acquisition geometry, which shall be subtracted from the interferogram. In this case, the results is highly dependent on the DEM accuracy, which shall reproduce even small features, otherwise the phase contribution due for instance to buildings can be mistakenly interpreted as motion. A second approach suggests to estimate along-track phase from the hybrid wrapped interferogram after removal of the flat earth phase, (L. Yang, 2008). According to this technique, based on the consideration that small moving targets cause point-like phase alterations of the interferogram while, for flat terrain, across-track phase varies locally only slowly, it is possible to estimate the along-track phase $\hat{\phi}_{ATI}$ in a certain position by subtracting an estimate of the local across-track (topographic) phase $\hat{\phi}_{XTI}$ computed as an average of the interferogram phase in the neighboring points.

$$\phi_{ATI} = arg\left\{\underline{I} \cdot e^{-j\hat{\phi}_{XTI}} \cdot e^{-j\phi_{flat}}\right\}$$
$$\phi_{XTI}(m,n) = \frac{1}{w^2} \sum_{k=m-w/2}^{m+w/2} \sum_{l=n-w/2}^{n+w/2} arg\left\{\underline{I}(k,l) \cdot e^{-j\phi_{flat}(k,l)}\right\} \tag{5.44}$$

where $\underline{I}$, ϕ_{flat}, (m,n) and w represent respectively the hybrid interferogram, the flat earth phase, the pixel position and the size of the analysis window, which shall be large enough compared to the moving target size in order to do not compensate also its along-track phase. Also the application of a filter is suggested in order to exclude the moving target position and the outliers among all the values in the window. Furthermore, in order to avoid technique failure due to low coherence over sea or to sea surface motion seen as a distributed moving target, the sea surface at a first approximation and after removal of the flat Earth phase can be considered flat compared with across-track phase, so across-track phase component over the sea can be compensated considering the phase estimate taken at the coastlines. The effectiveness of this approach should be experimented on real data especially over the sea, which represents a very challenging scenario for

across-track baseline component compensation, also because even if the flat approximation over the sea can be assumed, the effects of the sea motion should be properly investigated.

The estimated across-track phase, together with the flat earth contribution, shall be used also to compensate the phase in the master single-look complex (SLC) image in input to DPCA for clutter suppression, $\underline{S} \cdot e^{-j\widehat{\phi}_{XTI}} \cdot e^{-j\phi_{flat}}$, before subtracting the slave SLC image.

After the hybrid interferogram compensation for the across-track phase component, it is possible to correlate target motion to the interferogram phase. A constant ship translational motion causes a constant phase offset. Fringes may be induced by a ship rotation, in particular a roll rotation (around azimuth) causes range fringes, a yaw rotation (around zenith) and a pitch rotation (around ground range) cause azimuth fringes.

Classical Commercial-On-The-Shelf (COTS) software packages such as ENVI 4.8, SARscape 4.4, ERDAS IMAGINE 2011, SOCET GXP 3.2.0 and Next ESA SAR Toolbox (NEST) 4C-1.1 currently do not implement DPCA or ATI, but may help in some basic processing step such as coregistration, filtering, FFT. In particular, NEST implements a Two-Parameter CFAR Detector for ship detection and also allows to estimate and subtract the topographic phase from an interferogram, given an high accuracy input DEM, which may be useful for across-track baseline component compensation.

CONCLUSIONS

In this Thesis, several state-of-the-art and innovative techniques for Digital Elevation Model (DEM) generation from Synthetic Aperture Radar (SAR) images, both based on phase and amplitude information, were deeply analyzed, focusing on the methods which allow the improvement of the accuracy of the DEM product.

The availability of high accuracy DEM products is directly related to the geolocation accuracy of geocoded images and it is considered as an enabling factor for a large series of civilian and Defence applications, such as topography, air and surface based weapon system navigation, 3D visualization; go/no-go route planning based on slope assessment, cross-country movement and trafficability analysis, intelligence preparation of the battle-space, improved crisis intervention planning, modeling and simulation, 3D flight mission planning and simulation (aircrafts, missiles, etc), line-of-sight analysis, electromagnetic propagation analysis for telecommunication applications, etc.

Some of the proposed techniques were experimented on real data, i.e. COSMO-SkyMed (CSK) data, assessing the achievable performances compared with the state-of-the-art, pointing out and quantitatively highlighting the acquisition and processing strategies which would allow to maximize the quality of the results, and performing a critical analysis about the main errors affecting the applied techniques, as well as the limitations of the orbital configurations, identifying several complementary techniques which would allow to overcome or mitigate the observed drawbacks.

In particular, in Chapter 1 the main concepts concerning SAR operating principles were introduced and the main characteristics and performances of CSK and TDX satellite systems were described.

In Chapter 2 a review was proposed about the state-of-the-art SAR interferometric techniques for DEM generation, analyzing all the relevant processing steps and deepening the study of the main solutions recently proposed in the literature to increase the accuracy of the interferometric processing.

In Chapter 3 several complementary and innovative techniques respect to the interferometric processing were analyzed, such as the multi-chromatic approach to SAR interferometry and the delta-k technique, which allow to skip the error-prone phase unwrapping processing step; or the wavelet-based DEM fusion, which allows to take advantage of the specific frequency trend of the atmospheric distortions to estimate and properly weight the noise and atmospheric distortion power from each interferogram and improve the DEM accuracy; or permanent scatterers interferometry and SqueeSAR techniques, which allow to overcome several limitations of SAR interferometry and to obtain high accuracies over very stable scatterers through a huge number of SAR images, but voids filling has to

be properly taken into account; or radargrammetry, which is based on amplitude data and it is not affected by the main error sources related to the phase. These techniques can be applied in place of specific interferometric processing steps in order to increase the DEM accuracy or can concern the combination of complementary techniques to mitigate mutual disadvantages and to improve the overall performances.

In Chapter 4 experimental results were presented, obtained in the generation of high accuracy DEM by applying to a dataset of CSK images properly selected state-of-the-art interferometric techniques and innovative methods to improve DEM accuracy, exploring relevant limitations, and pointing out innovative acquisition and processing strategies.

The performed analysis allowed to explore the interferometric capabilities of CSK constellation for DEM generation, and several test cases were studied on a single scenario where ground truths were available for quality check and validation purposes. Even if a more extensive experimental campaign would be necessary if DEM quality certification aims wanted to be pursued, the results of the performed analysis are sufficient to understand the potentialities of CSK constellation for DEM generation according to the proposed operational concept, focused on the capability to quickly generate on-demand a very high accuracy DEM on a specific selected area. These results allowed to state that the DEM which is possible to generate from CSK data can be compliant with HREGP NGA standard, with accuracies between HREGP and HRE-80 quality levels, which entail a contribution to the geolocation accuracy of geocoded images using the generated DEM lower than 10 m for high incidence angles. If ground truths for quality check and validation purposes were available, the study can be further extended to more challenging topographies.

Furthermore, a theoretical error study and an experimental sensitivity analysis was performed based on CSK data in order to understand the dependencies of DEM accuracy on several relevant parameters such as normal baseline length, coregistration accuracy (DEM-assisted or not), usage of calibration GCP during processing and application of CBF.

In addition, a trade-off analysis was performed to quantitatively understand if it is possible to achieve improvements in the DEM final accuracy through a proper interferometric processing or other ad-hoc techniques. In particular, an analysis of the improvement of the DEM accuracy through a combination of acquisitions on the same site from ascending and descending passages was performed, in order to solve part of the errors introduced by shadowing and layover effects. Also a wavelet-based fusion between the generated DEM and a low resolution SRTM DEM was performed in order to mitigate the atmospheric disturbances at low frequencies due to the repeat-pass interferometry, through the injection of the low spatial frequencies of the low accuracy SRTM DEM, preserving the high spatial frequencies and details information of the DEM generated from CSK.

A critical analysis was performed also in relation to all the factors and parameters which limit the achievable performances in DEM generation.

Based on the obtained results and on the consequent critical analysis, several interferometric specifications for new generation SAR satellites were identified.

Moreover, an innovative procedure for on-demand DEM production from CSK SAR data was elaborated and proposed, fulfilling the proposed operational concept. An innovative DEM auto-validation method was also introduced and it is under review, to perform a quality analysis of a generated DEM even without vertical ground truths.

In Chapter 5, a literature review was proposed about the main state-of-the-art ship monitoring techniques, considered as one of the main fields of application, together with DEM generation, which takes benefit from SAR data, based on single/multi-platform multi-channel SAR data. In particular, the basic principles of Ground Moving Target Indication (GMTI) were described, focusing on Displaced Phase Center Antenna (DPCA) and Along-Track Interferometry (ATI) techniques, and analyzing how target detection and velocity estimation can be performed, with a focus on TanDEM-X (TDX) data.

BIBLIOGRAPHY

CHAPTER 1

Krieger G., Zink M. and Moreira A. TanDEM-X: a Radar Interferometer with two Formation Flying Satellites. 63rd International Astronautical Congress (IAC), 2012. - p. 12 pp.. - IAC-12-B4.7B.3.

Rizzato D. Techniques for ground moving target detection and velocity estimation with multi-channel Synthetic Aperture Radars (SAR). - University of Padova : Master Thesis, 2012.

CHAPTER 2

National Imagery and Mapping Agency (NIMA) Performance Specification Digital Terrain Elevation Data (DTED) // MIL-PRF-89020B. - 2000.

Bamler R. and Hartl P. Synthetic aperture radar interferometry. Inverse Problems, 1998. - Vol. 14. - pp. R1-R54.

Chen C.W. and Zebker H.A. Network approaches to two-dimensional phase unwrapping: intractability and two new algorithms. Journal of the Optical Society of America A, 2000. - Vol. 17. - pp. 401-414.

Costantini M. A novel phase unwrapping method based on network programming. IEEE Transactions on Geoscience and Remote Sensing, 1998. - Vol. 36. - pp. 813 – 821.

Curlander J.C. and McDonough R.N. Synthetic aperture radar: systems and signal processing. John Wiley & Sons, 1991.

Curlander J.C. Location of Spaceborne SAR Imagery. IEEE Transactions on Geoscience and Remote Sensing, 1982. - Vols. GE-20. - pp. 359-364.

Ferretti A. [et al.] InSAR Principles: Guidelines for SAR Interferometry Processing and Interpretation. ESA Publications, 2007. - ISSN: 1013-7076.

Ferretti A. [et al.] Multibaseline SAR interferometry for automatic DEM reconstruction. Proceedings of the III ERS Symposium, 1997. - pp. 1809-1820. - ESA SP-414.

Fornaro G. and Monti Guarnieri A. Minimum Mean Square Error Space-Varying Filtering Of Interferometric SAR Data. IEEE Transactions on Geoscience and Remote Sensing, 2001. - Vol. 39.

Gatelli F. [et al.] The wavenumber shift in SAR interferometry. IEEE Transactions on Geoscience and Remote Sensing, 1994. - Vol. 32. - pp. 855-865.

Ghiglia D.C and Romero L.A. Minimum Lp-norm two-dimensional phase unwrapping. Journal of the Optical Society of America A, 1996. - Vol. 13. - pp. 1-15.

Goldstein R., Zebker H. and Werner C. Satellite radar interferometry: two dimensional phase unwrapping. Radio Science, 1988. - Vol. 23. - pp. 713 – 720.

Hanssen R. Assessment of the role of Atmospheric heterogeneities in ERS Tandem SAR interferometry. Delft University Press, 1998.

Kramer R. and Loffeld O. Presentation of an improved Phase Unwrapping Algorithm based on Kalman filters combined with local slope estimation. Proceedings of the Fringe 1996 Workshop, 1996. - pp. 253-260. - ESA SP-406.

Li F. K. and Goldstein R. M. Studies of multibaseline spaceborne interferometric synthetic aperture radars. IEEE Transactions on Geoscience and Remote Sensing, 1990. - Vol. 28. - pp. 88-97.

Moreira A. and Schreiber R. Coregistration of interferometric SAR images using spectral diversity. IEEE Transactions on Geoscience and Remote Sensing, 2000. - Vol. 38. - pp. 2179-2191.

National Geospatial-Intelligence Agency "Implementation Profile for High Resolution Elevation (HRE) products" [Report]. - 2009. - NGA.IP.0002_1.0.

Nitti D.O. [et al.] Impact of DEM-Assisted Coregistration on High-Resolution SAR Interferometry. IEEE Transactions on Geoscience and Remote Sensing, 2011. - Vol. 49. - pp. 1127-1143.

Schreier G. SAR Geocoding: data and systems. Wichmann Verlag, 1993.

Small D., Pasquali P. and Fuglistaler S. A Comparison of Phase to Height Conversion Methods for SAR Interferometry. Proceedings of IEEE International Geoscience and Remote Sensing Symposium 1996, 1996. - pp. 342-344.

Spagnolini U. 2-D phase unwrapping and instantaneous frequency estimation. IEEE Transactions on Geoscience and Remote Sensing, 1995. - Vol. 33. - pp. 579-589.

Strang G. and Borre K. Linear Algebra, Geodesy and GPS. Wellesley-Cambridge Press, 1997.

Touzi R. [et al.] Coherence estimation for SAR imagery. IEEE Transactions on Geoscience and Remote Sensing, 1999. - Vol. 37. - pp. 135-149.

Wackernagel H. Multivariate Geostatistics - II Edition. Springer-Verlang, 1998.

Xu W. and Cumming I. A Region-Growing Algorithm for InSAR Phase Unwrapping. IEEE Transactions on Geoscience and Remote Sensing, 1999. - Vol. 37. - pp. 124-134.

Zebker H. A. and Goldstein R. M. Topographic mapping from interferometric synthetic aperture radar observations. Journal of Geophysical Research, 1986. - Vol. 91. - pp. 4993-4999.

CHAPTER 3

Bamler R. and Eineder M. Accuracy of Differential Shift Estimation by Correlation and Split-Bandwidth Interferometry for Wideband and Delta-k SAR Systems. IEEE Geoscience and Remote Sensing Letters, 2005. - Vol. 2. - pp. 151–155.

Bovenga F. [et al.] Interferometric Multi-Chromatic Analysis of TerraSAR-X Data. - DLR-Oberpfaffenhofen, Germany : TerraSAR-X Science Team Meeting, 2011.

Brcic R., Eineder M. and Bamler R. Absolute Phase Estimation from TerraSAR-X Acquisitions using Wideband Interferometry. - Oberpfaffenhofen : Proceedings of TerraSAR-X Science Team Meeting, 2008.

Chen P.H. and Dowman I.J. A weighted least squares solution for space intersection of spaceborne stereo SAR data. IEEE Transactions on Geoscience and Remote Sensing, 2001. - Vol. 39. - pp. 233 - 240.

Denos M. A pyramidal scheme for stereo matching SIR-B imagery. International Journal of Remote Sensing, 1992. - Vol. 13. - pp. 387 - 392.

Ferretti A. [et al.] A New Algorithm for Processing Interferometric Data-Stacks: SqueeSAR. IEEE Transactions on Geoscience and Remote Sensing, 2011. - Vol. 49. - pp. 3460-3470.

Ferretti A. [et al.] InSARr Principles: Guidelines for SAR Interferometry Processing and Interpretation. ESA Publications, 2007. - ISSN: 1013-7076.

Ferretti A., Prati C. and Rocca F. Multibaseline InSAR DEM Reconstruction: The Wavelet Approach. IEEE Transactions on Geoscience and Remote Sensing, 1999. - Vol. 37.

Ferretti A., Prati C. and Rocca F. Permanent Scatterers in SAR Interferometry. IEEE Transactions on Geoscience and Remote Sensing, 2001. - Vol. 39. - pp. 8-20.

Grohman G., Kroenung G. and Strebeck J. Filling SRTM voids: the delta surface fill method. Photogrammetric Engineering and Remote Sensing, 2006. - Vol. 72. - pp. 213–216.

Jehle M. [et al.] Estimation of Atmospheric Path Delays in TerraSAR-X Data using Models versus Measurements. Sensors, 2008. - Vol. 8. - pp. 8479-8491.

Leberl F. Radargrammetric image processing. - Norwood, MA : Artech House, 1990.

Luedeling E., Siebert S. and Buerkert A. Filling the voids in the SRTM elevation model - a TIN-based delta surface approach. ISPRS Journal of Photogrammetry and Remote Sensing, 2007. - Vol. 62. - pp. 283–294.

Meric S., Fayard F. and Pottier E. Radargrammetry improvements: a multiwindow approach. 8th European Conference on Synthetic Aperture Radar (EUSAR), 2010. - pp. 1-4.

Reuter H.I., Nelson A. and Jarvis A. An evaluation of void-filling interpolation methods for SRTM data. International Journal of Geographical Information Science, 2007. - Vol. 21. - pp. 983–1008.

Schubert A [et al.] Influence of atmospheric path delay on the absolute geolocation accuracy of TerraSAR-X high-resolution products. IEEE Transactions on Geoscience and Remote Sensing, 2010. - Vol. 48. - pp. 751-758.

Solheim F. S. [et al.] Propagation delays induced in GPS signals by dry air, water vapor, hydrometeors, and other particulates. Journal of Geophysical Research: Atmospheres , 1999. - Vol. 104. - pp. 9663–9670.

Stephens M. A. Use of the Kolmogorov-Smirnov, Cramér-Von Mises and related statistics without extensive tables. J. R. Stat. Soc. Ser. B (Methodological), 1970. - Vol. 32. - pp. 115–122.

Tupin F. and Nicolas J.-M. Matching criteria for radargrammetry. IEEE International Geoscience and Remote Sensing Symposium, 2002. - Vol. 5. - pp. 2608-2610.

Veneziani N. [et al.] A Frequency-domain differential approach to the absolute phase etrieval in SAR interferometry. - Honolulu : Proceedings of the IEEE International Geoscience and Remote Sensing Symposium (IGARSS), 2000. - Vol. 2. - pp. 797 - 799.

Veneziani N. and Giacovazzo V.M. A Multi-chromatic Approach to SAR Interferometry. - Denver, Colorado, USA : IEEE International Conference on Geoscience and Remote Sensing Symposium (IGARSS), 2006. - pp. 3723 - 3726.

Veneziani N., Bovenga F. and Refice A. A Wide-Band approach to Absolute Phase Retrieval in SAR interferometry. Multidimensional Systems and Signal Processing, 2003. - Vol. 14. - pp. 183-205.

Wornell G. W. Wavelet-based representations for the 1/f family of fractal processes. Proceedings of the IEEE, 1993. - Vol. 81. - pp. 1428-1450.

Zhang Z. [et al.] A robust technique for matching two uncalibrated images through the recovery of the unknown epipolar geometry. Artificial intelligence, 1995. - Vol. 78. - pp. 87–119.

CHAPTER 4

Caltagirone F. [et al.] COSMO-SkyMed Full Constellation Orbital Flexibility and Interferometric Capabilities. - Cape Town : Proceedings of the 62nd International Astronautical Congress (IAC), 2011. - p. 10 pp. - ISSN 1995-6258.

Costantini M. [et al.] A New Method for Baseline Calibration in SAR Interferometry. - Frascati : Proceedings of the Fringe 2003 Workshop, 2003.

Crosetto M. and Aragues F.P. Radargrammetry and SAR Interferometry for DEM Deneration: Validation and Data Fusion. - Toulouse : Proceedings of CEOS SAR Workshop, 1999.

D.O. Nitti R.F. Hanssen, A. Refice, F. Bovenga, G. Milillo, R. Nutricato Evaluation on DEM-assisted SAR coregistration. - Cardiff : Proceedings of SPIE Remote Sensing, 2008.

E. Rodriguez J.M. Martin Theory and Design of Interferometric Synthetic Aperture Radars. Proc. Inst Elect. Eng., 1992. - Vol. 139. - pp. 147-159.

Eineder M., Hubig M. and Milcke B. Unwrapping large interferograms using the minimum cost flow algorithm. IEEE Geoscience and Remote Sensing, 1998. - pp. 83 - 87.

Ferretti A., Prati C. and Rocca F. Permanent Scatterers in SAR Interferometry. IEEE Transactions on Geoscience and Remote Sensing, 2001. - Vol. 39.

Gatelli F., Guarnieri A.M. and al. et The Wavenumber Shift in SAR Interferometry. IEEE Transaction on Geoscience and Remote Sensing, 1994. - Vol. 32.

I. Baran M.P. Stewart, B.M. Kampes, Z. Perski, P. Lilly A Modification to the Goldstein Radar Interferogram Filter. IEEE Transactions on Geoscience and Remote Sensing, 2003. - Vol. 41. - pp. 2114-2118.

Jehle M. [et al.] Improved Knowledge of SAR Geometry through Atmospheric Modelling. Proceedings of the 5th European Conference on Synthetic Aperture Radar (EUSAR), 2004.

Koppe W. [et al.] Validation of Pixel Location Accuracy of Orthorectified TerraSAR-X Products. Proceedings of the 8th European Conference on Synthetic Aperture Radar (EUSAR), 2010.

Lee J.-S. and al. et Intensity and Phase Statistics of Multilook Polarimetric and Inteferometric SAR Imagery. IEEE Proceedings, 1994. - Vol. 32.

M. Albani G. Schiavon, D. Solimini Analisi degli Effetti dell'Atmosfera sull'Interferometria SAR. - Cetraro (Cosenza) : Società Italiana di Elettromagnetismo, 1998. - p. 575-578.

M. Lachaise R. Bamler Minimum Cost Flow phase unwrapping supported by multibaseline unwrapped gradient. Proceedings of the 8th European Conference on Synthetic Aperture Radar (EUSAR), 2010.

N. Yague-Martinez C. Rossi, M. Lachaise, F. Rodriguez-Gonzalez, T. Fritz, H. Breit Interferometric Processing Algorithms of TanDEM-X Data. - [s.l.] : IEEE International Geoscience and Remote Sensing Symposium (IGARSS), 2010. - pp. 3518-3521.

National Geospatial-Intelligence Agency "Implementation Profile for High Resolution Elevation (HRE) products" [Rapporto]. - 2009. - NGA.IP.0002_1.0.

P. Rosen S. Hensley, I. Joughin, F. Li, S. Madsen, E. Rodriguez, R. Goldstein Synthetic Apertura Radar Interferometry. Proceeding of the IEEE, 2000. - Vol. 88. - pp. 373-379.

Porfilio M. [et al.] COSMO-SkyMed di Seconda Generazione Spotlight Focusing Chain Improvements and Interferometric and Change Detection Capabilities Enhancement through Common Band Filtering. - Napoli : 63 International Astronautical Congress (IAC 2012), 2012.

Potere D. Horizontal Positional Accuracy of Google Earth's High-Resolution Imagery Archive. Sensors, 2008. - Vol. 8. - pp. 7973-7981. - DOI: 10.3390/s8127973.

Sowter A. and Bennett J. InSAR Radargrammetry: A Solution to the Phase Integer Ambiguity Problem for Single Interferograms. Proceedings of the FRINGE 2003 Workshop, 2003.

W.Koppe N.Kiefl, S.D. Hennig, J.Janoth Validation of Pixel Location Accuracy of Orthorectified TerraSAR-X Products. EUSAR 2010, 2010.

Zebker H., Werner C. and al. et Accuracy of Topographic Maps Derived from ERS-1 Interferometric Radar. IEEE Transactions on Geoscience and Remote Sensing, 1994. - Vol. 32.

Zhang K. [et al.] A New Approach to Improve the Accuracy of Baseline Estimation for Spaceborne Radar Interferometry. Proceedings of the IEEE International Geoscience and Remote Sensing Symposium (IGARSS), 2009. - Vol. 5. - p. V-162 - V-165.

Zhu X. and Bamler R. Very High Resolution Spaceborne SAR Tomography in Urban Environment. IEEE Transactions on Geoscience and Remote Sensing, 2010. - Vol. 48.

CHAPTER 5

Almeida L.B. The fractional Fourier transform and time-frequency representations. IEEE Transactions on Signal Processing, 1994. - Vol. 42. - pp. 3084-3091.

Antipov I. Simulation of Sea Clutter Returns. Tactical Surveillance System Division, Electronic and Surveillance Research Laboratory, 1998.

C. Schaefer A. Wagner Analysis of Potential GMTI Performance of TanDEM-X. - Friedrichshafen, Germany : 7th European Conference on Synthetic Aperture Radar (EUSAR 2008), 2008.

C.E. Livingstone I. Sikaneta, C.H. Gierull, S. Chiu, A. Beaudoin, J. Campbell, J. Beaudoin, S. Gong, T.A. Knight An airborne synthetic aperture radar experiment to support RADARSAT-2 ground moving target indication. Can. J. Remote Sensing, 2002. - Vol. 28. - pp. 794-813.

Chiu S. A constant false alarm rate (CFAR) detector for RADARSAT-2 along-track interferometry. Canadian Journal of Remote Sensing, 2005. - pp. 73-84. - 10.5589/m04-057.

Chiu S. A Simulation Study of Multi-Channel RADARSAT-2 GMTI // Technical Memorandum DRDC TM 2006-209. - Ottawa : Defence R&D Canada, 2006.

Chiu S. Application of Fractional Fourier Transform to Moving Target Indication via Along-Track Interferometry. EURASIP Journal on Advances in Signal Processing, 2005. - Vol. 20.

Chiu Shen [et al.] Radarsat-2 Moving Object Detection Experiment (MODEX). IEEE International Geoscience and Remote Sensing Symposium (IGARSS 2008), 2008. - Vol. 1. - p. I13 - I16.

Dong Zhen, Cai, Bin, Liang, Diannong Detection of Ground Moving Targets for Two-Channel Spaceborne SAR-ATI. EURASIP Journal on Advances in Signal Processing, 2010.

Ender J. H. G. Detection and estimation of moving target signals by multi-channel SAR. AEÜ Int. J. Electron. Commun., 1996. - Vols. 50, no. 2, pp. 150–156.

F. Nathanson J. Reilly, M. Cohen Radar Design Principles - Signal Processing and the Environment. SciTech Pub., 1999. - p. 278.

Gierull C.H. Ground moving target parameter estimation for two-channel SAR. IEE Proceedings Radar, Sonar and Navigation, 2006. - Vol. 153. - pp. 224- 233.

Golikov V. [et al.] CFAR robust detection of moving target in presence of fluctuating background. 12th International Conference on Mathematical Methods in Electromagnetic Theory, 2008. - pp. 144-146.

J. Mittermayer H. Runge Conceptual studies for exploiting the TerraSAR-X dual receive antenna. IEEE International Geoscience and Remote Sensing Symposium (IGARSS 2003), 2003. - Vol. 3. - pp. 2140- 2142.

J. Sijbers A. J. den Dekker, E. Raman, D. Van Dyck Parameter estimation from magnitude MR images. International Journal of Imaging Systems and Technology, 1999. - Vol. 10. - pp. 109-114.

L. Yang T. Wang, Z. Bao Ground Moving Target Indication Using an InSAR System With a Hybrid Baseline. IEEE Geoscience and Remote Sensing Letters, 2008. - Vol. 5. - pp. 373-377.

R.G. White D.J. Coe Detection limits for sideways looking MTI radars. Radar 97 (Conf. Publ. No. 449), 1997. - pp. 434-438. - ISBN 0-85296-698-9.

Rizzato D. Techniques for ground moving target detection and velocity estimation with multi-channel Synthetic Aperture Radars (SAR). - University of Padova : Master Thesis, 2012.

S. Baumgartner G. Krieger, K. Bethke A Large Along-Track Baseline Approach for Ground Moving Target Indication Using TanDEM-X. - Cologne, Germany : International Radar Symposium, 2007.

S. Baumgartner M. Gabele, G. Krieger, K.H. Bethke, S. Zuev Traffic Monitoring with SAR: Implications of Target Acceleration. - Dresden, Germany : Proceedings of EUSAR 2006, 2006.

S. Suchandt H. Runge Along-Track Interferometry Using TanDEM-X: First Results from Marine and Land Applications. - Nuremberg : 9th European Conference on Synthetic Aperture Radar (EUSAR 2012), 2012. - p. 392-395.

S. Suchandt H. Runge, U. Steinbrecher Ship detection and measurement using the TerraSAR-X dual-receive antenna mode. IEEE International Geoscience and Remote Sensing Symposium (IGARSS), 2010. - pp. 2860 - 2863.

S.J. Frasier A.J. Camps Dual-beam Interferometry for Ocean Surface Current Vector Mapping. IEEE Trans on Geoscience and Remote Sensing, 2001. - pp. 401-414.

Sharma J. The influence of target acceleration on dual-channel SAR-GMTI data. Master thesis, Department of Geomatics Engineering, 2004.

Skolnik Merrill I. Radar Handbook. McGraw-Hill Publishing Co., 2nd revised edition, 1989. - ISBN 007057913X.

V.C. Chen H. Ling Time-Frequency Transforms for Radar Imaging and Signal Analysis. Artech House, 2002.

ACKNOWLEDGEMENTS

La scelta di voler affrontare un percorso di Dottorato della durata di tre anni, parallelamente ad un'attività lavorativa impegnativa e ricca di stimoli, porta senz'altro con sé una serie di sacrifici e di difficoltà che non sarei stato in grado di affrontare se non grazie al supporto di molte persone, che meritano pertanto uno speciale ringraziamento.

In primo luogo, desidero ringraziare il Prof. Antonio Moccia, mio tutor di Dottorato, che mi segue dalla Tesi di Laurea triennale e mi ha accompagnato lungo l'intero percorso formativo, per la fiducia che mi ha accordato, la flessibilità che mi ha concesso e l'insegnamento umano e professionale che mi ha trasmesso. Un sentito ringraziamento va anche a tutti gli altri Professori dell'Università degli Studi di Napoli "Federico II", ed in particolare al Prof. Giovanni Maria Carlomagno, con i quali si è instaurato negli anni uno splendido rapporto.

In secondo luogo, voglio ringraziare il Col. Giuseppe D'Amico, Direttore del Centro Interforze Telerilevamento Satellitare, il Ten. Col. Franco Nardone ed il Magg. Riccardo Cetta, per la sensibilità mostrata verso questa attività che ho voluto intraprendere e per avermi messo nelle condizioni di ottemperare ai relativi impegni con la massima disponibilità e flessibilità possibile.

Infine, il mio più forte ringraziamento va a chi mi è più vicino, ed in particolare alla mia famiglia, per aver condiviso con me tutte le emozioni che hanno accompagnato questo percorso, per avermi supportato ed incoraggiato nei momenti più difficili, per aver gioito dei traguardi e delle soddisfazioni raggiunte, per rappresentare un punto di riferimento sicuro ed incondizionato; ed a Danila, che ha saputo starmi vicino anche quando ha dovuto condividere i sacrifici che ho affrontato, anche quando al termine di una intensa giornata lavorativa o nei fine settimana ho dovuto dedicarmi al Dottorato, per aver condiviso ogni momento di questo percorso riuscendo a trasmettermi quotidianamente quella serenità e quell'entusiasmo necessari ad affrontare anche le situazioni più impegnative. È a voi che dedico questo Dottorato, che è il massimo traguardo a coronamento di un intenso percorso di studi.

23 Febbraio 2013

Andrea

I risultati presentati in questo lavoro di tesi sono stati ottenuti facendo uso di dati disponibili presso il Centro Interforze Telerilevamento Satellitare dello Stato Maggiore della Difesa non soggetti a limitazioni nella loro divulgazione.

The results presented in this thesis are obtained using data available at the Centro Interforze Telerilevamento Satellitare of the Defence General Staff which are not subject to disclosure limitations.